Advanced Fluid Mechanics

Transition to Turbulence & Turbulence

Applications to Transfers, Aerodynamics & Wind Energy

by *Emmanuel Plaut* & *Joachim Peinke* at Mines Nancy

Version of February 12, 2017

Contents

Introduction **5**

1 Rayleigh-Bénard Thermoconvection **7**

1.1 Generalities . . . 7
1.2 Linear stability analysis of slip RBT . . . 9
1.2.1 Linear stability analysis: general modal approach . . . 9
1.2.2 Linear stability analysis of slip RBT . . . 10
Ex. 1.0 : Linear stability analysis of slip RBT - Most relevant modes . . . 10
Ex. 1.1 : General linear stability analysis of slip RBT . . . 11
1.3 The linear modes basis - The adjoint problem & adjoint modes . . . 12
1.3.1 Adjoint problem & adjoint modes: general principles . . . 13
Physical meaning of an adjoint mode: 'receptivity function' . . . 13
1.3.2 Adjoint problem & adjoint modes in slip RBT . . . 14
Ex. 1.2 : Adjoint problem in slip RBT . . . 14
Technical skill: Recursive integration by parts . . . 14
Ex. 1.3 : Adjoint critical mode in RBT with slip boundaries . . . 14
1.4 Weakly Nonlinear Analysis of slip RBT . . . 15
Ex. 1.4 : Quasistatic elimination of the passive mode in slip RBT . . . 16
Ex. 1.5 : Passive mode in slip RBT first control the Nusselt number . . . 16
Ex. 1.6 : Resonant terms in slip RBT at order A^3 . . . 16
Ex. 1.7 : Saturation in slip RBT . . . 16
1.5 A glimpse at the Lorenz model and Chaos . . . 17
1.6 Numerical Linear Analysis of no-slip RBT . . . 19
Ex. 1.8 : Numerical linear stability analysis of no-slip RBT with a spectral method . . . 19
1.7 Short review of no-slip RBT . . . 20
1.8 Problem . . . 22
Pb. 1.1 : Lorenz model of slip Rayleigh-Bénard Thermoconvection . . . 22

2 Transition to Turbulence in Open Shear Flows **25**
2.1 Generalities . . . 25
2.2 Linear stability analysis of Plane Parallel Flows . . . 27
2.2.1 Linear stability analysis of Inviscid Plane Parallel Flows . . . 27
Ex. 2.1 : Rayleigh's inflection point criterion . . . 27
2.2.2 Linear stability analysis of Viscous Plane Poiseuille Flow . . . 28
Ex. 2.2 : Linear stability analysis of Plane Poiseuille Flow with a spectral method . . . 28
Ex. 2.3 : Linear stability analysis of PPF at high Reynolds number . . . 31
2.3 Weakly nonlinear stability analysis of Plane Poiseuille Flow . . . 32
2.3.1 Linear modes basis - Adjoint problem & adjoint modes . . . 32
Ex. 2.4 : Adjoint problem and adjoint critical mode in PPF . . . 32
2.3.2 Simplified form of the weakly nonlinear solution: active and passive modes . . . 33
Ex. 2.5 : General form of the nonlinear source terms for the homogeneous mode . . . 35
Ex. 2.6 : Homogeneous passive mode in PPF with a fixed mean pressure gradient . . . 35
2.3.3 Feedback at order A^3 . . . 36
Ex. 2.7 : Feedback coefficient in PPF with a fixed mean pressure gradient . . . 36
2.4 About spatial and spatio-temporal stability theories . . . 39
2.5 Short review of transition in OSF . . . 39
2.6 Problem . . . 42
Pb. 2.1 : Spatial linear stability analysis - The case of Plane Poiseuille Flow . . . 42

3 Wind Energy and Turbulence **47**
3.1 Wind Energy: Power performance theory . . . 47
3.1.1 Momentum theory for wind turbines . . . 47
3.1.2 Power performance - Betz limit . . . 49
3.1.3 Limitations of Betz theory - Energy losses . . . 50
3.1.4 Power curve . . . 51
3.2 Rotor blade: Blade Element Momentum theory (BEM) . . . 53
3.3 IEC power curve and Annual Energy Production . . . 56
3.3.1 Turbulence-induced deviations . . . 57
3.3.2 Annual Energy Production . . . 59
3.4 A new alternative: the Langevin power curve . . . 60
3.4.1 A dynamical concept . . . 60
3.4.2 The Langevin equation . . . 60
3.4.3 The drift function and the Langevin power curve . . . 61
3.4.4 Advantages of the Langevin approach . . . 63
3.4.5 Detecting dynamical anomalies . . . 64
3.5 Turbulence modelling . . . 65
3.5.1 General definitions - Experimental results . . . 65
3.5.2 Kolmogorov & Obukov 1941 . . . 66
3.5.3 Kolmogorov & Obukov 1962 . . . 67

3.5.4 Multiplicative cascade after Castaing . . . 70
3.6 Data analysis - Wind data . . . 71
3.6.1 One-Point Statistics . . . 72
3.6.2 Two-point statistics . . . 77
3.6.3 Synthetic Time Series vs Atmospheric Turbulence . . . 79
3.6.4 Outlook: n-point statistics . . . 80
3.6.5 Conclusions . . . 81
3.7 Exercises . . . 83
Ex. 3.1 : Study of time series of Wind Speed and Wind Turbine Power . . . 83
Ex. 3.2 : Study of time series of Turbulent Flows . . . 84
Ex. 3.3 : Study of a time series of a Grid Turbulence Flow . . . 85

A Introduction to stochastic theory **87**
A.1 Markov property . . . 88
A.2 Kramers-Moyal expansion . . . 89
A.3 Fokker-Planck equation . . . 90
A.4 Langevin equation . . . 91

B Elements of solution of the problems **93**
Pb. : Lorenz model of slip Rayleigh-Bénard Thermoconvection . . . 93
Pb. : Spatial linear stability analysis - The case of Plane Poiseuille Flow . . . 95

Bibliography **97**

Introduction

This is the latest version of the Lecture Notes of Emmanuel Plaut and Joachim Peinke, for the module ***Advanced Fluid Mechanics - Transition to Turbulence & Turbulence - Applications to Transfers, Aerodynamics & Wind Energy*** at **Mines Nancy**, in the Department Energy & Fluid Mechanics, at the Master 2 Level.

This module is somehow a follow up of the modules ***Mécanique des fluides*** (Plaut 2016) and ***Machines à fluides - Turbomachines*** (Jenny 2016) of the Master 1 Level. Indeed one can find, in the Chapter 3 (resp. 6) of Plaut (2016), an introduction to Instabilities (resp. Turbulent flows); in the Chapter 4 of Jenny (2016), an introduction to Wind Energy.

In the first Part, driven by E. P., we study the problem of the ***transition to turbulence*** in fluid systems, either closed in Chapter 1, or open in Chapter 2. Chapter 1, which focusses on ***Rayleigh-Bénard Thermoconvection***, is an occasion to increase our knowledge about *Heat Transfers in convection*. Chapter 2, which focusses on ***Open Shear Flows***, is an occasion to increase our knowledge in *Aerodynamics*. We introduce, on these examples, the ***bifurcation theory*** (or ***'catastrophe theory'***), which is of interest for all nonlinear dynamical systems in general... 'Standard' dynamical systems governed by ordinary differential equations, or 'extended' dynamical systems governed by partial differential equations. Of course, 'fluid systems' are 'extended dynamical systems'...
In the second Part, driven by J. P., which corresponds to the Chapter 3 (and Appendix A), we give some notions on ***turbulence modelling***, concentrating on the fluctuations (not precisely characterized in Plaut 2016), and on applications to ***Wind Energy***. We use ***statistical*** and ***stochastic analysis*** and ***modelling***, which have been to some extent introduced in some modules of Mathematics at Mines Nancy.

The aim of this document is to give a framework for the lectures, with a level of details that is moderate in Chapters 1, 2, and, on the contrary, rather high in Chapter 3. Some notes in Chapter 3 and Appendix A are only devoted to the most interested readers... Some Exercises of Chapters 1 and 2 are solved during the lectures, and their solutions displayed in the 'Video presentations' posted on the dynamic web page of the module[1]

http://emmanuelplaut.perso.univ-lorraine.fr/afm .

This web page also contains turbulent flow data sets, that have been given by J. P., for Ex. 3.2...

[1] Please check this page for new versions of these Lecture Notes, and for the planning of this module. Note also that Appendix B gives some elements of solution of the problems of Chapters 1 and 2. To save paper, ink and energy, the printed version of this document does not include the Appendices; they can be read only in the PDF version of the Lecture Notes available on the web.

For the students of Mines Nancy, this module has an Intranet - ARCHE page

http://arche.univ-lorraine.fr/course/view.php?id=11599

on which wind speed and wind turbine power data, grid turbulence data are available for Ex. 3.1 and 3.3.

E. P. thanks Luca Brandt from KTH for providing a copy of Schlatter *et al.* (2010). J. P. acknowledges support by the *Fondation Mines Nancy*.

Nancy & Oldenburg, February 12, 2017.

Emmanuel Plaut & Joachim Peinke.

Chapter 1

Rayleigh-Bénard Thermoconvection

This chapter corresponds to the Sessions 1 and 2 of 2016-2017. Note that most of the material presented here is also presented with more details in Plaut (2008).

1.1 Generalities

Rayleigh-Bénard Thermoconvection (RBT; Fig. 1.1) is a 'simple' closed fluid system, that permits well-controlled experiments, and may display complex Heat Transfer properties. In this system, contrarily to the case of a differentially heated cavity studied by Davis (1983), thermoconvection can only come in through an ***instability*** of the conduction state.

We assume the ***Boussinesq approximation***, that states that the density ρ of the fluid depends on its temperature T according to

$$\rho \;=\; \rho_0\,[1-\alpha(T-T_0)] \tag{1.1}$$

with ρ_0 the reference density, T_0 the reference temperature, α the thermal expansion coefficient. Consequently the Boussinesq equations for the velocity field $\overline{\mathbf{v}}$, the pressure field p and the temperature field T read

$$\mathrm{div}\overline{\mathbf{v}} \;=\; 0\;, \tag{1.2}$$

$$\frac{d\overline{\mathbf{v}}}{dt} \;=\; -\,\alpha T\,\overline{\mathbf{g}} \;-\; \overline{\boldsymbol{\nabla}}p' \;+\; \nu\overline{\boldsymbol{\Delta}}\overline{\mathbf{v}}\;, \tag{1.3}$$

$$\frac{dT}{dt} \;=\; \kappa\Delta T\;. \tag{1.4}$$

Here $\overline{\mathbf{g}}$ is the acceleration due to gravity, ν the kinematic viscosity of the fluid, κ its heat diffusivity. The pressure is a modified one, hence the notation p'.
These equations always admit a static solution that satisfies the isothermal boundary conditions:

$$\overline{\mathbf{v}} \;=\; \overline{\mathbf{0}}\;,\quad T \;=\; T_0 \;-\; \delta T\frac{z}{d}\quad\text{with}\quad \delta T \;=\; T_2-T_1\;.$$

This proves that convection can only set in through an ***instability*** of this static solution.
We introduce dimensionless equations with the thickness d as the unit of length,

$$\text{the heat diffusion time}\;\; \tau_{\mathrm{therm}} \;=\; d^2/\kappa \;\;\text{as the unit of time,}$$

$$V \;=\; d/\tau_{\mathrm{therm}} \;=\; \kappa/d \;\;\text{as the unit of velocity,}$$

$$\delta T \;\;\text{as the unit of temperature.}$$

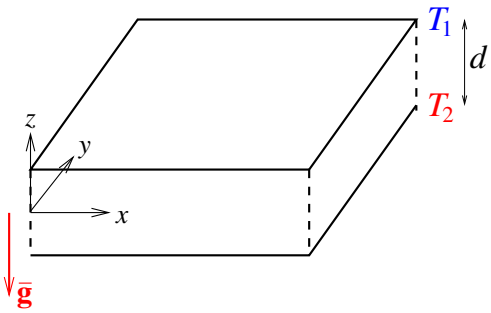

Fig. 1.1 : The ***Rayleigh-Bénard Thermoconvection*** system. A layer of fluid is sandwiched between two horizontal, isothermal plates, with $T_2 > T_1$.

We also introduce a dimensionless perturbation of temperature θ, such that the dimensionless temperature

$$T' \;=\; T'_0 \;-\; z' \;+\; \theta$$

Dropping the primes for the dimensionless quantities, we get the ***dimensionless Boussinesq equations***

$$\mathrm{div}\overline{\mathbf{v}} \;=\; 0 \;, \tag{1.5}$$

$$P^{-1}\frac{d\overline{\mathbf{v}}}{dt} \;=\; R\theta\;\overline{\mathbf{e}}_z \;-\; \overline{\boldsymbol{\nabla}}p \;+\; \overline{\boldsymbol{\Delta}}\overline{\mathbf{v}} \;, \tag{1.6}$$

$$\frac{d\theta}{dt} \;=\; \Delta\theta \;+\; v_z \;, \tag{1.7}$$

with

$$\text{the ***Rayleigh number***}\;\; R \;=\; \alpha\delta T g d^3/(\kappa\nu) \quad\text{and}\quad \text{the ***Prandtl number***}\;\; P \;=\; \nu/\kappa \;. \tag{1.8}$$

Because of the ***isotropy of the problem in the horizontal plane*** we may focus on 2D xz solutions

$$\overline{\mathbf{v}} \;=\; v_x(x,z,t)\;\overline{\mathbf{e}}_x \;+\; v_z(x,z,t)\;\overline{\mathbf{e}}_z \;,\quad \theta \;=\; \theta(x,z,t) \;. \tag{1.9}$$

Thus the mass-conservation equation (1.5) can be solved conveniently by using a ***streamfunction*** ψ such that

$$\overline{\mathbf{v}} \;=\; \overline{\mathbf{curl}}(\psi\;\overline{\mathbf{e}}_y) \;=\; (\overline{\boldsymbol{\nabla}}\psi)\times\overline{\mathbf{e}}_y \;=\; -\,(\partial_z\psi)\;\overline{\mathbf{e}}_x \;+\; (\partial_x\psi)\;\overline{\mathbf{e}}_z \;. \tag{1.10}$$

Moreover, the pressure can be eliminated by solving, instead of the Navier-Stokes equation (1.6), the vorticity equation, which reduces to its component in the y direction,

$$P^{-1}\partial_t(-\Delta\psi) \;+\; P^{-1}\big[\partial_z\big(\overline{\mathbf{v}}\cdot\overline{\boldsymbol{\nabla}}v_x\big) - \partial_x\big(\overline{\mathbf{v}}\cdot\overline{\boldsymbol{\nabla}}v_z\big)\big] \;=\; -\,R\partial_x\theta \;+\; \Delta(-\Delta\psi) \;. \tag{1.11}$$

To put the equations (1.11) and (1.7) under a 'matrix form', we introduce the ***local state vector***

$$V \;=\; \begin{bmatrix}\psi\\ \theta\end{bmatrix} \quad\text{also denoted}\quad (\psi,\,\theta) \;. \tag{1.12}$$

It fulfills

$$\boxed{D\cdot\partial_t V \;=\; L_R\cdot V \;+\; N_2(V,V)} \tag{1.13}$$

with

$$[D\cdot\partial_t V]_1 \;=\; P^{-1}(-\Delta\partial_t\psi) \;,\quad [L_R\cdot V]_1 \;=\; -\,R\partial_x\theta \;+\; \Delta(-\Delta\psi) \;, \tag{1.14a}$$

$$[N_2(V,V)]_1 \;=\; P^{-1}\big[\partial_x\big(\overline{\mathbf{v}}\cdot\overline{\boldsymbol{\nabla}}v_z\big) - \partial_z\big(\overline{\mathbf{v}}\cdot\overline{\boldsymbol{\nabla}}v_x\big)\big] \;, \tag{1.14b}$$

$$[D\cdot\partial_t V]_2 \;=\; \partial_t\theta \;,\quad [L_R\cdot V]_2 \;=\; \Delta\theta \;+\; v_z \;,\quad [N_2(V,V)]_2 \;=\; -\,\overline{\mathbf{v}}\cdot\overline{\boldsymbol{\nabla}}\theta \;. \tag{1.14c}$$

The boundary conditions on θ describe ***isothermal boundaries***:

$$\theta = 0 \quad \text{if} \quad z = \pm 1/2 \ . \tag{1.15}$$

The most physical boundary conditions on ψ describe ***no-slip boundaries***:

$$v_x = v_z = 0 \quad \Longleftrightarrow \quad \partial_x \psi = \partial_z \psi = 0 \quad \text{if} \quad z = \pm 1/2 \ . \tag{1.16}$$

However, with such boundary conditions even the linear problem requires numerical computations (exercise 1.8), whereas more 'idealistic' conditions of slip boundaries without shear stress permit analytical calculations, and will therefore be chosen in a first approach. These ***'slip boundary conditions'***, also denoted ***'stress-free boundary conditions'*** by some authors, read

$$v_z = 0 \quad \text{and} \quad D_{xz} = 0 \quad \text{if} \quad z = \pm 1/2 \ , \tag{1.17}$$

with D_{xz} the xz component of the *rate-of-strain tensor*

$$\overline{\overline{\mathbf{D}}} \ = \ \frac{1}{2}\Big(\overline{\overline{\boldsymbol{\nabla}}}\mathbf{v} + \overline{\overline{\boldsymbol{\nabla}}}\mathbf{v}^T\Big) \ , \tag{1.18}$$

that controls the tangential stresses at the boundaries,

$$D_{xz} \ = \ \frac{1}{2}(\partial_z v_x + \partial_x v_z) \ . \tag{1.19}$$

Thus, the conditions (1.17) reduce to

$$v_z = 0 \quad \text{and} \quad \partial_z v_x = 0 \quad \Longleftrightarrow \quad \partial_x \psi = \partial_z^2 \psi = 0 \quad \text{if} \quad z = \pm 1/2 \ . \tag{1.20}$$

1.2 Linear stability analysis of slip RBT

Since the solution $V = (0,0)$ or '$V = 0$' of (1.13) always exists, the problem of the onset of convection can be attacked with a ***linear stability analysis***, here, a ***'temporal'*** stability analysis[1].

1.2.1 Linear stability analysis: general modal approach

Generally, in such an analysis the vector V is supposed to be small, hence a nonlinear problem of the form (1.13) is replaced by its linearized version, the linear problem

$$\boxed{D \cdot \partial_t V \ = \ L_R \cdot V} \ . \tag{1.21}$$

This problem is solved using a ***complex modal analysis***, i.e., by a superposition of ***linear eigenmodes*** or ***normal modes*** $V_1(\mathbf{q})$ that depends on numbers $\mathbf{q}$, on R and on the other parameters of the problem (this dependence is not recalled), and fulfill

$$\boxed{\sigma(\mathbf{q},R) \ D \cdot V_1(\mathbf{q}) \ = \ L_R \cdot V_1(\mathbf{q})} \ . \tag{1.22}$$

In this equation, $\sigma(\mathbf{q},R) \in \mathbb{C}$ is the ***temporal eigenvalue***, since the solution of (1.21) with the initial condition

$$V(t=0) \ = \ A_0 \ V_1(\mathbf{q}) \tag{1.23}$$

[1] We will see in section 2.4 that in open flows a ***'spatial'*** stability analysis may be equally relevant.

is

$$V(t) \;=\; A_0 \;\; e^{\sigma(\mathbf{q},R)\;t}\; V_1(\mathbf{q})\;.$$

For systems that are locally invariant by translations $x \mapsto x+\ell$, one usually adopts simple conditions of periodicity under $x \mapsto x+L$ ('*periodic boundary conditions*') that may be relevant for real systems of finite but 'large' size in the x direction, with the belief that these transversal boundaries do not strongly influence the behaviour of the system 'far from the boundaries'. Therefore, in a 'Fourier' approach, the modes $V_1(\mathbf{q})$ are Fourier modes

$$V_1(\mathbf{q}) \;=\; \widetilde{V}_1(k,\mathbf{q}') \;\; e^{ikx} \tag{1.24}$$

with k the ***wavenumber*** in the x-direction[2] and $\mathbf{q}'$ the other numbers that label the modes. Then the solution of (1.21) with the initial condition (1.23) reads

$$V(t) \;=\; A_0 \;\; e^{ikx \;+\; \sigma(\mathbf{q},R)\;t}\; \widetilde{V}_1(k,\mathbf{q}') \;=\; A_0 \;\; e^{i(kx+\sigma_i t)} \;\; e^{\sigma_r t}\; \widetilde{V}_1(k,\mathbf{q}') \tag{1.25}$$

where we have used a decomposition of $\sigma(\mathbf{q},R)$ in real and imaginary parts,

$$\sigma(\mathbf{q},R) \;=\; \sigma_r(\mathbf{q},R) + i\sigma_i(\mathbf{q},R)\;. \tag{1.26}$$

Therefore, we distinguish three cases, depending on the sign of $\sigma_r(\mathbf{q},R)$:

- if $\sigma_r > 0$, the mode is ***amplified***, with the *growth rate* σ_r ;
- if $\sigma_r = 0$, the mode is ***neutral*** ;
- if $\sigma_r < 0$, the mode is ***damped***, with the *damping rate* $-\sigma_r$.

Assuming that $k > 0$, we also distinguish three cases, depending on the sign of $\sigma_i(\mathbf{q},R)$:

- if $\sigma_i > 0$, the mode is a ***left-traveling wave***, with an *angular frequency* $\omega = \sigma_i$ and a *phase velocity* $c = \omega/k$;
- if $\sigma_i = 0$, the mode is ***'stationary'*** ;
- if $\sigma_i < 0$, the mode is a ***right-traveling wave***, with an *angular frequency* $\omega = -\sigma_i$ and a *phase velocity* $c = \omega/k$.

The trivial solution $V = 0$ of (1.21) is ***stable*** if no amplified mode exist - ***unstable*** as soon as one amplified mode exists.

1.2.2 Linear stability analysis of slip RBT

We now perform the linear stability analysis of slip RBT, in two steps - two exercises.

Exercise 1.0 ***Linear stability analysis of slip RBT - Most relevant modes***

Check that modes of the form

$$V_1(k,\pm) \;=\; (\Psi,\,\Theta)\;\exp(ikx)\;\cos(\pi z) \tag{1.27}$$

with $k > 0$, Ψ and Θ two complex numbers, are eigenmodes of the problem (1.21) for slip RBT, provided that the ratio Ψ/Θ assumes a precise value, and that $\sigma = \sigma(k,\pm)$ fulfills a characteristic

[2] An integer multiple of $2\pi/L$. If L is large, the discrete set of the possible values of k is almost $\mathbb{R}$.

equation of degree 2. Check that this equation has two real roots, which leads to a mode $V_1(k,-)$ that is always damped, and a mode $V_1(k,+)$ that becomes amplified if the Rayleigh number exceeds a ***neutral value*** (Fig. 1.3)

$$R_0(k) \;=\; \frac{(k^2+\pi^2)^3}{k^2}\;. \tag{1.28}$$

Identify the ***critical Rayleigh number***

$$R_c \;=\; 27\pi^4/4 \;=\; 657.5 \tag{1.29}$$

above which the conduction solution looses its stability. The first amplified mode, the so-called ***critical mode***, has an x-wavenumber which is the ***critical wavenumber***

$$k_c \;=\; \pi/\sqrt{2} \;=\; 2.22\;. \tag{1.30}$$

Thus ***'roll patterns'***, with periodic modulations of the average temperature, appear spontaneously just above onset, with the ***critical wavelength***

$$\lambda_c \;=\; 2\pi/k_c \;=\; 2\sqrt{2} \;=\; 2.83\;. \tag{1.31}$$

This corresponds to a ***patterning bifurcation***. The precise form of the complex ***critical mode***

$$V_{1c} \;=\; (-3i\pi/\sqrt{2},\,1)\;\exp(ik_cx)\;\cos(\pi z) \tag{1.32}$$

leads to a real critical mode

$$V_{1r} \;=\; AV_{1c}+c.c. \;=\; A(3\sqrt{2}\pi\;\sin(k_cx),\,2\cos(k_cx))\;\cos(\pi z)\;. \tag{1.33}$$

Plot the corresponding streamlines and isotherms in the layer, and explain the ***instability loop*** that amplifies this mode...

All this is confirmed by experiments, such as the ones of Hu *et al.* (1993), which display nice roll patterns. See Fig. 1.5 ; note, however, that the boundary conditions in the experiments are 'no-slip' instead of 'stress-free'.

Exercise 1.1 ***General linear stability analysis of slip RBT***

To perform a general linear stability analysis of the problem (1.13) with the boundary conditions (1.15) and (1.20), it is more convenient to use another frame $Oxyz'$ where the layer is located between $z'=0$ (bottom plate) and $z'=1$ (top plate), i.e., to use $z'=z+1/2$. In this exercise, we note z instead of z', i.e. $z\in\;]0,1[$.

1 Calculate ***systematically*** all x-homogeneous normal modes, that do not depend on x, and have been disregarded in Ex. 1.0. Show that they are indeed 'irrelevant'.

Indications:

Observe that the heat and vorticity equations are decoupled.
First, solve the heat equation. Search solutions of the form $\theta = a_+\;e^{rz}+a_-\;e^{-rz}$. Establish a link between r and the temporal eigenvalue σ. With the boundary conditions, obtain an homogeneous system on (a_+,a_-). Explain why the determinant of this system must vanish. From this condition, obtain the values of σ and finally the form of θ.
Second, observe that ψ'' obeys an equation similar to the heat equation...

2 Focus now on x-dependent solutions. In Ex. 1.0, we have calculated only one family of Fourier normal modes,

$$V_1(k,\pm) \;=\; (\Psi(k,\pm),\, \Theta(k,\pm))\;\exp(ikx)\;\sin(\pi z)\;, \tag{1.34}$$

with $k \neq 0$ the x-wavenumber. Thus, the fact that an initial condition

$$V(t=0) \;=\; (\psi(t=0),\, \theta(t=0))$$

can be decomposed on the basis of all normal modes

$$V(t=0) \;=\; \sum_{\mathbf{q}} A(\mathbf{q}) V_1(\mathbf{q})$$

is unclear, as is also the precise meaning of $\mathbf{q}$, the labels that index all normal modes.
For the sake of simplicity, we consider periodic boundary conditions in the x direction, under $x \mapsto x + L$. Hence exponential Fourier series can be used to analyse the x dependence, i.e. $\mathbf{q}$ contains generally the x-wavenumber k such that

$$V_1(\mathbf{q}) \;=\; V_1(k,\mathbf{q}') \;=\; V_1(z;k,\mathbf{q}')\;\exp(ikx)$$

with $k \in \mathbb{K}$, $\mathbb{K} = (2\pi/L)\mathbb{Z}$, $\mathbf{q}'$ other labels that have to be identified.

Show that modes

$$V_1(k,\pm,n) \;=\; (\Psi(k,\pm,n),\, \Theta(k,\pm,n))\;\exp(ikx)\;\sin(n\pi z)$$

with $n \in \mathbb{N}^*$ are also normal modes, and establish a characteristic equation for the temporal eigenvalue σ. Check that for given k and n, there are indeed two modes $+$ and $-$ and two eigenvalues $\sigma(k,\pm,n)$. Check that with $n = 1$ you recover the modes (1.34) and their corresponding eigenvalues. Check that the most relevant modes are indeed the modes with $n = 1$.

Comments:

From a mathematical point of view, the fact that any initial condition can be written as

$$V(t=0) \;=\; \sum_{k\in\mathbb{K}} \sum_{s=\pm} \sum_{n\in\mathbb{N}^*} A(k,s,n)\; V_1(k,s,n)$$

results from a development in exponential Fourier series of x, trigonometric Fourier series of z, and from the fact that, for given k and n, $(\Psi(k,+,n),\, \Theta(k,+,n))$ and $(\Psi(k,-,n),\, \Theta(k,-,n))$ form a basis of $\mathbb{C}^2$.
Coming back to $z \in\;]-1/2,1/2[$, the following symmetry property can be shown: all normal modes are *either* even *or* odd under the midplane reflection symmetry $z \mapsto -z$.

1.3 The linear modes basis - The adjoint problem & adjoint modes

Hereafter we work in a box with periodic boundary conditions under $x \mapsto x + \lambda_c$. Consequently the wavenumber $k \in \mathbb{K}$ with $\mathbb{K} = k_c\mathbb{Z}$. Hence we can label the normal modes with $\mathbf{q} = (k,s,n) \in \mathbb{K} \times \{+,-\} \times \mathbb{N}^*$, and a general field can always be written as a superposition of normal modes,

$$V \;=\; \sum_{k\in\mathbb{K}} \sum_{s=\pm} \sum_{n\in\mathbb{N}^*} A(k,s,n)\; V_1(k,s,n) = \;\sum_{\mathbf{q}} A(\mathbf{q})\; V_1(\mathbf{q})\;. \tag{1.35}$$

It is important to be able to calculate systematically the 'amplitudes' $A(\mathbf{q})$. For this purpose, we introduce (generally, the technique is not only specific to RBT) the ***adjoint problem*** and ***adjoint modes*** as follows.

1.3.1 Adjoint problem & adjoint modes: general principles

- We first introduce the ***Hermitian inner product***

$$\langle V,\, U\rangle \;=\; \int_{x=0}^{\lambda_c}\int_{z=-1/2}^{1/2} V(x,z)\cdot U^*(x,z)\;\frac{dx}{\lambda_c}\;dz\;. \tag{1.36}$$

- We then define the ***adjoint operators*** $D^\dagger$ and $L^\dagger$ such that

$$\forall V,U,\quad \langle D\cdot V,\,U\rangle \;=\; \Big\langle V,\,D^\dagger\cdot U\Big\rangle \quad\text{and}\quad \langle L\cdot V,\,U\rangle \;=\; \Big\langle V,\,L^\dagger\cdot U\Big\rangle\;, \tag{1.37}$$

  V and U satisfying the boundary conditions of the problem.

- We assume[3] that the ***adjoint eigenproblem***

$$\sigma^* D^\dagger\cdot U \;=\; L^\dagger\cdot U \tag{1.38}$$

  has eigenvalues σ^* that are the complex conjugates of the ones σ of the direct eigenproblem.

- Therefore to each direct mode $V_1(\mathbf{q})$ of eigenvalue $\sigma(\mathbf{q})$ there correspond ***adjoint modes*** $U_1(\mathbf{q})$ of eigenvalue $\sigma^*(\mathbf{q})$ with the same wavenumber k.

- If k in $\mathbf{q}\;\neq k'$ in $\mathbf{q}'$ then

$$\big\langle D\cdot V_1(\mathbf{q}),\,U_1(\mathbf{q}')\big\rangle \;=\; \big\langle L\cdot V_1(\mathbf{q}),\,U_1(\mathbf{q}')\big\rangle \;=\; 0\;. \tag{1.39}$$

- For $\mathbf{q}$ with the same wavenumber k, one has usually non degenerate eigenvalues:

$$\text{if } k \text{ in } \mathbf{q} \;=\; k \text{ in } \mathbf{q}' \;\text{ but }\; \mathbf{q}\neq\mathbf{q}'\;,\quad \sigma=\sigma(\mathbf{q}) \;\neq\; \sigma'=\sigma(\mathbf{q}')\;. \tag{1.40}$$

- Consequently one can show that

$$\mathbf{q}\neq\mathbf{q}' \quad\Longrightarrow\quad \big\langle D\cdot V_1(\mathbf{q}),\,U_1(\mathbf{q}')\big\rangle \;=\; \big\langle L\cdot V_1(\mathbf{q}),\,U_1(\mathbf{q}')\big\rangle \;=\; 0\;. \tag{1.41}$$

- Normalizing the adjoint modes such that

$$\forall\mathbf{q}\;,\quad \langle D\cdot V_1(\mathbf{q}),\,U_1(\mathbf{q})\rangle \;=\; 1\;, \tag{1.42}$$

  we find that the amplitudes in (1.35) are given by

$$\boxed{A(\mathbf{q}) \;=\; \langle D\cdot V,\,U_1(\mathbf{q})\rangle}\;. \tag{1.43}$$

Physical meaning of an adjoint mode: 'receptivity function'

In order to analyze the physics behind adjoint modes, let us consider briefly a (linearized) ***forcing problem***

$$D\cdot\partial_t V \;=\; L\cdot V \;+\; F \tag{1.44}$$

with $F=F(x,z,t)$ the ***forcing terms***, corresponding to source terms in the vorticity and heat equation. Seeking solutions of the form

$$V \;=\; \sum_{\mathbf{q}} A(\mathbf{q},t)\;V_1(\mathbf{q})\;,$$

[3] This is very often the case, at least this works for RBT... and this will work for PPF, see chapter 2...

we obtain

$$\sum_{\mathbf{q}} \frac{dA}{dt}(\mathbf{q},t)\ D\cdot V_1(\mathbf{q}) \ = \ \sum_{\mathbf{q}} \sigma(\mathbf{q})A(\mathbf{q},t)\ D\cdot V_1(\mathbf{q}) \ + \ F\ .$$

With a projection onto $U_1(\mathbf{q})$, we find the *'amplitude equations'*

$$\frac{dA}{dt}(\mathbf{q},t) \ = \ \sigma(\mathbf{q})A(\mathbf{q},t) \ + \ \langle F,\, U_1(\mathbf{q})\rangle$$

Hence the ***forcing term*** in the equation for $A(\mathbf{q},t)$ reads

$$\langle F,\, U_1(\mathbf{q})\rangle \ = \ \int_{x=0}^{\lambda_c}\int_{z=-1/2}^{1/2} F(x,z,t)\cdot U_1^*(\mathbf{q};x,z)\ \frac{dx}{\lambda_c}\ dz\ .$$

Thus the components of $U_1(\mathbf{q})$ measure the ***'receptivity'*** of the mode $V_1(\mathbf{q})$ to ***perturbation***.

1.3.2 Adjoint problem & adjoint modes in slip RBT

Exercise 1.2 ***Adjoint problem in slip RBT***

Denoting $U=(\psi_a,\theta_a)$, calculate analytically the adjoint problem of the RBT linearized problem, with slip boundaries. Focus on the case of Fourier modes in x, of x-wavenumber $k\neq 0$.

Indications:

Start with the calculation of $D^\dagger$. It will be useful to use ***recursive integrations by parts***: if u and v are functions of z of class C^n, one has

$$\int uv^{(n)}\ dz \ = \ \Big[uv^{(n-1)} \ - \ u'v^{(n-2)} \ + \ u''v^{(n-3)} \ + \ ... \ + \ (-1)^{n-1}u^{(n-1)}v\Big] \ + \ (-1)^n\int u^{(n)}v\ dz$$

which can be explicited with the help of this table:

	Column A Derivatives of u	Column B Derivatives of v
$+$	u	$v^{(n)}$
$-$	$u^{(1)}$	$v^{(n-1)}$
	$\vdots$	$\vdots$
$(-1)^n$	$u^{(n)}$	v

and of this rule: pair the 1st entry of column A with the 2nd entry of column B, the 2nd entry of column A with the 3rd entry of column B, etc... with alternating signs (beginning with the positive sign)...

Solution:

$$D^\dagger \ = \ D\ , \quad [L_R^\dagger\cdot U]_1 \ = \ -\Delta\Delta\psi_a \ - \ ik\theta_a\ , \quad [L_R^\dagger\cdot U]_2 \ = \ \Delta\theta_a \ + \ Rik\psi_a\ . \tag{1.45}$$

Exercise 1.3 ***Adjoint critical mode in RBT with slip boundaries***

For $k=k_c=\pi/\sqrt{2}$, $R=R_c=27\pi^4/4$, to the critical mode (1.32), check that there corresponds a neutral ***adjoint critical mode*** U_{1c}, and calculate it with the normalization condition (1.42).

Solution:

$$U_{1c} \ = \ \frac{2}{1+P^{-1}}(-i2\sqrt{2}/(9\pi^3),\,1)\ \exp(ik_cx)\ \cos(\pi z)\ . \tag{1.46}$$

1.4 Weakly Nonlinear Analysis of slip RBT

We seek, for R close to R_c or

$$\epsilon \;=\; R/R_c - 1 \;\ll\; 1 \;, \tag{1.47}$$

which is denoted as the 'bifurcation parameter', an approximate solution of the nonlinear problem (1.13) of the form (1.35),

$$V \;=\; \sum_{\mathbf{q}} A(\mathbf{q},t)\; V_1(\mathbf{q}) \;. \tag{1.48}$$

Following Haken (1983) *'Long-living systems slave short-living systems'*, we distinguish

- ***active modes*** that correspond to $\mathbf{q} = \mathbf{q}_c = (k_c, +, 1)$ or $\mathbf{q}_c^* = (-k_c, +, 1)$ and are long-living

$$\sigma(\mathbf{q},R) \;\sim\; \epsilon/\tau_0 \tag{1.49}$$

  with

$$\tau_0 \;=\; 2\;(3\pi^2)^{-1}\;(1+P^{-1}) \tag{1.50}$$

  the characteristic time of the instability,

- from the ***passive modes*** that correspond to $\mathbf{q} \neq \mathbf{q}_c, \mathbf{q}_c^*$ and are short-living (rapidly damped)

$$\sigma(\mathbf{q},R) \;<\; \sigma_1 \;<\; 0 \;. \tag{1.51}$$

We assume that, possibly after a short transient, the active modes dictate the dynamics. The amplitudes are assumed to be ***slowly varying***

$$\forall \mathbf{q} \;,\quad \frac{dA}{dt}(\mathbf{q},t) \;=\; O(\epsilon\; A(\mathbf{q},t)) \;. \tag{1.52}$$

Thus,

$$\boxed{V \;=\; V_a \;+\; V_\perp} \quad \text{with} \quad \boxed{V_a \;=\; A_{1c}V_{1c} \;+\; c.c.} \;\text{the ***active modes***},\; V_a \;\ll\; 1 \;, \tag{1.53}$$

$$V_\perp \;=\; \sum_{\mathbf{q}\neq\mathbf{q}_c,\mathbf{q}_c^*} A(\mathbf{q},t)\; V_1(\mathbf{q}) \;\text{the ***passive modes***},\; V_\perp \;\ll\; V_a \;. \tag{1.54}$$

In the amplitude equations for the passive modes,

$$\frac{dA}{dt}(\mathbf{q},t) \;=\; \sigma(\mathbf{q},R)A(\mathbf{q},t) \;+\; \sum_{\mathbf{q}_1}\sum_{\mathbf{q}_2} A(\mathbf{q}_1,t)A(\mathbf{q}_2,t)\,\langle N_2(V_1(\mathbf{q}_1),V_1(\mathbf{q}_2)),\, U_1(\mathbf{q})\rangle \;, \tag{1.55}$$

we may neglect dA/dt and consider that these modes are created by the active ones, through nonlinear effects. The passive modes are therefore obtained by ***quasistatic elimination***

$$0 \;=\; \sigma(\mathbf{q},R)A(\mathbf{q},t) \;+\; \sum_{\mathbf{q}_1=\mathbf{q}_c,\mathbf{q}_c^*}\;\sum_{\mathbf{q}_2=\mathbf{q}_c,\mathbf{q}_c^*} A(\mathbf{q}_1,t)A(\mathbf{q}_2,t)\,\langle N_2(V_1(\mathbf{q}_1),V_1(\mathbf{q}_2)),\, U_1(\mathbf{q})\rangle \tag{1.56}$$

which amounts here, for 'symmetry' reasons[4], to

$$0 \;=\; L_R\cdot V_\perp \;+\; N_2(V_a,V_a) \;. \tag{1.57}$$

[4] The nonlinear terms $N_2(V_a,V_a)$ may create only passive modes, of x-wavenumbers 0 or $\pm 2k_c$ which are quite different from k_c.

Exercise 1.4 ***Quasistatic elimination of the passive mode in slip RBT***

In slip RBT, denoting $A = A_{1c}$ the amplitude of the critical mode, show with Mathematica that

$$[N_2(V_a,V_a)]_1 = 0\ , \quad [N_2(V_a,V_a)]_2 = B\ \sin(2\pi z) \tag{1.58}$$

with B a real number,

$$B = 3\pi^3 A^2\ . \tag{1.59}$$

Next, solve (1.57), showing that

$$\boxed{V_\perp = A^2 V_{20}} \quad \text{with} \quad V_{20} = (0,\,\Theta_2) = \left(0,\,\frac{3\pi}{4}\ \sin(2\pi z)\right)\ , \tag{1.60}$$

and explain the physics behind.

Exercise 1.5 ***Passive mode in slip RBT first control the Nusselt number***

Show that the passive mode that you have calculated controls the value of the Nusselt number

$$Nu = \frac{\Phi_{\text{heat with conduction \& convection}}}{\Phi_{\text{heat with conduction only}}} \tag{1.61}$$

with Φ_{heat} the average heat flux that goes from the hot bottom plate to the cold top plate.

Indication: you must prove that $Nu - 1 \propto A^2$.

Solution:

$$Nu - 1 = \frac{3\pi^2}{2} A^2\ . \tag{1.62}$$

To determine A, we obtain, by projection of (1.13) onto the adjoint critical mode U_{1c}, the ***amplitude equation***

$$\frac{dA}{dt} = \frac{\epsilon}{\tau_0} A + \langle N_2(V,V),\, U_{1c}\rangle\ . \tag{1.63}$$

The nonlinear terms in $N_2(V,V)$ that have a nonzero projection on $U_1(\mathbf{q}_c)$ are ***'resonant'***.

Exercise 1.6 ***Resonant terms in slip RBT at order*** A^3

Compute with Mathematica the resonant terms in $N_2(V,V)$, and explain their physics.

Solution:

$$[N_2(V,V)\ \text{resonant}]_1 = 0\ , \quad [N_2(V,V)\ \text{resonant}]_2 = -\frac{9\pi^4}{2} A^3\ \cos(k_c x)\ \cos(\pi z)\ \cos(2\pi z)\ . \tag{1.64}$$

Exercise 1.7 ***Saturation in slip RBT***

Show that $\langle N_2(V,V),\, U_{1c}\rangle = -gA^3$ and compute the ***saturation coefficient***

$$g = (9/8)\pi^4/(1+P^{-1})\ . \tag{1.65}$$

Deduce from this and the knowledge of τ_0 an analytical expression of the Nusselt number in weakly nonlinear roll solutions,

$$Nu = 1 + 2\epsilon\ . \tag{1.66}$$

Comments:

'Solutions' refers to the stationary solutions (1.68) of the final amplitude equation (1.67). An important consequence of (1.66) is that $Nu - 1 \propto \delta T/(\delta T)_c - 1$, with $(\delta T)_c$ the critical value of the temperature difference. This is confirmed by experiments, see Fig. 1.6.

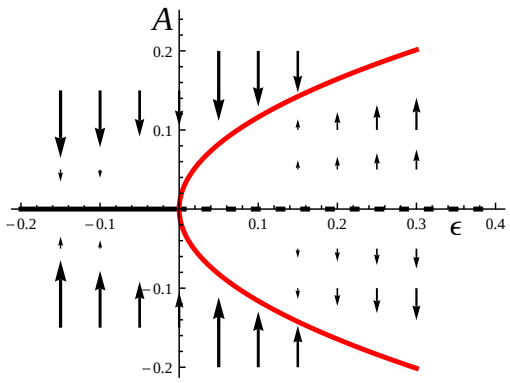

Fig. 1.2 : ***Bifurcation diagram*** of the amplitude equation (1.67). The curves in black and grey (red online) show the stationary solutions, or 'fixed points'; with the continuous lines: stable solutions; with the dashed line: unstable solution. The arrows show vectors $(0,\, dA/dt)$ when $A(t)$ evolves according to eq. (1.67), from an initial condition which is not a fixed point.

In conclusion, the ***amplitude equation*** (1.63) assumes the form

$$\boxed{\frac{dA}{dt} \;=\; \frac{\epsilon}{\tau_0} A \;-\; g A^3} \quad \text{with} \quad g \in \mathbb{R}^{+*} \; . \tag{1.67}$$

This is the generic equation of a ***supercritical pitchfork bifurcation***. It is easy to calculate the stationary solutions, or 'fixed points', of eq. (1.67):

$$\begin{aligned} \forall \epsilon \quad &, \quad A \;=\; 0 \; , \\ \forall \epsilon > 0 \quad &, \quad A \;=\; \pm \sqrt{\epsilon/(\tau_0 g)} \; , \end{aligned} \tag{1.68}$$

and to construct a ***bifurcation diagram*** in the plane (ϵ, A) (bifurcation parameter, amplitude) plotting these solutions, that depend on ϵ, and arrows parallel to the A-axis indicating dA/dt. From the direction of these arrows, the trajectories of the dynamical system (1.67), which are line segments, can be immediately deduced. From this, the stability properties of the stationary solutions ensue... The result is shown in Fig. 1.2, which displays a *'pitchfork'*; moreover, the interesting non-vanishing stationary solutions exist only for $\epsilon > 0$ i.e. *above* (*'super'* in latin) onset; all this explain the name of the bifurcation...

1.5 A glimpse at the Lorenz model and Chaos

Considering the WNL solution found here,

$$V \;=\; V_a \;+\; V_\perp \;+\; h.o.t. \tag{1.69}$$

with

$$V_a \;=\; A V_{1c} \;+\; c.c. \;=\; A \left(3\sqrt{2}\pi \, \sin(k_c x),\, 2\cos(k_c x)\right) \, \cos(\pi z) \; , \tag{1.70}$$

$$V_\perp \;=\; A^2 V_{20} \;=\; A^2 \left(0,\, \tfrac{3\pi}{4} \sin(2\pi z)\right) \; , \tag{1.71}$$

gave in 1963 to Edward Lorenz, an American mathematician and meteorologist, the idea to study thermoconvection flows containing the same contributions, but with 3 different amplitudes A, B and C,

$$\psi \;=\; A \, \sin(k_c x) \, \cos(\pi z) \; , \quad \theta \;=\; B \, \cos(k_c x) \, \cos(\pi z) \;+\; C \, \sin(2\pi z) \; . \tag{1.72}$$

By inserting this ansatz into the Boussinesq equations, renormalizing time and the amplitudes (A, B, C) to define new ones (X, Y, Z), and disregarding a term in the heat equation, that cannot be balanced, he obtained the ***'Lorenz system'***

$$\left\{ \begin{array}{rcl} P^{-1}\dot{X} & = & Y - X \\ \dot{Y} & = & rX - Y - XZ \\ \dot{Z} & = & -bZ + XY \end{array} \right. \tag{1.73}$$

with

$$r = R/R_c \, , \quad b = 8/3 \, . \tag{1.74}$$

One can easily show that, for $r < 1$, the conduction solution

$$X = Y = Z = 0$$

is stable, whereas it becomes unstable if $r > 1$. Two new fixed points appear then, which correspond to weakly nonlinear thermoconvection rolls,

$$X = Y = \pm \sqrt{b(r-1)} \, , \quad Z = r - 1 \, . \tag{1.75}$$

This is quite coherent with the theory developped in Sections 1.2 and 1.4.

By analyzing the stability of the roll solutions (1.75) in the framework of the model (1.73), one can show that, for Prandtl numbers $P > 11/3$, these solutions undergo at sufficiently large R (or r) a ***secondary oscillatory instability***, with temporal eigenvalues of the form $\pm i\omega$ with $\omega \in \mathbb{R}$ (see the Pb. 1.1). Numerical simulations show that this secondary instability leads to ***'chaos'***, i.e., a dynamic behaviour which displays a ***sensitive dependence on the initial condition***. This is demonstrated in the movie available on YouTube

Simple Model of the Lorenz Attractor
https://www.youtube.com/watch?v=FYE4JKAXSfY .

This movie shows, in the phase space (X, Y, Z), how three nearby trajectories, which correspond first to 'oscillatory convection', suddenly diverge, and explore a 'large region' of phase space in a seemingly 'random' manner. The 'region' explored has a structure, it is in fact a ***'strange attractor'***. It can be thought of as a 'collection' of trajectories which are *all* unstable. This remarkable finding, published in Lorenz (1963), attracted the attentions of many scientists. Their work on this topics has lead to the development of the ***'theory of chaos'*** in the 1970s - 1980s, as illustrated by the treatise Bergé *et al.* (1984). The title of this treatise, *Order within Chaos: Towards a Deterministic Approach to Turbulence*, is meaningful... Indeed, the great relevance of continuum thermomechanics suggests that the randomness characteristic of Turbulence rests on a deterministic dynamics... Coming back to slip RBT, the Lorenz model has to be seen as a crude model, but the fact that thermoconvection takes, after a secondary instability, the form of a weakly turbulent flow at high Rayleigh numbers, is an interesting lesson. We could ask what happens at quite large Rayleigh numbers in slip RBT, but, if we want to do good and quantitative physics, we have now to switch to the more realistic case of no-slip boundary conditions...

1.6 Numerical Linear Analysis of no-slip RBT

Exercise 1.8 ***Numerical linear stability analysis of no-slip RBT with a spectral method***

To solve with Mathematica the linear RBT problem using no-slip boundary conditions, for $P = 1$, use a ***spectral expansion*** of the eigenfunctions of the Fourier modes, in $\exp(ikx)$, as a sum of simple polynomial functions that fulfill the boundary conditions:

$$\Psi(z) \;=\; \sum_{n=1}^{N} \Psi_n F_n(z) \quad \text{with} \quad F_n(z) \;=\; (1/2-z)^2\,(z+1/2)^2\,T_{2n-2}(2z)\;, \tag{1.76}$$

$$\Theta(z) \;=\; \sum_{n=1}^{N} \Theta_n f_n(z) \quad \text{with} \quad f_n(z) \;=\; (1/2-z)\,(z+1/2)\,T_{2n-2}(2z)\;, \tag{1.77}$$

T_n the n^{th} Chebyshev polynomial of the first kind, N the number of z-modes.

1 Plot a few functions F_n and f_n, and the ***Gauss-Lobatto collocation points***

$$z_m \;=\; \cos[m\pi/(2N+1)]/2 \quad \text{for} \quad m \in \{1,2,\cdots,N\}\;, \tag{1.78}$$

and comment.

2 By evaluating the vorticity and heat equation at the Gauss-Lobatto collocation points, construct by blocks matrices that represent the operators D and L_R applied to the vector of the expansion coefficients $V_{\rm num} \;=\; (\Psi_1,\cdots,\Psi_N,\Theta_1,\cdots,\Theta_N)$. Note that n in equations (1.76) and (1.77) is a 'column index', m in equation (1.78) is a 'line index'.

3 With the command `Eigenvalues`, find a numerical approximation of the temporal eigenvalues $\sigma(k,R)$ for k fixed. Check the physical relevance of this 'spectrum'.

4 Sort these eigenvalues to find the most relevant one $\sigma_1(k,R)$.

5 Define the neutral Rayleigh number $R_0(k)$ by finding a root of $\sigma_1(k,R) = 0$. Plot the corresponding neutral curve Fig. 1.3.

6 Finally, find the critical parameters by minimizing the neutral Rayleigh number.
Compare with the slip case and discuss the physics.

Elements of solution and comments:

As it is visible on Fig. 1.3, the critical Rayleigh number found,

$$R_c \;=\; 1708\;, \tag{1.79}$$

larger than the one (1.29) found with slip boundary conditions, demonstrates that the no-slip boundary conditions have, naturally, a ***stabilizing effect***. The critical wavelength,

$$\lambda_c \;=\; 2.01\;, \tag{1.80}$$

smaller than the one (1.31) found with slip boundary conditions, shows that the thermoconvection rolls require stronger gradients... and are almost 'squared'...

Further computations show that the characteristic time of the instability in the no-slip case

$$\tau_0 \;=\; 0.0509 \;+\; 0.0260P^{-1} \tag{1.81}$$

has the same form of Prandtl-number dependence than the characteristic time of the instability in the slip case (1.50).

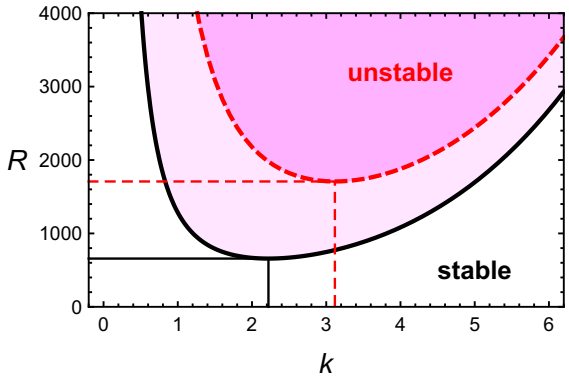

Fig. 1.3 : The continuous line shows the ***neutral curve*** $R_0(k)$ ***of slip RBT***, the dashed line the ***neutral curve of no-slip RBT***. The straight lines show the critical parameters.

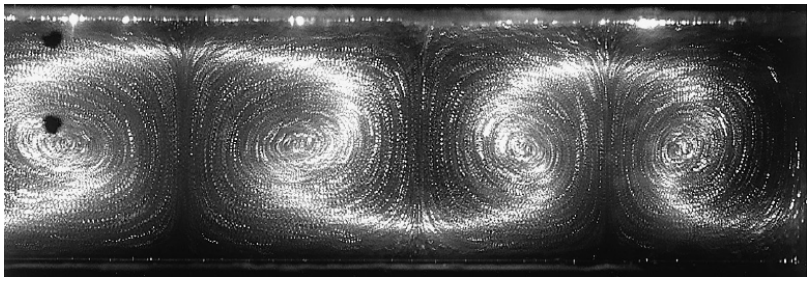

Fig. 1.4 : Experimental visualisation by Stasiek (1997) of ***thermoconvection rolls*** in a glycerol-filled cavity of 180 mm long, 60 mm wide and 30 mm high. The Prandtl number $P = 12.5\ 10^3$ and the Rayleigh number $R = 12\ 10^3$. A vertical 'plane' of thickness 2 - 3 mm in width is illuminated. Small drops, of diameter 50 - 80 μm, of thermochromic liquid crystals are dispersed in the glycerol. The photograph is taken with 8 flashes at a time interval of 6 seconds: the successive positions of the drops show the flow streamlines. Moreover, a selective reflection of light by the thermochromic liquid crystals shows in bright the isotherm corresponding roughly to the average T_0 of the temperatures of the horizontal boundaries.

1.7 Short review of no-slip RBT

A ***weakly nonlinear analysis*** can also be performed numerically, but with care to explicit the Prandtl number dependence of the solutions. Thus, for instance, Schlüter *et al.* (1965) showed that the Nusselt number is given, in the weakly nonlinear regime, by

$$Nu \;=\; 1 + (0.699 \;+\; 0.00472P^{-1} \;+\; 0.00832P^{-2})^{-1}\epsilon \;+\; O(\epsilon^2)\ . \tag{1.82}$$

There is a strong Prandtl-number dependence, especially, as $P \to 0$, which is not at all present in the slip case: compare with eq. (1.66). This illustrates the fact that nonlinear properties of a model are much more sensitive to the boundary conditions than linear properties... Of course, ***strongly nonlinear computations*** can also be performed; this will be illustrated during the oral Lecture... In particular, I will display numerical results that agree well with the experiment at large Prandtl number of Stasiek (1997), shown in Fig. 1.4.

Other ***experimental results*** that confirm the bifurcation to rolls in no-slip RBT are presented for instance in Hu *et al.* (1993). Their cylindrical setup is shown Fig. 1.5a : RBT in CO_2 under pressure is realized in a flow cell of thickness $d = 1.05$ mm and diameter $43d$, heated from below with a ohmic film heater, cooled from above with a water bath. The thermoconvection flows, e.g., the roll pattern of Fig. 1.5b, are visualized with the *shadowgraph method*: the refractive index of

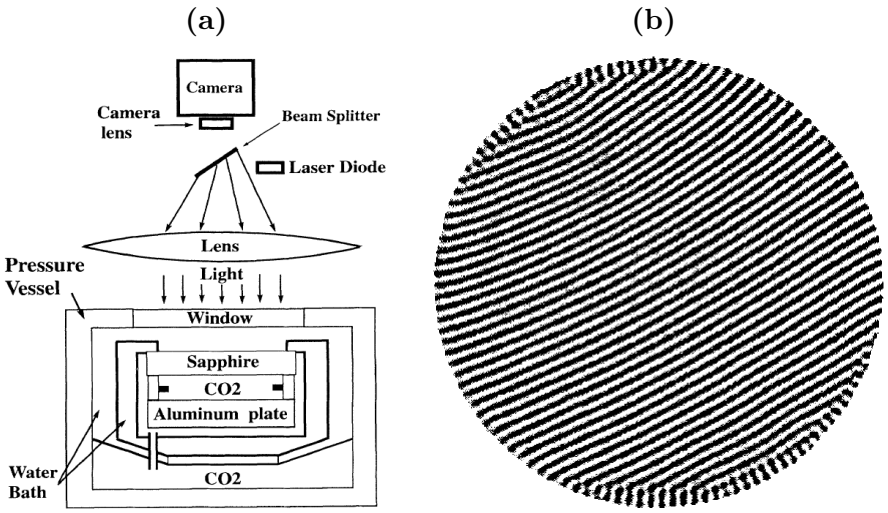

Fig. 1.5 : **(a)** Section of the ***Rayleigh-Bénard Thermoconvection setup*** of Hu *et al.* (1993). **(b)** Top view of a roll pattern obtained near onset, for $R = 1.04R_c$.

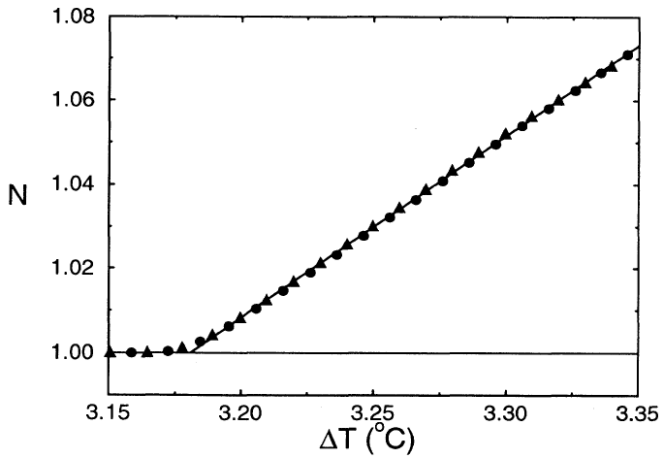

Fig. 1.6 : Nusselt number measured by Hu *et al.* (1993) in their ***RBT experiment***, vs. the applied temperature difference. The triangles are for increasing δT, the circles, for decreasing δT.

the fluid depends on T, thus the light rays that pass through the flow cell are more or less deflected depending on T, and an image of an 'average temperature field' is obtained. The knowledge of the power injected in the film heater allows the determination of the heat flux Φ_{heat} that passes through the convection cell. Hence, the Nusselt number Nu, defined in eq. (1.61), can be measured. Typical results are shown in Fig. 1.6. This agrees with the weakly nonlinear formula (1.82). The Fig. 1.6 thus shows clearly a ***supercritical bifurcation***, without any hysteresis.

Especially at small Prandtl numbers, nonlinear rolls become quickly unstable when the Rayleigh number increases, as shown for instance in Plapp (1997); Bodenschatz *et al.* (2000). These ***secondary instabilities*** have been studied in great details by Busse and coworkers (Busse 2003). After ***tertiary instabilities***, etc... this leads at high Rayleigh numbers to ***turbulent flows***. Relevant informations on turbulent RBT can be found in the review Ahlers *et al.* (2009)... These scenarios of a ***progressive transition to turbulence through a cascade of instabilities*** can be coined as ***'globally supercritical'***.

1.8 Problem

Problem 1.1 ***Lorenz model of slip Rayleigh-Bénard Thermoconvection***

[*Part of the test of February* 2016]

Following Lorenz, we explore a model of slip RBT where the streamfunction

$$\psi \;=\; A(t)\;\sin(kx)\;\cos(\pi z)\;, \tag{1.83}$$

and the temperature perturbation

$$\theta \;=\; B(t)\;\cos(kx)\;\cos(\pi z)\;+\;C(t)\;\sin(2\pi z)\;, \tag{1.84}$$

with $k>0$ a real number.

0 Specify the physical name and physical meaning of k.

1 Check that these fields satisfy the boundary conditions of slip RBT.

2 Write a Mathematica code to explicit, in the case of a state vector $V=(\psi,\,\theta)$ with ψ given by (1.83) and θ given by (1.84), the equations of slip RBT

$$D\cdot\partial_t V \;=\; L_R\cdot V \;+\; N_2(V,V)\;, \tag{1.85}$$

with $R>0$ the Rayleigh number. Write the solution on your copy, under the form

$$\begin{aligned}
[D\cdot\partial_t V]_1 &= \ldots\\
[L_R\cdot V]_1 &= \ldots\\
[N_2(V,V)]_1 &= \ldots\\
[D\cdot\partial_t V]_2 &= \ldots\\
[L_R\cdot V]_2 &= \ldots\\
[N_2(V,V)]_2 &= \ldots
\end{aligned}$$

where the r.h.s. are polynomials of $\dot A$, $\dot B$, $\dot C$, A, B, C (hereafter we do not recall the time dependence, and the superdots denote the time derivative), with coefficients simplified as much as possible. Also, you will use the command `TrigReduce` to expand the z-dependent factor of the coefficient of $A\,C$ in $[N_2(V,V)]_2$.

3.a Show that the vorticity equation reduces to an ordinary differential equation (ODE) of order 1 coupling the amplitudes A and B, that you will explicit.

3.b By identifying the coefficients of $\cos(kx)\;\cos(\pi z)$ and $\sin(2\pi z)$ in the heat equation, obtain two ODE of order 1 coupling the amplitudes A, B and C.

3.c If we retain, as Lorenz did it, only these three ODE, are the equations of slip RBT exactly fulfilled ? Conclude on the nature of the Lorenz model.

4 To further reduce the form of the model, implement the changes of variables

$$t' \;=\; D_1\,t\;,\quad A\;=\;\frac{\sqrt{2}D_1}{k\pi}\,X\;,\quad B\;=\;\frac{\sqrt{2}D_1^3}{k^2\pi R}\,Y\;,\quad C\;=\;\frac{D_1^3}{k^2\pi R}\,Z\quad\text{with}\quad D_1\;=\;k^2+\pi^2\;. \tag{1.86}$$

Show that the three ODE reduce to the ***'Lorenz system'***

$$\left\{\begin{array}{rcl} P^{-1}\dot{X} &=& Y - X \\ \dot{Y} &=& rX - Y \ - \ XZ \\ \dot{Z} &=& -bZ \ + \ XY \end{array}\right. \tag{1.87}$$

with now $\dot{X} = dX/dt'$, $\dot{Y} = dY/dt'$, $\dot{Z} = dZ/dt'$, P the Prandtl number, r and b parameters that depend on R and k. Specify physical names and the physical meaning of r.

5 Explain the physical meaning of the null fixed point $X = Y = Z = 0$ of the Lorenz system.

6 Show by a systematic calculation that other ***fixed points*** appear as soon as r exceeds a value that you will determine. Represent those in the planes (r,X) and (r,Y). What physical phenomenon is revealed by these calculations ?

7 By an 'optimization' calculation based on this study of the Lorenz system, determine the critical value R_c of the Rayleigh number R for which thermoconvection sets in first, and the corresponding critical value k_c of k.

8 From now on, we consider the case $k = k_c$. Specify in this case the expressions of r and b in terms of the parameter $\epsilon = R/R_c - 1$.

9 For $\epsilon > 0$, specify the expressions of X_0, Y_0, Z_0, the amplitudes corresponding to the fixed point of question 6 with X_0 and $Y_0 > 0$, in terms of b and ϵ.
Hereafter, avoid as much as possible to replace b by its actual value, to shorten the expressions.

10.a In order to study the ***secondary stability*** of this fixed point, calculate, in terms of P, b and ϵ, the matrix $[M]$ of the linearized evolution operator that governs the dynamics of small perturbations of (X_0, Y_0, Z_0). I.e., if we denote the Lorenz system

$$\dot{X} \ = \ F_1(X,Y,Z) \ , \quad \dot{Y} \ = \ F_2(X,Y,Z) \ , \quad \dot{Z} \ = \ F_3(X,Y,Z) \ ,$$

$$[M] \ = \ \begin{bmatrix} \partial_X F_1 & \partial_Y F_1 & \partial_Z F_1 \\ \partial_X F_2 & \partial_Y F_2 & \partial_Z F_2 \\ \partial_X F_3 & \partial_Y F_3 & \partial_Z F_3 \end{bmatrix}_{X_0,\ Y_0,\ Z_0} \quad .$$

10.b Calculate the characteristic polynomial $\chi(\sigma) \ = \ \det(\sigma[I] - [M])$ where $[I]$ is the identity matrix.

10.c We admit that the eigenvalues of $[M]$, the so-called ***'temporal eigenvalues'***, are of the form

$$\{\sigma_1,\, \sigma_2,\, \sigma_3\} \ = \ \{q + i\omega,\, q - i\omega,\, -s\} \quad \text{with} \quad q \in \mathbb{R},\, \omega \in \mathbb{R}^{+*},\, s \in \mathbb{R}^{+*} \ .$$

What would signal a change of sign of q, from $q < 0$ for small $\epsilon > 0$, to $q > 0$ for $\epsilon > \epsilon_1$?
Right at the point where this change of sign would occur, establish a relation between $\epsilon = \epsilon_1$, P and b.
Check that, for sufficiently large P, a solution ϵ_1 exists in terms of ϵ.

10.d For $P = 11$, give a lower bound of ϵ for the ***onset of chaos*** through small perturbations of the studied fixed point. Translate this bound in terms of r and R.

Chapter 2

Transition to Turbulence in Open Shear Flows

This chapter corresponds to the Sessions 6 and 7 of 2016-2017.

2.1 Generalities

Open Shear Flows are often encountered in Aerodynamics, think for instance to the Flow around an Airfoil, and also in Hydrodynamics, think for instance to Pipe Flow or Channel Flow.

For the sake of simplicity, we focus here on ***2D xz Flows***, such as the Boundary Layer Flow over a flat plate (Fig. 2.1a) or Flows in channels (Fig. 2.1b). It is assumed that in the y direction, the boundaries of the system are far away and have a little influence. Not too close to the leading edge, the Boundary Layer over a flat plate (Fig. 2.1a) is quasi invariant under translations in the x direction. To simplify, we will consider hereafter ***Parallel Open Shear Flows*** that are strictly invariant under translations in the x direction. They are generally of the form

$$\overline{\mathbf{v}} \;=\; \overline{\mathbf{v}}_0 \;=\; U(z)\,\overline{\mathbf{e}}_x\;,\quad \widehat{p} \;=\; p+\rho g Z \;=\; \widehat{p}_0 \;=\; -\,Gx\;, \tag{2.1}$$

with Z the vertical coordinate, G the pressure gradient necessary to sustain the Flow if the fluid is viscous. If the fluid is inviscid, $G=0$.
We want to analyze the ***stability*** of such basic Flows.
For this purpose, we introduce ***perturbations*** of velocity and pressure, i.e., we write

$$\overline{\mathbf{v}} \;=\; \overline{\mathbf{v}}_0 \;+\; \overline{\mathbf{u}}\;,\quad \widehat{p} \;=\; \widehat{p}_0 \;+\; p'\;. \tag{2.2}$$

The Navier-Stokes or Euler equation then give

$$\partial_t\overline{\mathbf{u}} \;+\; U' u_z\overline{\mathbf{e}}_x \;+\; U\partial_x\overline{\mathbf{u}} \;+\; (\overline{\mathbf{u}}\cdot\overline{\boldsymbol{\nabla}})\overline{\mathbf{u}} \;=\; -\,(1/\rho)\overline{\boldsymbol{\nabla}}p' \;+\; \nu\overline{\boldsymbol{\Delta}}\overline{\mathbf{u}}\;. \tag{2.3}$$

Moreover, we assume that the fluid is incompressible,

$$\mathrm{div}\overline{\mathbf{u}} \;=\; 0\;. \tag{2.4}$$

We introduce dimensionless equations using a length scale h which is the thickness of the mixing layer, the half-width of the channel, ... For the velocity scale, we use

$$U_0 \;=\; \max_z U(z)\;. \tag{2.5}$$

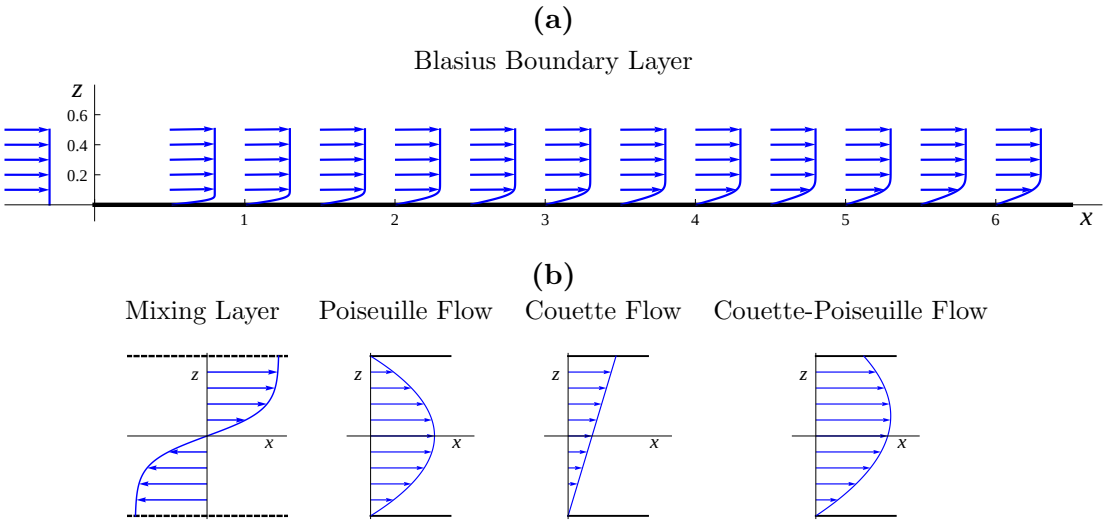

Fig. 2.1 : Examples of 2D ***Open Shear Flows***. **(a)** A slightly non-parallel Flow. **(b)** Parallel Flows.

Finally the unit of time is the advection time, or inertial time, $t_0 = h/U_0$.
The dimensionless form of the Navier-Stokes or Euler equation (2.3) is then

$$\partial_t \overline{\mathbf{u}} + U' u_z \overline{\mathbf{e}}_x + U \partial_x \overline{\mathbf{u}} + (\overline{\mathbf{u}} \cdot \overline{\boldsymbol{\nabla}}) \overline{\mathbf{u}} = - \overline{\boldsymbol{\nabla}} p'' + R^{-1} \overline{\boldsymbol{\Delta}} \overline{\mathbf{u}} \,, \tag{2.6}$$

with[1]

$$\text{the } \textbf{\textit{Reynolds number}} \quad R = U_0 h/\nu \,, \quad R = \infty \text{ in an inviscid fluid.} \tag{2.7}$$

Contrarily to the problem of the Rayleigh-Bénard Thermoconvection which has been studied in the chapter 1, the basic flow creates an anisotropy in the xy plane. Despite this, we assume that it is relevant to focus, firstly, on perturbations that are ***2D xz***. It is convenient then to use a perturbation ***streamfunction*** ψ such that

$$\overline{\mathbf{u}} = \overline{\mathbf{curl}}(\psi \, \overline{\mathbf{e}}_y) = (\overline{\boldsymbol{\nabla}} \psi) \times \overline{\mathbf{e}}_y = - (\partial_z \psi) \, \overline{\mathbf{e}}_x + (\partial_x \psi) \, \overline{\mathbf{e}}_z \,. \tag{2.8}$$

We also eliminate the pressure by solving, instead of (2.6), the vorticity equation, which reduces to its component in the y direction,

$$\partial_t(-\Delta\psi) + \left[\partial_z\left(\overline{\mathbf{u}} \cdot \overline{\boldsymbol{\nabla}} u_x\right) - \partial_x\left(\overline{\mathbf{u}} \cdot \overline{\boldsymbol{\nabla}} u_z\right)\right] = R^{-1}\Delta(-\Delta\psi) + U\partial_x(\Delta\psi) - U''(\partial_x\psi) \,. \tag{2.9}$$

Since the perturbations in these fluid systems are characterized by only one field, the streamfunction ψ, there is no need to introduce a new notation for the local state vector[2]. This streamfunction fulfills

$$\boxed{D \cdot \partial_t \psi = L_R \cdot \psi + N_2(\psi,\psi)} \tag{2.10}$$

$$\text{with} \quad D \cdot \partial_t \psi = - \Delta \partial_t \psi \,, \quad L_R \cdot \psi = R^{-1}\Delta(-\Delta\psi) + U\partial_x(\Delta\psi) - U''(\partial_x\psi), \tag{2.11a}$$

$$N_2(\psi,\psi) = \partial_x\left(\overline{\mathbf{u}} \cdot \overline{\boldsymbol{\nabla}} u_z\right) - \partial_z\left(\overline{\mathbf{u}} \cdot \overline{\boldsymbol{\nabla}} u_x\right) \,. \tag{2.11b}$$

The boundary conditions, at the 'plates' located at $z = z_\pm$, are,

$$\text{for a viscous fluid, no-slip,} \quad \overline{\mathbf{u}} = \overline{\mathbf{0}} \iff \partial_x\psi = \partial_z\psi = 0 \,, \tag{2.12}$$

$$\text{for an inviscid fluid, slip,} \quad u_z = 0 \iff \partial_x\psi = 0 \,. \tag{2.13}$$

[1] Do not mingle the main control parameter R of this chapter, the Reynolds number, with the main control parameter R of chapter 1, the Rayleigh number.

[2] I.e., the local state vector $V = (\psi)$.

2.2 Linear stability analysis of Plane Parallel Flows

This linear analysis relies on the calculation of normal modes of the form

$$\psi \;=\; \Psi_n(z)\;\exp(ikx+\sigma t) \;=\; \Psi_n(z)\;\exp[ik(x-c_r t)]\;\exp(kc_i t) \tag{2.14}$$

with $k \neq 0$ the ***wavenumber***[3], n another label to mark normal modes, σ the temporal eigenvalue. Most often the bulk velocity of the basic flow $\langle U \rangle_z > 0$, hence we expect normal modes that are ***waves*** traveling 'to the right' (in the x direction). For this reason we write

$$\sigma \;=\; -i\omega \;=\; -ikc \tag{2.15}$$

with c the ***complex phase velocity***, $c_r > 0$ (most often) the real phase velocity, $kc_i > 0$ (resp. < 0) the growth rate (resp. damping rate). By inserting the form (2.14) in (2.10) and linearizing, we obtain

$$\boxed{(U-c)\Delta\psi \;-\; U''\psi \;=\; (ikR)^{-1}\Delta\Delta\psi} \tag{2.16}$$

which is the ***Orr - Sommerfeld equation*** in a viscous fluid, ***Rayleigh equation*** in an inviscid fluid ($R=\infty$).
The boundary conditions at $z = z_\pm$, are,

$$\text{for a viscous fluid} \quad , \quad \psi \;=\; \partial_z\psi \;=\; 0\;, \tag{2.17}$$

$$\text{for an inviscid fluid} \quad , \quad \psi \;=\; 0\;. \tag{2.18}$$

2.2.1 Linear stability analysis of Inviscid Plane Parallel Flows

Exercise 2.1 ***Rayleigh's inflection point criterion***

Let us assume that an Inviscid Plane Parallel Flow is unstable. Therefore there exists at least one amplified normal mode (2.14), more simply

$$\psi \;=\; \Psi(z)\;\exp[ik(x-c_r t)]\;\exp(kc_i t)\;, \tag{2.19}$$

which corresponds to $c_i > 0$.

1 Express $\Psi''(z)$ as a function of $\Psi(z)$, $U(z)$, $U''(z)$, k and c.

2 By multiplication with a suitable function and integration over $z \in [z_-,z_+]$, show that

$$\int_{z_-}^{z_+} \left(k^2|\Psi(z)|^2 + |\Psi'(z)|^2\right)dz \;+\; \int_{z_-}^{z_+} \frac{U''(z)\;|\Psi(z)|^2}{U(z)-c}dz \;=\; 0$$

and, then,

$$\int_{z_-}^{z_+} \frac{U''(z)\;|\Psi(z)|^2}{|U(z)-c|^2}dz \;=\; 0\;. \tag{2.20}$$

3 Conclude that, if $U'' \neq 0$, U'' must change sign somewhere, i.e. there must exist an ***inflection point*** in the U-profile.

A typical example of an 'inflection-point instability' is the ***Kelvin-Helmholtz instability*** of the ***mixing layer***, which has been already approached in Plaut (2016), see also the animations on http://emmanuelplaut.perso.univ-lorraine.fr/mf/KH-e.htm.

[3] One can easily show that x-homogeneous modes are all damped.

2.2.2 Linear stability analysis of Viscous Plane Poiseuille Flow

Exercise 2.2 ***Linear stability analysis of Plane Poiseuille Flow with a spectral method***

We analyze the stability of ***Plane Poiseuille Flow*** (PPF), $U(z) = 1 - z^2$, of a ***Viscous Fluid***. For this purpose we solve the ***Orr - Sommerfeld equation*** (2.16), here rewritten with the temporal eigenvalue σ,

$$\boxed{\sigma D \cdot \Psi = -\sigma \Delta \Psi = L_R \cdot \Psi = -R^{-1} \Delta\Delta\Psi + ik(U\Delta\Psi - U''\Psi)} \tag{2.21}$$

with

$$\Delta = -k^2 + \frac{d^2}{dz^2} \tag{2.22}$$

and the boundary conditions (2.17),

$$\Psi = \Psi' = 0 \quad \text{if} \quad z = \pm 1 \ . \tag{2.23}$$

For this purpose, we use a ***spectral expansion*** of the eigenfunctions $\Psi(z)$, as a sum of simple polynomial functions that fulfill the boundary conditions:

$$\Psi(z) = \sum_{n=1}^{N} \Psi_n F_n(z) \quad \text{with} \quad F_n(z) = (z-1)^2 (z+1)^2 T_{2n-2}(z) = (z^2-1)^2 T_{2n-2}(z) \ , \tag{2.24}$$

T_n the n^{th} Chebyshev polynomial of the first kind, $N = N_z$ the number of z-modes (`Nz` in your code). We retain only the Chebyshev polynomials of even index because we know that the relevant modes correspond to $\Psi(z)$ even under $z \mapsto -z$, i.e. to modes invariant with respect to the midplane reflection symmetry $z \mapsto -z$. To check this, we should test a more general expansion...

1 Start a Mathematica code by defining the functions F_n (`F[n,z]` in your code) and the ***Gauss-Lobatto collocation points***

$$z_m = \cos[m\pi/(2N+1)] \quad \text{for} \quad m \in \{1,2,\cdots,N\} \tag{2.25}$$

(`z[m]` in your code). Plot a few functions F_n and the collocation points for various values of N, and comment.

2 By inserting (2.24) in (2.21), we get

$$\sigma \sum_n \Psi_n D \cdot F_n(z) = \sum_n \Psi_n L \cdot F_n(z)$$

which we want to be fulfilled at the collocation points (2.25):

$$\forall m \ , \quad \sigma \sum_n \Psi_n D \cdot F_n(z_m) = \sum_n \Psi_n L \cdot F_n(z_m) \ . \tag{2.26}$$

Introducing the vector of the expansion coefficients (or 'spectral coefficients')

$$V = \begin{bmatrix} \Psi_1 \\ . \\ . \\ . \\ \Psi_N \end{bmatrix} \ , \tag{2.27}$$

show that (2.26) can be written under a matrix form

$$\sigma MD \cdot V \;=\; ML \cdot V \tag{2.28}$$

$$\text{with } MD_{mn} \;=\; D \cdot F_n(z_m) \quad , \quad ML_{mn} \;=\; L \cdot F_n(z_m) \quad . \tag{2.29}$$

Note that n is a 'column index', m is a 'line index'.

3.a Define in your code the operators D and L_R acting on a general function Ψ or f of z, according to equation (2.21),

```
Dop[f_]:= ...
Lop[f_]:= ...
```

Create the square matrices MD and ML with the good dimension :

```
MatD = MatL = IdentityMatrix[Nz]
```

then, with a double loop, code the rules (2.29):

```
Do[
   Do[
      MatD[[m,n]] = ... ;
      MatL[[m,n]] = ...
     ,{m,1,Nz}]
  ,{n,1,Nz}]
```

Indication : for the derivatives with respect to z to be correctly computed, do not replace too early z by z_m; do this at the end using the `ReplaceAll` command.

3.b To show clearly the control parameters, define

```
MD[k_] = MatD;  ML[k_,R_] = MatL;
```

4 Define the spectrum of the generalized eigenvalue problem (2.28) as

```
spectrum[k_,R_]:= Eigenvalues[{ML[k,R], MD[k]}]
```

and the eigenvalue of the most relevant mode as

```
sigma1[k_?NumericQ,R_?NumericQ]:= Last[Sort[spectrum[k,R]]]
```

The `?NumericQ` will prevent Mathematica from trying to do formal computations on `sigma1`.
By setting k to a typical value, observe the evolution of the spectrum and of the most relevant eigenvalue as a function of R.
Check that PPF is stable at small R but becomes ***unstable*** at large R.

5 Code with `FindRoot` the computation of the neutral Reynolds number $R = R_0(k)$ where

$$\mathrm{Re}[\sigma_1(k,R)] \;=\; 0 \; ; \tag{2.30}$$

write

```
R0[k_?NumericQ]:= R/.FindRoot[...]
```

to prevent Mathematica from trying to compute formally $R_0(k)$.
Compute a list of values of $R_0(k)$ and plot the corresponding ***neutral curve*** Fig. 2.2. Comment.

6.a By minimizing $R_0(k)$ with respect to k, compute the ***critical parameters*** k_c, R_c, ω_c and c_c of the bifurcation of PPF to the so-called ***TS waves***[4] :

$$k_c \;=\; 1.02\;, \quad R_c \;=\; 5772\;, \quad \omega_c \;=\; 0.269\;, \quad c_c \;=\; 0.264\;. \tag{2.31}$$

Perform ***convergence tests*** by varying the number of modes N_z, for instance, saving your results at given N_z :

```
Put[{Rc,kc,omc},"RckcomcNz"<>ToString[Nz]]
```

then comparing the results obtained with $N_z - 1$ vs N_z modes. For this purpose you will load the previous file with the command

```
{Rcold,kcold,omcold} = Get["RckcomcNz"<>ToString[Nz-1]]
```

A reasonable convergence criterion is that k_c, R_c and ω_c do not change by more than 0.1% with $N_z - 1$ vs N_z modes. Determine the minimum number of modes that satisfies this criterion,

$$N_z \;=\; 18\;. \tag{2.32}$$

6.b Explain the physical meaning of the values (2.31) found for k_c and c_c.

7 With the `Eigensystem` command, find the vector V (2.27) that represents the ***critical mode*** eigenfunction $\Psi(z)$. By coding the summation (2.24), compute this function $\Psi(z)$. Normalize it such that

$$\Psi(z=0) \;=\; 1\;, \tag{2.33}$$

plot its modulus, and comment.

8 Compute a streamfunction that represents PPF with a TS wave

$$\overline{\mathbf{v}} \;=\; \overline{\mathbf{v}}_0 \;+\; \overline{\mathbf{u}} \tag{2.34}$$

with $\overline{\mathbf{u}}$ deriving from

$$\psi \;=\; A\;\Psi(z)\;\exp(ik_c x) \;+\; c.c.\;, \tag{2.35}$$

A a 'small' amplitude that one cannot compute with such a linear theory, and that you will vary. For this purpose, introduce a streamfunction $\Psi_0(z)$ that represents pure PPF. Take care of the midplane reflection symmetry $z \mapsto -z$: $\Psi_0(z)$ should be odd under $z \mapsto -z$.
Use this to plot the streamlines of PPF with a more or less developped TS wave, $A = 0$, 0.1 and 0.2.
Comment these plots, in connection with this citation of Reynolds (1895):

> *'when water is caused by pressure to flow through a uniform smooth pipe,*
> *the motion of the water is* ***direct****, i.e., parallel to the sides of the pipe,*
> *or* ***sinuous****, i.e., crossing and re-crossing the pipe,*
> *according as R is below or above a certain value'.*

9 To prepare weakly nonlinear calculations, save, with the command `Put`, the vector of the spectral coefficients (2.27) of the normalized critical mode eigenfunction $\Psi(z)$ to a file `V1.m`.

[4] TS in honour of Tollmien & Schlichting, the (german) theoreticians who predicted the existence of these waves in the Blasius Boundary Layer, during the first part of the 20^{th} century.

Exercise 2.3 ***Linear stability analysis of PPF at high Reynolds number***

1 With the program that you wrote for Ex. 2.2, using at least $N_z = 18$ spectral modes, plot the real part of the eigenvalue $\sigma(k,R)$ of the most relevant mode with a streamwise wavenumber

$$k = 0.9$$

versus $R \in [5\ 10^3, 100\ 10^3]$. Observe that this mode is amplified only in a range of Reynolds number $R \in [R_0(k), R_1(k)]$.

2 Code with `FindRoot` the computation of the high Reynolds number $R_1(k)$ at which $\mathrm{Re}[\sigma(k,R)]$ vanishes.

3 Saving the value of $R_1(k)$ to files with names `R1Nz*` and re-reading these files, implement the convergence criterion that $R_1(k)$ does not change by more than 0.01% with $N_z - 1$ vs N_z modes: if $r_{1\mathrm{low}} = R_1(k; N_z - 1)$ and $r_1 = R_1(k; N_z)$, one wants that

$$|r_1/r_{1\mathrm{low}} - 1| \ < \ 10^{-4} \ .$$

Determine according to this criterion the lowest value of N_z that one should use for this study at high Reynolds number, and an estimate of $R_1(k)$ with 2 digits.
Importantly, you should observe that you run into precision problems at high N_z. To increase the precision, define the collocation points with

```
z[m_]= N[Cos[m Pi/(2 Nz+1)],Nz]
```

Hereafter we do no more focus on $k = 0.9$ but explore a range of values of k.

4 With the value of N_z determined in question 3, construct a list `lkR0` of the couples $(k,R_0(k))$ with k the wavenumber, $R_0(k)$ the lower neutral Reynolds number, for discrete k values spanning the interval

$$0.7 \ \leq \ k \ \lesssim \ 1.1 \ .$$

Construct also a list `lkR1` of the couples $(k,R_1(k))$ with k the wavenumber, $R_1(k)$ the higher neutral Reynolds number, for discrete k values spanning the interval

$$0.8 \ \leq \ k \ \lesssim \ 1.1 \ .$$

To compute this second list, use a continuation method: start at large k and decrease k by small steps, using as an estimate of $R_1(k)$ in the `FindRoot` command the value of $R_1(k)$ computed at the previous step.
Join these two lists and plot Fig. 2.2 in linear - log scales the limit of the region where TS waves are amplified in the (k,R) plane, in the intervals

$$0.7 \ \leq \ k \ \leq \ 1.1 \ , \quad 5\ 10^3 \ \leq \ R \ \leq \ 200\ 10^3 \ .$$

5 Explain what happens as $R \to +\infty$ using a theoretical result valid in this limit.

2.3 Weakly nonlinear stability analysis of Plane Poiseuille Flow

We present here a ***simplified weakly nonlinear analysis*** of ***Viscous Plane Poiseuille Flow*** (PPF), seen as a 'generic' example of Plane Parallel Flow. This weakly nonlinear analysis is valid for small values of the bifurcation parameter

$$\epsilon \;=\; R/R_c - 1 \;\ll\; 1 \;. \tag{2.36}$$

2.3.1 Linear modes basis - Adjoint problem & adjoint modes

The idea is still to use the ***linear modes basis***. We use periodic boundary conditions under $x \mapsto x + 2\pi/k_c$. Therefore, the linear modes are characterized by $\mathbf{q} \;=\; (k,n)$ with k the x-wavenumber, integer multiple of k_c, and n an integer which indexes the z-dependence. We denote the ***critical mode***

$$\psi_{1c} \;=\; \Psi(z)\;\exp(ik_c x)\;, \tag{2.37}$$

with $\Psi(z)$ the critical streamfunction. An ***adjoint problem*** and ***adjoint critical mode*** is now defined with the method of section 1.3.

Exercise 2.4 ***Adjoint problem and adjoint critical mode in PPF***

1 Consider a Viscous Plane Parallel Flow (typically, PPF) in a channel with boundaries at $z = \pm 1$ in dimensionless units. Over the streamfunction space, the Hermitian inner product

$$\langle \psi,\, \phi \rangle \;\;=\;\; \int_{x=0}^{\lambda_c} \int_{z=-1}^{1} \psi(x,z)\;\phi^*(x,z)\;\frac{dx}{\lambda_c}\;\frac{dz}{2}\;. \tag{2.38}$$

Focusing on the case of Fourier modes in x, of wavenumber $k \neq 0$,

$$\langle \Psi(z)\;\exp(ikx),\, \Phi(z)\;\exp(ikx) \rangle \;\;=\;\; \int_{z=-1}^{1} \Psi(z)\exp(ikx)\;[\Phi(z)\exp(ikx)]^*\;\frac{dz}{2}\;. \tag{2.39}$$

Show with analytic hand-made calculations that the adjoint operators corresponding to the operators D and L_R (2.11*a*) characterizing the stability of a Plane Parallel Flow are

$$D \;=\; D^\dagger \;=\; -\,\Delta\;, \qquad L_R^\dagger \cdot \phi \;=\; -\,R^{-1}\Delta\Delta\phi \;-\; 2ikU'\partial_z\phi \;-\; ikU\Delta\phi\;. \tag{2.40}$$

2 With the spectral method of Ex. 2.2, represent the adjoint critical problem for PPF,

$$\sigma^* D\cdot\phi \;=\; L_R^\dagger\cdot\phi\;, \tag{2.41}$$

as a matrix problem.

3.a With the command `Get`, read the file `RckcomcNz..` writen during the resolution of Ex. 2.2, then solve numerically the adjoint problem (2.41) for $k = k_c$, $R = R_c$, and check that there exists an ***adjoint critical mode***

$$\phi_{1c} \;=\; \Phi(z)\;\exp(ik_c x) \tag{2.42}$$

corresponding to $\sigma = -i\omega_c$.

3.b Calculate the function $\Phi(z)$, plot $|\Phi(z)|$ and comment.

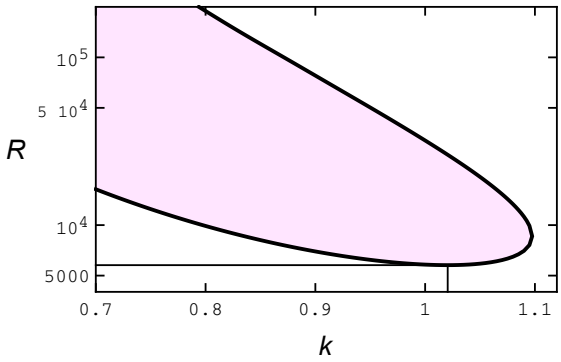

Fig. 2.2 : Region of ***linear instability of PPF to TS waves***, according to the ***temporal stability analysis***, see Ex. 2.3. The straight lines show the critical parameters.

4 Normalize this mode with the condition (1.42),

$$\langle D\cdot\psi_{1c}\ ,\ \phi_{1c}\rangle \ = \ \int_{-1}^{1}[D\cdot\Psi\exp(ik_cx)]\ \Phi^*\exp(-ik_cx)\frac{dz}{2} \ = \ 1\ . \tag{2.43}$$

For this purpose read the file `V1.m` written during the resolution of Ex. 2.2, to reconstruct the critical mode eigenfunction $\Psi(z)$, and evaluate the scalar product with the not-normalized adjoint mode using `NIntegrate`. Save the spectral coefficients of the normalized adjoint streamfunction $\Phi(z)$ to a file `U1.m`.

2.3.2 Simplified form of the weakly nonlinear solution: active and passive modes

We distinguish between ***active*** and ***passive modes***.

- The ***active modes*** correspond to $\mathbf{q}=\mathbf{q}_c=(k_c,1)$ or $\mathbf{q}_c^*=(-k_c,1)$ and have eigenvalues

$$\sigma(\mathbf{q}_c,R) \ = \ -i\omega_c \ + \ (1+is)\epsilon/\tau_0 \ + \ O(\epsilon^2)\ , \tag{2.44a}$$
$$\sigma(\mathbf{q}_c^*,R) \ = \ +i\omega_c \ + \ (1-is)\epsilon/\tau_0 \ + \ O(\epsilon^2)\ , \tag{2.44b}$$

  with $\tau_0>0$ the characteristic time of the instability, s the linear frequency-shift coefficient.

- The ***passive modes*** correspond to $\mathbf{q}\neq\mathbf{q}_c,\mathbf{q}_c^*$ and are short-living (rapidly damped),

$$\sigma(\mathbf{q},R) \ = \ \sigma_r(\mathbf{q},R) \ + \ i\sigma_i(\mathbf{q},R) \quad \text{with} \quad \sigma_r(\mathbf{q},R) \ < \ \sigma_1 \ < \ 0\ . \tag{2.45}$$

The weakly nonlinear solution is seeked as

$$\boxed{\psi \ = \ \psi_a \ + \ \psi_\perp} \tag{2.46}$$

with the ***active modes*** leading term

$$\boxed{\psi_a \ = \ A(t)\ \exp(-i\omega_c t)\ \psi_{1c} \ + \ c.c. \ \ll \ 1}\ , \tag{2.47}$$

and $\psi_\perp \ \ll \ \psi_a$ ***passive modes*** terms. It is quite important to insert the oscillating factor $\exp(-i\omega_c t)$. Indeed, if one inserts this ansatz in the linearized problem, one obtains

$$\begin{aligned}\left(\frac{dA}{dt}-i\omega_cA\right)\ \exp(-i\omega_ct)\ D\cdot\psi_{1c} \ + \ c.c. \ &= \ A\ \exp(-i\omega_ct)\ L_R\cdot\psi_{1c} \ + \ c.c.\\ &= \ \sigma(\mathbf{q}_c,R)\ A\ \exp(-i\omega_ct)\ D\cdot\psi_{1c} \ + \ c.c.\end{aligned} \tag{2.48}$$

By projection onto the adjoint critical mode ϕ_{1c} , one gets

$$\frac{dA}{dt} - i\omega_c A \;=\; \sigma(\mathbf{q}_c,R)\; A \quad\Longleftrightarrow\quad \frac{dA}{dt} \;=\; [\sigma(\mathbf{q}_c,R) + i\omega_c]\; A \;\sim\; (1+is)\frac{\epsilon}{\tau_0}\; A \tag{2.49}$$

according to the expansion (2.44). This shows that A is a ***slowly varying*** amplitude[5].

At leading order, the ***passive modes*** are created by the nonlinear terms

$$N_2(\psi_a,\psi_a) \;=\; |A(t)|^2\; [N_2(\psi_{1c},\psi_{1c}^*) \;+\; c.c.] \;+\; [A^2(t)\; \exp(-2i\omega_c t)\; N_2(\psi_{1c},\psi_{1c}) \;+\; c.c.]\;. \tag{2.50}$$

The analysis is simplified in that we disregard, in a first approach, the harmonic modes in $\exp[\pm 2i(k_c x - \omega_c t)]$, that we 'neglect'. This is a very crude approximation, you might try to avoid it by computing these harmonic modes and their feedback on the critical mode...
Thus, we will assume that $\psi_\perp$ contains only an x-homogeneous contribution,

$$\psi_\perp \;\simeq\; A_0(t)\; \psi_{20}\;. \tag{2.51}$$

By identification of the x-homogeneous, passive part of the equations, one gets

$$\frac{dA_0}{dt}\; D\cdot\psi_{20} \;=\; A_0\; L_R\cdot\psi_{20} \;+\; |A(t)|^2\; [N_2(\psi_{1c},\psi_{1c}^*) \;+\; c.c.]\;. \tag{2.52}$$

We solve this equation by ***quasistatic elimination***, assuming

$$A_0 \;=\; |A|^2\;, \quad \text{therefore} \quad \frac{dA_0}{dt} \;\ll\; A_0 \quad \text{and} \quad 0 \;=\; L_R\cdot\psi_{20} \;+\; [N_2(\psi_{1c},\psi_{1c}^*) \;+\; c.c.]\;. \tag{2.53}$$

Thus

$$\boxed{\psi_\perp \;\simeq\; |A|^2\; \psi_{20}}\;. \tag{2.54}$$

Note the similarity with eq. (1.57) and (1.60).
However, all the information concerning pressure has been lost when we considered the vorticity eq. (2.9) instead of the Navier-Stokes eq. (2.6). This is not dangerous as far as modulated modes like the critical mode are concerned: to them corresponds a modulation of pressure, which is not very important. On the contrary, when we want to calculate an x-homogeneous mode like ψ_{20}, we must care with the pressure: modifying the mean pressure gradient for instance would translate in a change of the head losses, which are quite important from an energetical point of view. Therefore, to calculate ψ_{20} with the most natural condition of ***fixed mean pressure gradient - fixed head losses***, we must come back to the Navier-Stokes eq. (2.6). The streamfunction ψ_{20} thus corresponds to a correction of the basic flow $U(z)\overline{\mathbf{e}}_x$, of the form $U_2(z)\overline{\mathbf{e}}_x$, which is driven by the quasistatic equation

$$R_c^{-1} U_2''(z) \;=\; [(\overline{\mathbf{u}}_1\cdot\overline{\boldsymbol{\nabla}})\overline{\mathbf{u}}_1^* \;+\; c.c.]_x \tag{2.55}$$

with

$$\overline{\mathbf{u}}_1 \;=\; -\,\partial_z[\Psi(z)\; \exp(ik_c x)]\; \overline{\mathbf{e}}_x \;+\; \partial_x[\Psi(z)\; \exp(ik_c x)]\; \overline{\mathbf{e}}_z \tag{2.56}$$

the velocity field of the critical mode (2.37).

[5] In this sense, the active modes are 'long-living'.

Exercise 2.5 ***General form of the nonlinear source terms for the homogeneous mode***

Separating the critical streamfunction into real and imaginary parts according to

$$\Psi(z) \;=\; \Psi_r(z) \;+\; i\Psi_i(z)\;, \tag{2.57}$$

show with formal computations performed with Mathematica that the nonlinear source term in eq. (2.55) can be simplified,

$$[(\overline{\mathbf{u}}_1\cdot\overline{\boldsymbol{\nabla}})\overline{\mathbf{u}}_1^* \;+\; c.c.]_x \;=\; 2k_c[\Psi_r''(z)\Psi_i(z)-\Psi_r(z)\Psi_i''(z)]\;. \tag{2.58}$$

Exercise 2.6 ***Homogeneous passive mode in PPF with a fixed mean pressure gradient***

We remark that eq. (2.55) can be integrated once to obtain

$$R_c^{-1}U_2'(z) \;=\; 2k_c[\Psi_r'(z)\Psi_i(z)-\Psi_r(z)\Psi_i'(z)]\;, \tag{2.59}$$

where the constant of integration vanishes[6]. This eq. (2.59) shows that $U_2'(z)$ vanishes if $z=\pm1$. Therefore, $U_2(z)$ satisfies the same boundary conditions as $\Psi(z)$, i.e.

$$U_2 \;=\; U_2' \;=\; 0 \quad \text{if} \quad z=\pm1\;. \tag{2.60}$$

We observe finally that eq. (2.55) can be rewritten

$$-\,D\cdot U_2 \;=\; \Delta U_2(z) \;=\; U_2''(z) \;=\; 2R_ck_c[\Psi_r''(z)\Psi_i(z)-\Psi_r(z)\Psi_i''(z)]\;. \tag{2.61}$$

The operator D already encountered in the linear analysis (see eq. 2.21) is implied, and acts on the x-homogeneous field U_2 which satisfies the same boundary conditions (2.60) as the field Ψ of the linear problem (see eq. 2.23). Therefore, the spectral code constructed in Ex. 2.2 can be re-used to solve eq. (2.61).

1 In a new Notebook, extract a part of the code of Ex. 2.2 to compute the matrix MD that represents D for $k=0$, with the spectral method.

2 With the command `Get`, read the files `RckcomcNz..` and `V1.m` written during the resolution of Ex. 2.2, to define the critical parameters R_c and k_c, and the critical streamfunction $\Psi(z)$. Separate it into real and imaginary parts, and evaluate the source term, the r.h.s. of eq. (2.61), at the collocation points (2.25), to compute a source vector S_0 such that

$$-\,MD\cdot V_0 \;=\; S_0\;, \tag{2.62}$$

with V_0 the vector of the spectral coefficients of $U_2(z)$.

3 Solve the problem (2.62) with the command `LinearSolve`, to compute V_0, then $U_2(z)$.
Plot $U_2(z)$ and explain the physics behind.

4 Save the vector of the spectral coefficients of $U_2(z)$ to a file `U2.m`.

Additional information

An analysis of the source terms in the equation (2.61), which can be integrated with respect to z, is presented in Plaut *et al.* (2008). This analysis advocates and precises the ***'Reynolds-Orr amplification mechanism'***, which may be viewed as the driver of the TS waves.

[6] One can show this by integrating the eq. (2.59) once more, writing the boundary conditions $U_2(\pm1)=0$, and using the fact that $\Psi(z)$ is even under $z\mapsto -z$.

2.3.3 Feedback at order A^3

In the nonlinear regime, one has of course to add, in the r.h.s. of the linearized eq. (2.48), the terms

$$N_2(\psi,\psi) \;=\; N_2(\psi_a,\psi_a) \;+\; N_2(\psi_a,\psi_\perp) \;+\; N_2(\psi_\perp,\psi_a) \;+\; h.o.t. \tag{2.63}$$

To obtain the amplitude equation for $A(t)$, we have to project these terms onto the adjoint critical mode ϕ_{1c}, and collect the resonant terms N, such that

$$\langle N,\, \phi_{1c}\rangle \;\neq\; 0\;.$$

From the eq. (2.47) and (2.54), we know that

$$\psi_a \;=\; A(t)\;\exp(-i\omega_c t)\;\psi_{1c} \;+\; c.c. \quad \text{and} \quad \psi_\perp \;\simeq\; |A(t)|^2\;\psi_{20}\;, \tag{2.64}$$

with $\psi_{1c} \propto \exp(ik_c x)$ and ψ_{20} independent of x. Therefore, at leading order,

$$\langle N_2(\psi,\psi),\, \phi_{1c}\rangle \;=\; g\;|A(t)|^2 A(t) \tag{2.65}$$

with the ***feedback coefficient***

$$g \;=\; \langle N_2(\psi_{1c},\psi_{20}) + N_2(\psi_{20},\psi_{1c}),\, \phi_{1c}\rangle\;. \tag{2.66}$$

This general theoretical expression will become more concrete if one rewrites the nonlinear term in the vorticity equation (2.10) as

$$\widetilde{N}_2(\overline{\mathbf{u}}_a,\, \overline{\mathbf{u}}_b) \;=\; \partial_x\big(\overline{\mathbf{u}}_a\cdot\overline{\boldsymbol{\nabla}}u_{zb}\big) - \partial_z\big(\overline{\mathbf{u}}_a\cdot\overline{\boldsymbol{\nabla}}u_{xb}\big)\;. \tag{2.67}$$

Then the nonlinear resonant term

$$S_2(x,z) \;=\; \widetilde{N}_2(\overline{\mathbf{u}}_1,\, U_2\overline{\mathbf{e}}_x) \;+\; \widetilde{N}_2(U_2\overline{\mathbf{e}}_x,\, \overline{\mathbf{u}}_1)\;, \tag{2.68}$$

with $\overline{\mathbf{u}}_1$ given by eq. (2.56), and the feedback coefficient

$$g \;=\; \langle S_2(x,z),\, \phi_{1c}(x,z)\rangle \;=\; \int_{z=-1}^{1} S_2(0,z)\;\Phi^*(z)\;\frac{dz}{2}\;. \tag{2.69}$$

Exercise 2.7 ***Feedback coefficient in PPF with a fixed mean pressure gradient***

For PPF, code the computation of the feedback coefficient (2.69) with Mathematica.

1 In a new Notebook, for two velocity fields $\overline{\mathbf{u}}_a = u_{xa}\overline{\mathbf{e}}_x + u_{za}\overline{\mathbf{e}}_z$ and $\overline{\mathbf{u}}_b = u_{xb}\overline{\mathbf{e}}_x + u_{zb}\overline{\mathbf{e}}_z$, write a function `N2[uxa,uza,uxb,uzb]` that codes $\widetilde{N}_2(\overline{\mathbf{u}}_a,\, \overline{\mathbf{u}}_b)$ defined by eq. (2.67).

2 Read the file `RckcomcNz..` to define the critical parameters R_c and k_c ; the files `V1.m`, `U1.m`, `U2.m` to reconstruct the functions $\Psi(z)$, $\Phi(z)$ and $U_2(z)$.
Write a function `S2[x,z]` that codes $S_2(x,z)$ defined by eq. (2.68).

3 Compute with `NIntegrate` the feedback coefficient g defined by eq. (2.69).
Check that, when separated into real and imaginary parts,

$$g \;=\; g_r \;+\; i g_i \quad \text{with} \quad g_r \;>\; 0\;, \tag{2.70}$$

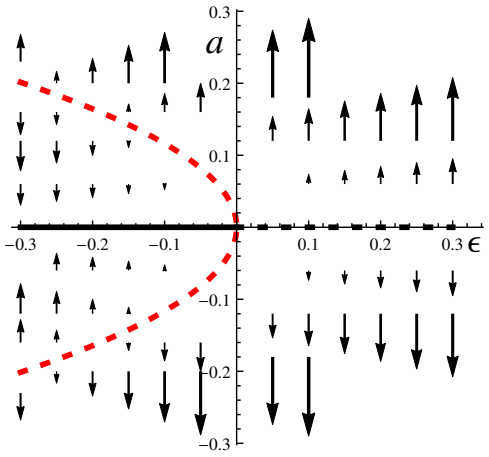

Fig. 2.3 : ***Bifurcation diagram*** of the amplitude equation (2.74), with the same convention as in Fig. 1.2, to which it should be compared. The arrows now show vectors $(0,\ da/dt)$ when $a(t)$ evolves according to eq. (2.74), from an initial condition which is not a fixed point.

and give a numerical estimate of g_r with 2 digits,

$$g_r \ = \ 39 \ . \tag{2.71}$$

In conclusion, gathering the linear and lowest order nonlinear terms in the evolution equation

$$D \cdot \partial_t \psi \ = \ L_R \cdot \psi \ + \ N_2(\psi,\psi)$$

projected onto ϕ_{1c}, we obtain, according to (2.48) and (2.65), the ***complex amplitude equation***

$$\boxed{\frac{dA}{dt} \ = \ (1+is)\frac{\epsilon}{\tau_0}\ A \ + \ (g_r + ig_i)|A|^2 A} \ . \tag{2.72}$$

It is useful to use a polar representation of the amplitude,

$$A \ = \ |A| \ \exp(i\phi) \ . \tag{2.73}$$

The modulus $a = |A|$ then satisfies the real ***amplitude equation***

$$\boxed{\frac{da}{dt} \ = \ \frac{\epsilon}{\tau_0}\ a \ + \ g_3 a^3} \quad \text{with} \quad g_3 \ = \ g_r \ > \ 0 \ . \tag{2.74}$$

This is the generic amplitude equation of a ***subcritical pitchfork bifurcation***. The ***anti-saturation*** effect traduced by the fact that $g_3 > 0$ has the consequence that nonlinear terms enhance the instability for $\epsilon > 0$. Therefore, no stationary solutions or 'fixed points' exist for $\epsilon > 0$. They exist on the contrary for $\epsilon < 0$, i.e., below ('sub') the onset of the bifurcation, and are given by

$$a \ = \ \pm \sqrt{-\epsilon/(\tau_0 g_3)} \ . \tag{2.75}$$

However, they are unstable vs perturbations of the amplitude, as shows the corresponding bifurcation diagram Fig. 2.3. Within this model, for $\epsilon > 0$ the amplitude $a(t)$ goes to infinity, if one starts with an initial condition $a(0) \neq 0$: one faces a very strong instability of the basic flow.

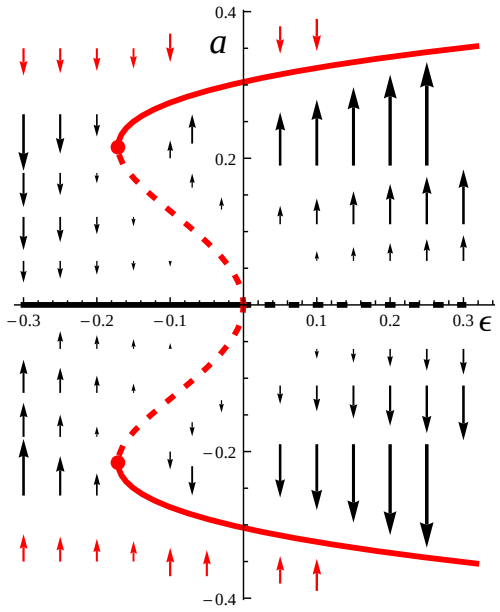

Fig. 2.4 : ***Bifurcation diagram*** of the amplitude equation (2.76), with the same convention as in Fig. 2.3, to which it should be compared. The gray (red online) disks show the turning points where saddle-node bifurcations occur. The black arrows now show vectors $(0,\, da/dt)$ when $a(t)$ evolves according to eq. (2.76), from an initial condition which is not a fixed point. Far from the origin, da/dt becomes large, hence the gray (red online) arrows have a length divided by a factor 10, as compared with the black arrows.

However, to have $|a(t)| \longrightarrow +\infty$ in many cases is not quite physical. A more relevant model can be obtained, phenomenologically, by adding a saturation term at order A^5 or a^5 to the r.h.s. of eq. (2.74), thus respecting the symmetry properties of the system. The new ***amplitude equation*** thus obtained,

$$\boxed{\frac{da}{dt} \;=\; \frac{\epsilon}{\tau_0}\, a \;+\; g_3 a^3 \;-\; g_5 a^5} \qquad \text{with} \qquad g_3, g_5 \;>\; 0\;, \tag{2.76}$$

corresponds to the bifurcation diagram of Fig. 2.4. The characteristic time τ_0 can be easily scaled out by a change of the unit of time, i.e., one can assume $\tau_0 = 1$. The bifurcated stationary solutions of (2.76) with $\tau_0 = 1$ are easily parametrized by a as

$$\epsilon \;=\; \epsilon(a) \;=\; -\, g_3 a^2 \;+\; g_5 a^4\;. \tag{2.77}$$

For small ϵ and a, the two branches of solutions parametrized by this polynomial approach asymptotically the branches of the lower-order amplitude equation (2.74), which are given by eq. (2.75) and displayed in Fig. 2.3. However, at ***'turning points'*** defined by

$$a_{\rm tp} \;=\; \pm\sqrt{g_3/(2g_5)} \qquad \text{and} \qquad \epsilon_{\rm tp} \;=\; -\, g_3^2/(2g_5)\;, \tag{2.78}$$

the branches turn to the right of the bifurcation diagram Fig. 2.4. Exactly as one passes the turning points, the solutions become stable, within the framework of eq. (2.76). Since in the real physical systems there are many degrees of freedom, one typically passes from a 'saddle' fixed point, for $|a| < a_{\rm tp}$, i.e., a solution that has many stable modes and at least one unstable mode, to a 'node' fixed point, for $|a| > a_{\rm tp}$, i.e., a solution that has one more stable mode, and, in some cases, is completely stable. This phenomenon is therefore called a ***'saddle-node bifurcation'***.
A comparison between the Fig. 1.2 and 2.4 shows that the instability of the basic flow (or state),

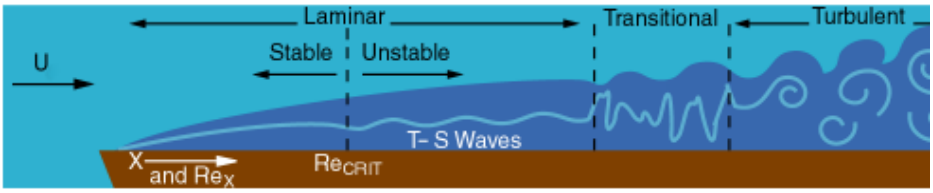

Fig. 2.5 : (color online) Sketch of the ***transition to turbulence in a Boundary Layer*** from the DVD *Multimedia Fluid Mechanics* by Homsy *et al.* CUP 2004.

when $\epsilon > 0$, is 'stronger' than in the supercritical case, since one typically goes, even for quite small values of ϵ, to a finite value of a.
It must also be remarked that, in the interval $\epsilon_{\rm tp} < \epsilon < 0$, there exist three stable solutions of the dynamical system described by the eq. (2.76) : the trivial solution $a = 0$ (corresponding to the basic flow) and two bifurcated solutions defined by (2.77). Therefore this model displays ***bistability***. ***Hysteretic*** behaviours can consequently happen: if one starts with a weakly perturbed basic flow, and increases R i.e. ϵ, the transition to TS-waves will occur only at $\epsilon \simeq 0$ i.e. $R \simeq R_c$. If one then decreases R and ϵ, the TS-waves will probably survive down to the turning point where they disappear.

2.4 About spatial and spatio-temporal stability theories

In the ***temporal linear stability theory***, we have considered modes of the linearized problem of the form

$$\exp[i(kx - \omega t)] \quad \text{with} \quad k \in \mathbb{R} \text{ the wavenumber}, \quad \omega = \omega(k) \in \mathbb{C} \text{ the temporal eigenvalue.}$$

However, since there exists in general a non-vanishing mean flow, a ***spatial linear stability theory*** can be relevant. Within this approach, one seeks to calculate modes of the linearized problem of the form

$$\exp[i(kx - \omega t)] \quad \text{with} \quad \omega \in \mathbb{R} \text{ the angular frequency}, \quad k = k(\omega) \in \mathbb{C} \text{ the spatial eigenvalue.}$$

Usually, in unstable flows, modes with $k_i < 0$ exist, which are amplified as x increases... An example of spatial stability analysis is given in the Pb. 2.1; see also the corresponding Fig. 2.8.
In fact, a ***spatio-temporal theory*** may also be developped, where the spatio-temporal response to a perturbation localized in time and space is calculated. The interested reader should for instance immerse himself in Schmid & Henningson (2001).

2.5 Short review of transition in OSF

Reviews on the nonlinear behaviour of OSF can be found in Huerre & Rossi (1998); Drazin (2002). Numerical computations confirm the subcritical character of the transition to ***Tollmien-Schlichting waves***. However, typically, these waves are unstable vs three-dimensional perturbations. Therefore, a rapid ***transition to turbulence*** often happens in OSF. If the upstream flow (or 'inflow') has a high level of perturbations, ***bypass transition*** can occur, where the flow goes even more rapidly, and 'directly', to turbulence, without the apparition of 2D TS waves.

Also, as already mentioned in section 2.4, the transition to turbulence is generally a ***spatio-temporal problem***. This is obvious in non-parallel flows, like ***Boundary Layers***, where the local Reynolds number increases with the streamwise coordinate x. There the turbulence sets in at a 'particular' distance from the leading edge, as sketched in the Fig. 2.5. This 'particular' distance depends on the level and on the nature of the perturbations that are contained in the inflow. This is illustrated in the ***'numerical experiments'*** of Schlatter *et al.* (2010) shown in Fig. 2.6 and 2.7. In these numerical simulations, which use the 'large-eddy simulation technique', a 2D 'harmonic' forcing is applied close to the edge of the system, the leftmost segment of Fig. 2.6*a,b*. This 'harmonic' forcing is a bulk force applied in the wall-normal direction z, localized in the xz plane but independent of the spanwise coordinate y. It is 'harmonic' because it oscillates sinusoidally in time with an angular frequency ω that is close to the critical frequency ω_c of the TS waves. The localization of this harmonic forcing coincides with the green vortex, the leftmost green segment of Fig. 2.6*a,b*. This harmonic forcing produces ***TS waves*** that first decay with x, but then are amplified due to the natural instability of the Blasius Boundary Layer, as seen by the green vortices which are regularly spaced in the x-direction, and of a growing intensity in the second right half of the flow region in the Fig. 2.6*a,b*. The ***three-dimensional instabilities*** of the TS waves and the ensuing ***transition to turbulence*** is clearly visible on the right of these figures. To trigger these three-dimensional instabilities, some 'noise' has been added with a bulk force localized in the same region where the harmonic forcing is acting, this bulk force now depending on the spanwise coordinate y in a random manner. When this force is constant in time, one obtains the scenario of Fig. 2.6*a*, whereas, when this force depends on time in a random manner, one obtains the scenario of Fig. 2.6*b*, with an 'earlier' transition to turbulence, in terms of x. A 3D visualization of a case similar to the one of Fig. 2.6*a* is shown in Fig. 2.6*c*. One sees first, from left-bottom to right-up, the pattern of TS waves, then a pattern of 3D 'Λ-vortices', then smaller vortices that become more and more turbulent; in addition, low speed blue 'streamwise streaks' are also visible. They indicate a reduction of the average flow velocity. Depending on the global conditions, one may also observe an ***increase of the drag*** exerted by the fluid on the plate...
If one adds in the inflow, or near the edge of the system, a completely 3D noise that is sufficiently strong, to simulate 'natural free-stream turbulence', even if the harmonic forcing is still present, a quite different scenario is observed, as displayed in the Fig. 2.7. In this ***bypass transition scenario***, no TS waves appear, but blue and red streamwise 'streaks' come in and break rather soon, in terms of x, into turbulence...

It is with these figures that we conclude this chapter and this first Part of the module on the ***transition to turbulence***. The second Part of this module, that contains only Chapter 3, will focus on ***fully developped turbulence***... with applications to ***Wind Energy***...

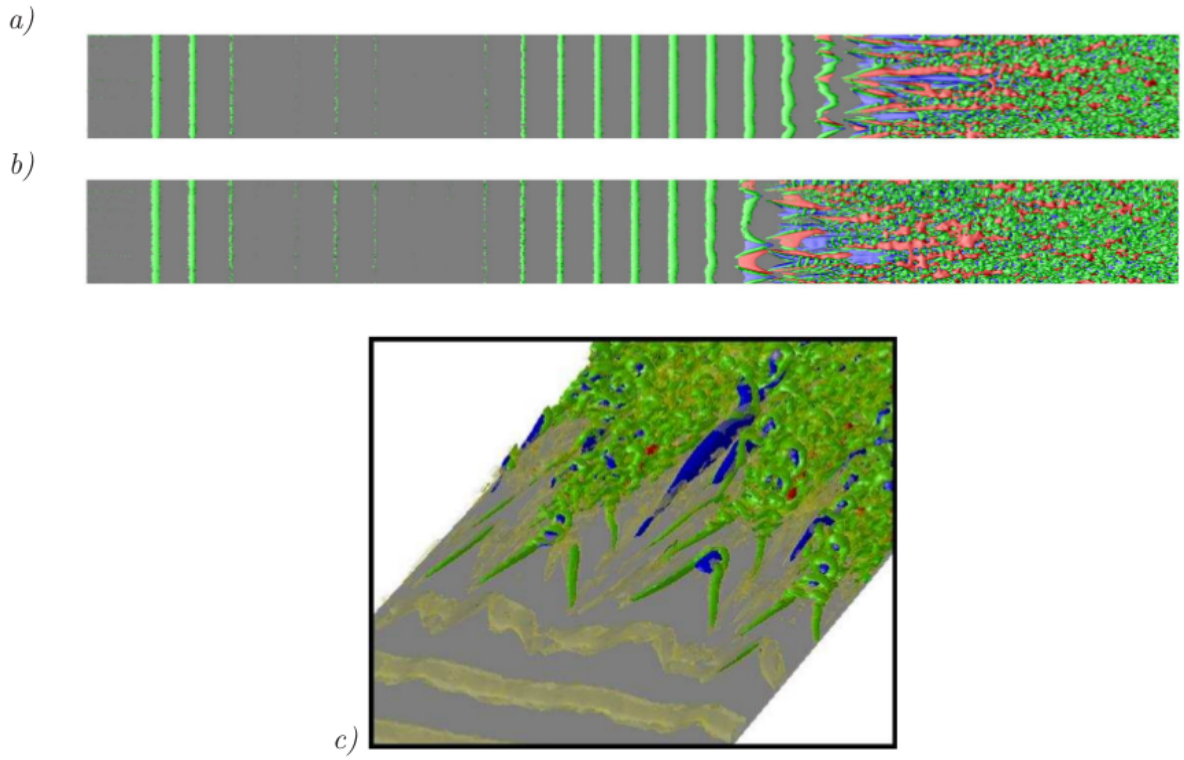

Fig. 2.6 : (color online) Flow visualizations in simulations of a ***Blasius Boundary Layer*** in the presence of forcing (Schlatter *et al.* 2010). (a) and (b) : top view, the flow is from left to right. Green isocontours show high vorticity regions. Red and blue isocontours show regions of positive and negative streamwise disturbance velocity $u_x = \pm 0.07 U_0$ with U_0 the far-field streamwise velocity. (c) : 3D view. The transparent yellow iscontours show 'high vorticity regions' of an intensity which corresponds to the green isocontours of (a) and (b), the green isocontours show regions of even higher vorticity. Red and blue isocontours show $u_x = \pm 0.1 U_0$. Observe a ***progressive transition to turbulence*** with **2D *TS waves*** then **3D Λ-*vortices***.

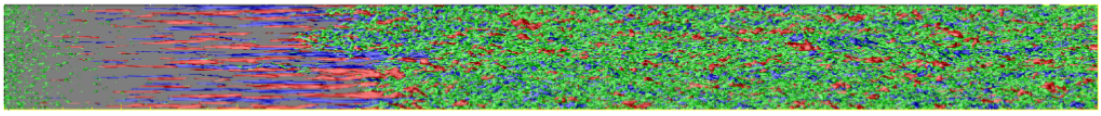

Fig. 2.7 : (color online) Flow visualization as Fig. 2.6*a*, in a similar case where, however, a 'strong' 3D noise has been added in the inflow (Schlatter *et al.* 2010). Observe a ***bypass*** or ***'direct' transition to turbulence***.

2.6 Problem

Problem 2.1 ***Spatial linear stability analysis - The case of Plane Poiseuille Flow***

[*Test of February* 2017]

We consider a ***Viscous Parallel Open Shear Flow*** with a velocity field

$$\overline{\mathbf{v}} \;=\; \overline{\mathbf{v}}_0 \;=\; U(z)\;\overline{\mathbf{e}}_x$$

and investigate its ***stability*** versus ***2D xz perturbations***. With the use of the dimensionless units described in the Lecture Notes, the wall-normal coordinate z varies in the interval $[-1,+1]$. Our aim is to perform a ***spatial stability analysis***, i.e. to compute modes of the form (2.79) with $\omega \in \mathbb{R}^*$, $k \in \mathbb{C}^*$.

1 Give the linearized ordinary differential equation (ODE) that determines the modes of this problem, written under the form

$$\overline{\mathbf{u}} \;=\; \overline{\mathbf{v}} \;-\; \overline{\mathbf{v}}_0 \;=\; \overline{\mathbf{curl}}(\psi\;\overline{\mathbf{e}}_y) \quad \text{with} \quad \psi \;=\; \Psi(z)\;\exp[i(kx-\omega t)]\;. \tag{2.79}$$

Recall the physical origin of this equation, that you will write as an equation applied to $\Psi(z)$. You should introduce the operator

$$D \;=\; \partial_z$$

and the notation $r = R^{-1}$ with R the Reynolds number. You should normalize your equation such that only positive powers of k appear. What is the highest power of k that intervenes ?

2 In order to decrease this power, implement the change of unknown function

$$\Psi(z) \;=\; \Phi(z)\;e^{-kz} \quad\Longleftrightarrow\quad \Phi(z) \;=\; \Psi(z)\;e^{kz}\;.$$

First, calculate $D\Psi$, $D^2\Psi$, $(D^2-k^2)\Psi$ and $(D^2-k^2)^2\Psi$ in terms of Φ and its derivatives[7]. Second, show that $\Phi(z)$ verifies an ODE where k appears only up to the second power.

3 In order to obtain an ***eigenvalue problem*** on k, we introduce the vector

$$v \;=\; \begin{bmatrix} v_1 \\ v_2 \end{bmatrix} \;=\; \begin{bmatrix} k\Phi(z) \\ \Phi(z) \end{bmatrix}\;. \tag{2.80}$$

Show that the ODE on $\Phi(z)$ established Q.2 can be written under the form

$$L_1\cdot v_1 \;+\; L_2\cdot v_2 \;=\; kD_1\cdot v_1 \tag{2.81}$$

where you will identify the differential operators L_1 of order 3, L_2 of order 4, D_1 of order 2, which may depend on ω, r and U but not on k.

Indication: you should show that one may assume $L_2 = -rD^4 - i\omega D^2$.

4 Check that the relation of proportionality of the two components of v and the ODE on $\Phi(z)$ can be written under the matrix form

$$\begin{bmatrix} L_1 & L_2 \\ 1 & 0 \end{bmatrix}\cdot v \;=\; k\begin{bmatrix} D_1 & 0 \\ 0 & 1 \end{bmatrix}\cdot v\;. \tag{2.82}$$

[7] In order to simplify, we denote $D\Psi$ what we could also denote $D\cdot\Psi$.

From now on, the basic flow is the ***Plane Poiseuille Flow*** $U(z) = 1 - z^2$. Also, there are walls at $z = \pm 1$.

5 Recall the boundary conditions that ψ and Ψ must satisfy. Establish the boundary conditions that Φ must satisfy.

6 In order to solve with a ***spectral method*** the system (2.82), justify that it is reasonable to search $\Phi(z)$ as an expansion of the form

$$\Phi(z) \;=\; \sum_{n=1}^{N_z} \Phi_n F_n(z) \quad \text{with} \quad F_n(z) \;=\; (z^2-1)^2\; T_{n-1}(z)\;, \tag{2.83}$$

T_n the n^{th} Chebyshev polynomial of the first kind.

7.1 With the notations of equation (2.80), we assume

$$v_1 \;=\; \sum_{n=1}^{N_z} a_n F_n(z)\;, \quad v_2 \;=\; \sum_{n=1}^{N_z} \Phi_n F_n(z)\;,$$

and introduce the vector of the spectral coefficients

$$V \;=\; \begin{bmatrix} V_1 \\ V_2 \end{bmatrix} \;=\; \begin{bmatrix} a_1 \\ : \\ a_{N_z} \\ \Phi_1 \\ : \\ \Phi_{N_z} \end{bmatrix} \;\in\; \mathbb{C}^{2N_z}\;.$$

We also introduce, to discretize the equation (2.81), the collocation points

$$z_m \;=\; \cos[m\pi/(N_z+1)] \quad \text{for} \quad m \in \{1,2,\cdots,N_z\}\;.$$

For $N_z = 9$, with the help of a geometrical construction that uses the unit circle, represent these points in the interval $[-1,1]$, and comment.

7.2 Show that the system (2.82) can be represented by the matrix system

$$ML \cdot V \;=\; k\; MD \cdot V \tag{2.84}$$

with

$$ML \;=\; \begin{bmatrix} ML1 & ML2 \\ Id & 0 \end{bmatrix}\;, \quad MD \;=\; \begin{bmatrix} MD1 & 0 \\ 0 & Id \end{bmatrix}\;,$$

Id being the identity matrix of dimension $N_z \times N_z$, $ML1$, $ML2$ and $MD1$ being square matrices that represent the operators L_1, L_2 and D_1 defined in Q.3. You will establish the expressions of the matrix elements at line m and column n of $ML1$, $ML2$ and $MD1$.

8 Using a Mathematica code of a structure similar to the one that you used in order to solve Ex. 2.2, construct the matrices ML and MD for a given value of N_z, `Nz` in your code[8]. Hereafter is its skeleton:

```
(*Nb of base functions*) Nz= 36;
(*Base functions*) F[n_,z_]= ...
(*Collocation points*) z[m_]= Cos[m Pi/(Nz+1.)]

(*Inverse of the Reynolds number*) r= 1/R;
(*Base flow*) U[z_]= 1-z^2;
(*Operators*) Dz[f_]:= D[f,z]; Dz2[f_]:= ... ; Dz3[f_]:= ... ; Dz4[f_]:= ... ;
L1[f_]:= 4 r Dz3[f] + ...
L2[f_]:= -r Dz4[f] - ...
D1[f_]:= ...

(*Kronecker delta*) delta[i_,j_]:= If[i==j, 1, 0]

(*Matrices*) MatD = MatL = IdentityMatrix[2 Nz];
Do[
   Do[
      MatD[[m,n]] = ReplaceAll[ ... , z->z[m]];
      MatL[[m,n]] = ReplaceAll[ ... , z->z[m]];
      MatL[[m,Nz+n]] = ReplaceAll[ ... , z->z[m]];
      MatL[[Nz+m,n]] = ... ;
      MatL[[Nz+m,Nz+n]] = ...
     ,{m,1,Nz}]
  ,{n,1,Nz}]

MD[R_]= MatD; ML[omega_,R_]= MatL;

kspectrum[omega_,R_]:= Eigenvalues[{ML[omega,R], MD[R]}]
```

Check that, when $\omega = \omega_{ct} = 0.269$, $R = R_{ct} = 5772$ computed with the temporal stability analysis, you recover in the k-spectrum a wavenumber k close to $k_{ct} = 1.02$, the critical wavenumber found with the temporal stability analysis. For this purpose, use the command

```
kclose[omega_,R_]:= Select[ kspectrum[omega,R], Abs[# - kct] < 0.2 &][[1]]
```

9 Check that, when R varies from $0.9R_{ct}$ to $1.1R_{ct}$, this mode becomes amplified in space. For this purpose calculate theoretically, compute and then plot Fig. 2.8a the ***spatial growth rate*** sr of this mode (define a function `sr[omega,R]` that depends on `kclose[omega,R]`) vs R.

10 Code with `FindRoot` the computation of the ***neutral Reynolds number*** $R_1(\omega)$ at which $sr(\omega,R)$ vanishes. Construct a list `lomR1` of the couples $(\omega,R_1(\omega))$ for discrete ω values spanning the interval

$$0.24 \ \leq \ \omega \ \leq \ 0.286 \ ,$$

and plot Fig. 2.8b the corresponding ***spatial neutral curve***.

[8] You may test your code at the beginning with 'small' values of N_z, but the preferred value that you must use is $N_z = 36$.

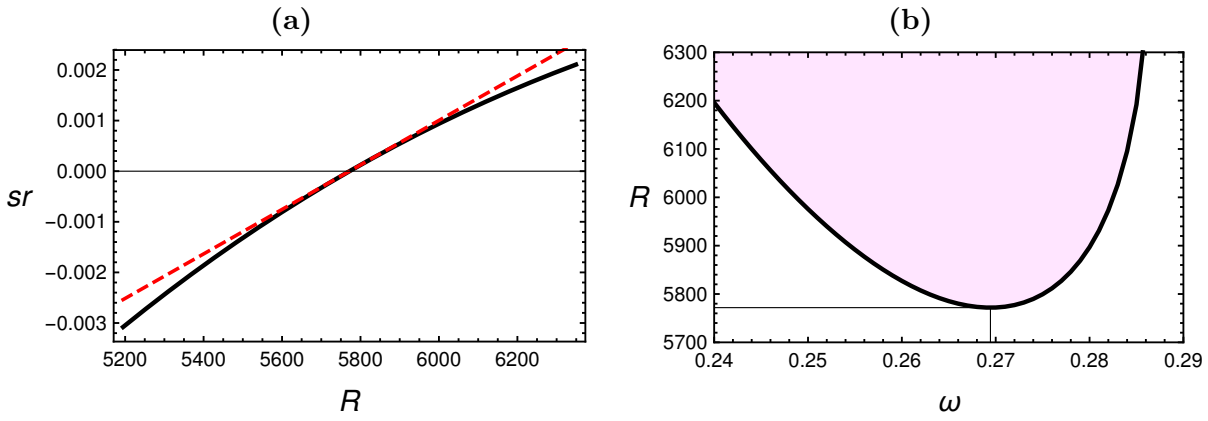

Fig. 2.8 : According to the ***spatial stability analysis*** performed in Pb. 2.1 **a:** the continuous curve shows the ***spatial growth rate*** of the most relevant spatial mode with the critical angular frequency, the dashed line the lowest order estimate ϵ/ℓ_0 ; **b:** region of ***linear instability of PPF to TS waves***; the straight lines show the critical parameters.

11 Code with `FindMinimum` the computation of the ***bifurcation point*** where the first spatially amplified mode appears, for the lowest value of R. Compare the ***critical parameters*** (ω_c,k_c,R_c) obtained with the ones determined with the temporal stability analysis. Comment.

12 Compute with 3 digits the ***characteristic length*** ℓ_0 such that close to onset, for $\epsilon = R/R_c - 1$ small,

$$sr(\omega_c,R_c) \;=\; \epsilon/\ell_0 \;+\; o(\epsilon)\;. \tag{2.85}$$

Check the relevance of this computation by overlaying a straight line onto Fig. 2.8a. Comment.

Chapter 3

Wind Energy and Turbulence

This chapter corresponds to the Sessions 3, 4, 5 of 2016-2017.

3.1 Wind Energy: Power performance theory

This section presents the concept of power performance for wind turbines, starting from momentum theory to power curves that leads to the Betz limit. This section deals only with horizontal-axis three-bladed electrical wind turbines. There is no major limitation to its extension to other designs of wind power systems.

3.1.1 Momentum theory for wind turbines

A basic understanding of fluid mechanics will be applied to wind turbines, with the so-called 'momentum theory'. This theoretical approach sets ground for the further power curve analysis. The complexity of turbulence is first set aside, so as to understand the fundamental behavior of a wind turbine in a uniform flow at steady-state. More complex atmospheric effects will be addressed later on.

As a wind turbine converts the power from wind into available electrical power, one can assume the following relation

$$\boxed{P(u) \;=\; c_p(u)\; P_{wind}(u)}\,, \tag{3.1}$$

where $P_{wind}(u)$ is the power contained in the wind passing with speed u through the wind turbine, and $P(u)$ is the ***electrical power extracted***. The amount of power converted by the wind turbine is given by the ***power coefficient*** $c_p(u)$, which represents the efficiency of the machine. As the input $P_{wind}(u)$ cannot be controlled, improving power performance means increasing the power coefficient $c_p(u)$. The power contained in a laminar incompressible flow of mass m and density ρ moving along the $x-axis$ with constant speed u through a vertical plane of area A is

$$P_{wind}(u) \;=\; \frac{dE_{kin,wind}}{dt} \;=\; \frac{d}{dt}\left(\frac{1}{2}mu^2\right) \;=\; \frac{1}{2}\frac{dm}{dt}u^2 \;=\; \frac{1}{2}\frac{d(\rho V)}{dt}u^2 \;=\; \frac{1}{2}\rho\frac{d(Ax)}{dt}u^2 = \frac{1}{2}\rho A u^3\,, \tag{3.2}$$

as can be also deduced from the 'Euler formula' (see e.g. Plaut 2016).

Let us consider a mass of air moving towards a wind turbine, which can be represented by an 'actuator disc' of diameter D. An actuator disc is an infinitely thin disc through which the air can flow without resistance, as proposed by Froude and Rankine's momentum theory Rankine (1865).

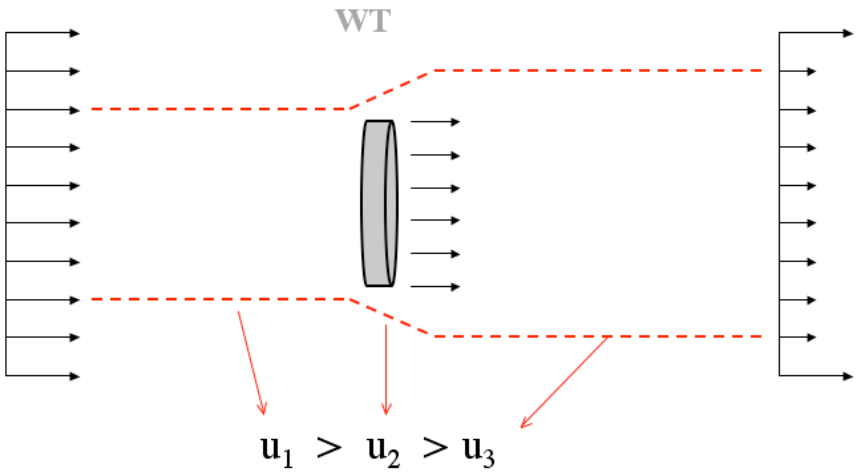

Fig. 3.1 : Idealized flow situation around a wind turbine (WT) according to Twele & Gasch (2005). The dashed lines show the limit of the 'streamtube' considered in the momentum theory, i.e., the stream of air particles that interact with the wind turbine. The wind speeds before, at and after the wind turbine are respectively u_1, u_2 and u_3.

When crossing the wind turbine, the wind is affected as parts of its energy is extracted. This extraction of kinetic energy results in a drop in the wind speed from upstream to downstream. The velocity far before the wind turbine (upstream), at the wind turbine and far behind (downstream) are labelled respectively u_1, u_2 and u_3. An illustration is given in Fig. 3.1. Mass conservation requires that the flow-rate $\dot{m} = A_i \rho u_i$ be conserved and

$$A_1 \rho u_1 \;=\; A_2 \rho u_2 \;=\; A_3 \rho u_3 \,, \tag{3.3}$$

where A_i are the respective areas perpendicular to the flow. A_2 is the area swept by the rotor blades $A_2 = A = \pi D^2/4$. As a consequence of the wind speed slowing down, i.e. $u_3 < u_2 < u_1$, the area of the stream-tube has to expand, and $A_3 > A_2 > A_1$. This can be observed in Fig. 3.1. Also, the energy extracted by the wind turbine can be determined by the difference of kinetic energy upstream and downstream of the wind turbine

$$E_{ex} \;=\; \frac{1}{2} m (u_1^2 - u_3^2) \,, \tag{3.4}$$

resulting in a power extraction

$$P_{ex} \;=\; \frac{d}{dt} E_{ex} \;=\; \frac{1}{2} \dot{m} (u_1^2 - u_3^2) \,. \tag{3.5}$$

The wind turbine continuously takes energy out of the wind flow, which reduces its velocity. However, the flow needs to *escape* the wind turbine downstream with a speed $u_3 > 0$. If all the power content of the wind would be extracted, the wind speed downstream would then become zero. As a consequence, the air would *accumulate* downstream and block newer air from flowing through the wind turbine, so that no more power could be extracted. This means that the wind flow must keep some energy to escape, which naturally sets a limit for the efficiency of any wind power system. The power coefficient $c_p(u)$ must be inferior to 1. An optimal ratio of wind speeds $\mu = u_3/u_1$ can be found that allows for the highest energy extraction.

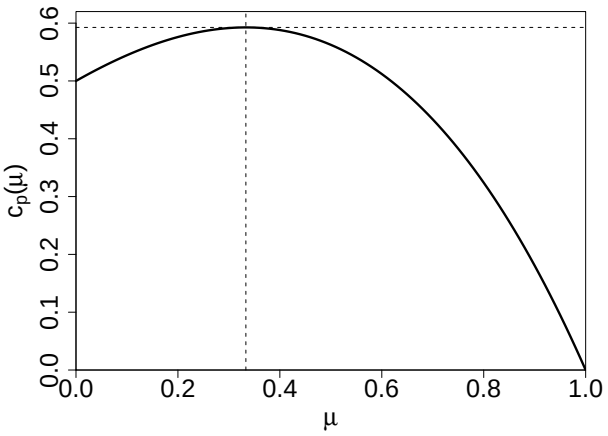

Fig. 3.2 : Power coefficient c_p as a function of the wind speed ratio $\mu = u_3/u_1$.

3.1.2 Power performance - Betz limit

In the plane of the rotor blades, an intermediate value of wind speed

$$u_2 \;=\; \frac{u_1 + u_3}{2} \tag{3.6}$$

can be shown to be optimal, following Froude-Rankine. Knowing this value one also knows the flow-rate in the rotor plane area that is now given by

$$\dot{m} \;=\; \rho A u_2 \,. \tag{3.7}$$

Inserting equations (3.6) and (3.7) into equation (3.5) yields

$$P(\mu) \;=\; \frac{1}{2}\rho A u_1^3 \,\frac{1}{2}(1 + \mu - \mu^2 - \mu^3) \;=\; P_{wind}(u_1)\; c_p(\mu) \tag{3.8}$$

where $\mu = u_3/u_1$ is the wind speed reduction factor. The theoretical definition of the power coefficient is then

$$c_p(\mu) = \frac{1}{2}(1 + \mu - \mu^2 - \mu^3)\,, \tag{3.9}$$

as shown in Fig. 3.2. The optimal power performance is obtained for a ratio μ such that the derivative of $c_p(\mu)$ with respect to μ is zero

$$\frac{d}{d\mu} c_p(\mu) = \left(-\frac{1}{2}\right) \times \left(3\mu^2 + 2\mu - 1\right) = 0\,. \tag{3.10}$$

This leads to

$$\mu_{max} \;=\; \frac{1}{3} \quad\Longleftrightarrow\quad c_p(\mu_{max}) \;=\; \frac{16}{27} \;\simeq\; 0.593\;, \tag{3.11}$$

as shown in Fig. 3.2.

This limit is called the ***Betz limit***, see Betz (1927). In other words, a wind turbine can extract at most 59.3% of the power contained in the wind. This can be obtained when the wind speed downstream is one-third of the wind speed upstream.

A widely used representation of power performance is given by the relation of c_p to the ***tip speed ratio***

$$\lambda = \frac{\omega R}{u_1}, \tag{3.12}$$

where ω and R are the angular frequency and radius of the rotor. λ is the ratio of the rotational speed at the tip of the blades to the upstream wind speed. If the rotational speed increases, more air is 'slowed down' by the turbine, i.e., the wind speed reduction factor μ decreases: λ is directly related to μ. The dimensionless $c_p - \lambda$ curve will be introduced in the next section.

Betz' momentum theory only considers the mechanical transfer of energy from the wind to the rotor blades. The next step of the conversion from mechanical to electrical energy has not been taken into account, as well as all energy losses. The more complex design of wind turbines causes lower values of c_p, as discussed in section 3.1.3. The power coefficients of modern commercial wind turbines reach values of order 0.5. Also, criticism of Betz theory is given in Rauh & Seelert (1984); Rauh (2008), leading to a less well defined upper limit of c_p.

3.1.3 Limitations of Betz theory - Energy losses

Although it is based on a simplified approach, the Betz limit is a widely used and accepted value. But more realistic considerations indicate that real wind turbine designs have even lower efficiency due to additional limitations. In this section, the three main limitations to reach the optimal value of $c_p = 16/27$ are introduced. This section only aims to give a first idea. For a more detailed understanding of the mathematical equations presented here, the reader is kindly referred to the literature.

Bouncing losses

Betz' consideration does not take into account that there is not only a reduction of wind speed downstream, but also an additional angular momentum that is transferred to the air flow, as shown in Fig. 3.3. This effect follows Newton's third law, as a reaction to the rotational motion of the rotor. For slow rotating wind turbines (λ small), these losses are much more severe than for fast rotating machines. For $\lambda \approx 1$ an optimum value of c_p of only 0.42 can be reached instead of the Betz optimum of 0.59. c_p approaches the Betz optimum with increasing tip speed ratio.

Profile losses

Another important source of energy loss is the quality of the airfoil profile for which the realistic or ideal cases, including drag force or not, can be considered.
The efficiency η can now be defined as the ratio between equation realistic and ideal situation. This leads to the efficiency given by

$$\eta = 1 - \xi\,. \tag{3.13}$$

The profile losses ξ_{prof} follow the relation

$$\xi_{prof} \propto r\lambda\,. \tag{3.14}$$

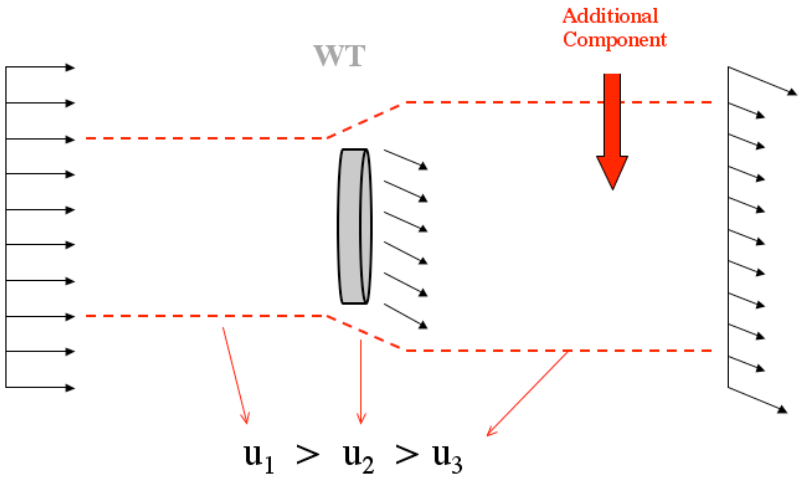

Fig. 3.3 : Flow around a wind turbine. After passing the turbine the velocity field has a rotational component due to the rotating rotor blades.

In contrast to the bouncing losses, the profile losses mainly affect fast rotating machines. For higher tip speed ratios, the lift to drag ratio C_L/C_D must be optimized. Furthermore the losses increase with the radius, such that the manufacturing quality of the blade tips is of primary importance for power performance.

Tip losses

A good quality of the tips especially means that they should be as narrow as possible because this corresponds to an (ideal) airfoil with length infinity, $R/c \to \infty$ with R the distance to the rotation axis and c the chord. For real blades there is always a flow around the end of the blade (forming an eddy that is advected by the flow) from the high pressure area to the low pressure area. This is partly levelling the pressure difference and consequently the lift force. The tip losses obey approximately the following relation

$$\xi_{tip} \propto \frac{1}{z\lambda}. \tag{3.15}$$

Different to the profile losses an increasing tip speed ratio decreases the tip losses, as well as an increased number of blades.

Impact on power performance

The Fig. 3.4 shows an overview of the different kinds of losses and their influence on the value of c_p. One can see that bouncing losses cause the largest reduction in the power coefficient for small values of λ, similar to the finite number of blades. This is the opposite for the profile losses. Three-bladed wind turbines can reach optimal c_p values of order 0.50 for typical values of $\lambda \approx 6-8$, which naturally sets the strategy for optimal power performance in terms of rotational frequency ω.

3.1.4 Power curve

Along with the $c_p - \lambda$ curve, a standard representation of a wind turbine power performance is given by a so-called ***power curve***. The power curve gives the relation between the simultaneous

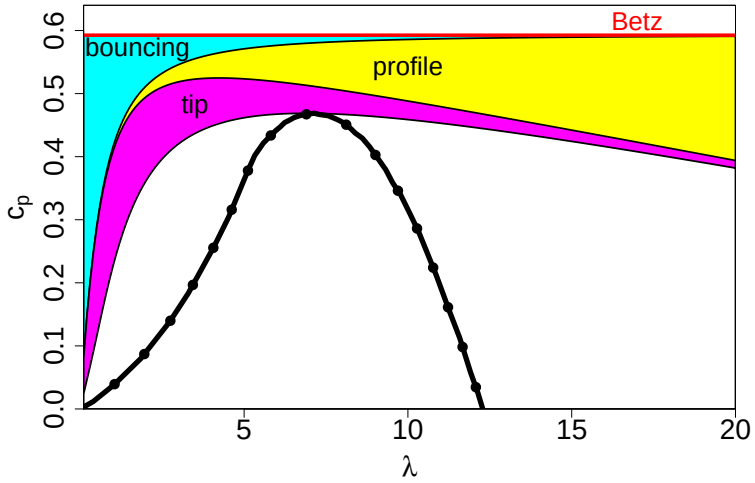

Fig. 3.4 : Typical $c_p - \lambda$ curve (black dotted line). The influence on the efficiency of Betz limit, the bouncing, profile and tip losses is illustrated. These results were obtained with a lift to drag ratio $C_L/C_D = 60$ and $z = 3$ blades. Maximum performance $c_p \simeq 0.475$ is obtained at $\lambda \simeq 7$.

wind speed u and power output P. Following usual practice, the ***wind speed*** u will refer to the upstream horizontal wind speed u_1 from now on, such that $u = u_1$. Also, the ***net electrical power output*** P that the wind turbine actually delivers to the grid is considered, integrating all possible losses. The two quantities u and P will follow these specifications until the end of the chapter. Following equation (3.8), the theoretical power curve reads

$$\boxed{P(u) \;=\; c_p(u)\; P_{wind}(u) \;=\; c_p(u)\; \frac{1}{2}\rho A u^3}\,. \tag{3.16}$$

In most of the modern wind turbine designs, the ***regulation of the power output*** is performed through changes both in the ***rotational frequency of the generator*** and in the ***pitch angle of each blade***. (Note other wind turbine designs involve fixed rotational frequency, so-called fixed-speed wind turbines, or fixed pitch angle, so- called fixed-pitch wind turbines). A more detailed description on control strategies is given in Bianchi *et al.* (2006). The rotational frequency of the generator is physically linked to the wind speed, such that it cannot be changed freely. However, the pitch angle of the blades can be controlled at will, and almost independently of the wind speed, to reach the chosen control strategy, and hence represents the central mean of control for the operation. Pitching plainly consists of a rotation of the blades by a pitch angle θ in the plane of their cross-section.

The power production is then controlled by changing the lift forces on the rotor blades (Burton *et al.* 2001; Bianchi *et al.* 2006). The power production can be reduced or stopped by pitching the blades towards stall[1]. In modern wind turbines, this is achieved by a so-called active pitch control. The power coefficient c_p depends strongly on this pitch angle θ and on the tip speed ratio λ, i.e. $c_p = c_p(\lambda(u),\theta)$. As λ can typically not be controlled, c_p is optimized via θ to a desired power production. In particular for high wind speeds, c_p is lowered to protect the wind turbine machinery and prevent from overshoots in the power production.

This pitch regulation is commanded by the controller of the wind turbine, which constitutes of

[1] Stall effects are obtained when the angle of attack of an airfoil exceeds a critical value, resulting in a sudden reduction in the lift force generated.

several composite mechanical-electrical components that operate actively for the optimum power performance[2]. For the common pitch-controlled wind turbines, the control strategy gives four distinct modes of operation:

- for $u \leq u_{cut-in}$, here u_{cut-in} represents the minimum wind speed such that the wind turbine can extract power, typically in the order of $3-4$ m/s. In this range the power contained in the wind is not sufficient to maintain the wind turbine into motion, and no power is produced;
- in partial load $u_{cut-in} \leq u \leq u_{rated}$, here u_{rated} denoted the rated wind speed at which the wind turbine extracts the rated, maximum allowed power P_{rated}. u_{rated} is typically in the order of $12 - 15$ m/s. In this range the wind turbine works at its maximum power performance, i.e. c_p is maximized, and the pitch angle θ is normally maintained constant;
- in full load $u_{rated} \leq u \leq u_{cut-out}$, here $u_{cut-out}$ represents the maximum wind speed at which the wind turbine can safely extract power, typically in the order of $25 - 35$ m/s. In this range the wind turbine power output is limited to the rated power P_{rated}. In this mode of operation, the pitch angle θ is adjusted in real-time to maintain $P \approx P_{rated}$;
- for $u > u_{cut-out}$ the pitch angle θ is maximized to the feathered position so as to eliminate the lift forces on the blades. A braking device can be used in addition to block the rotation for safety reasons. As a consequence, the power production is stopped.

An illustration of the theoretical strategy for $c_p(u)$ and $P(u)$ is given in Fig. 3.5.

It is important to precise that this theoretical estimation is valid for a ***laminar flow***, which never occurs in real situations. The more complex atmospheric winds call for more complex descriptions of power performance. Following the path of turbulence research, statistical models are introduced in Appendix A to deal with this complexity.

3.2 Rotor blade: Blade Element Momentum theory (BEM)

In this section will will use the momentum theory for sections of the rotor to derive the ***design*** or layout of a rotor blade.

Modern wind turbines rotate due to the lift forces F_L acting on the airfoils. For an airfoil the effective area can be expressed in terms of the ***depth***, also called ***chord***, c, and the ***span*** of the wing b, similar to the rotor radius R. Therefore the ***drag force*** F_D and the ***lift force*** F_L read

$$F_D = C_D(\alpha)\frac{1}{2}\rho\, u^2\, (c\, b)\,, \quad F_L = C_L(\alpha)\frac{1}{2}\rho\, u^2\, (c\, b)\,, \tag{3.17}$$

where α is the ***angle of attack***, as displayed in Fig. 3.6. The lift-to-drag ratio F_L/F_D relates to the quality of the airfoil, which should be maximized.

Incident velocity

In Fig. 3.6, the velocity vector u_{res} gives the wind velocity in the frame of reference of the airfoil.

[2] Additional considerations such as mechanical loads or power stability are usually taken into account as well Bianchi *et al.* (2006), but reach out of the scope of this chapter.

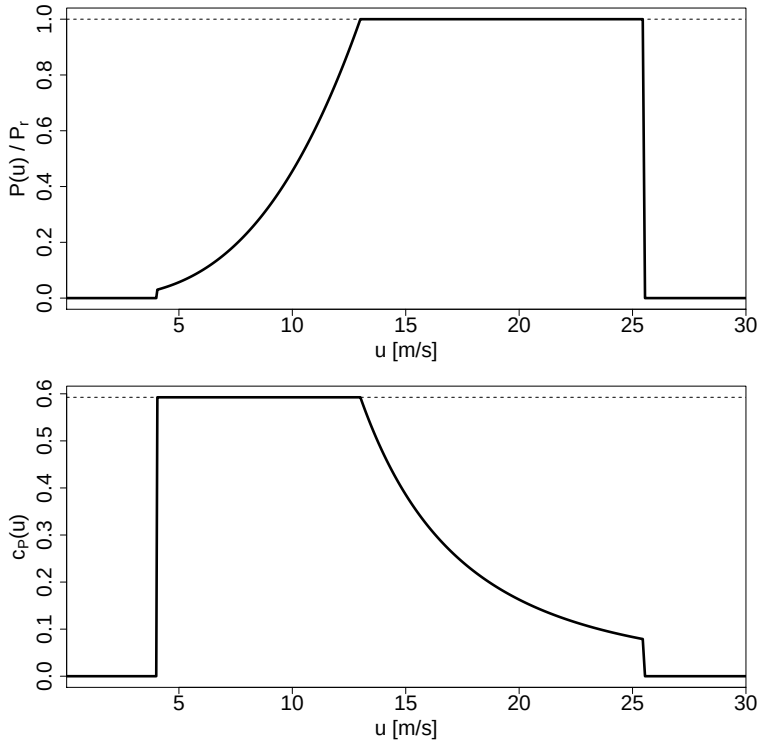

Fig. 3.5 : (a) Theoretical power curve $P(u)$; (b) Theoretical power coefficient $c_p(u)$ for a pitch-controlled wind turbine with $u_{cut-in} = 4$ m/s, $u_{rated} = 13$ m/s and $u_{cut-out} = 25$ m/s.

The wind velocity at the rotor is $\frac{2}{3}u_1$ in the frame of the ground, where u_1 is the free wind velocity upstream in front of the turbine. Additionally, the rotational motion must be considered for the motion of the wind with respect to the blades. The velocity of the rotational motion at a radial position r is $v = \omega r$, such that

$$u_{res}^2(r) = (2u_1/3)^2 + (\omega r)^2 \tag{3.18}$$

gives the effective or resulting velocity u_{res} of the air in the reference frame of the blade, see Fig. 3.6.

Forces on blade section dr

Blade element momentum theory is commonly used to estimate the total force acting on the rotor by summing up the local force on each infinitesimal blade element of size dr. The total force is divided into its rotational component F_r and its axial component F_a, which causes the thrust. Considering an infinitesimal cut dr at radial position r in the polar plane of the rotor, the infinitesimal components are

$$\begin{aligned} dF_r &= \frac{\rho}{2} u_{res}^2 \; c(r) \; dr \Big[C_L(\alpha) \; \cos(\gamma) - C_D(\alpha) \; \sin(\gamma) \Big] \; , \\ dF_a &= \frac{\rho}{2} u_{res}^2 \; c(r) \; dr \Big[C_L(\alpha) \; \sin(\gamma) + C_D(\alpha) \; \cos(\gamma) \Big] \; . \end{aligned} \tag{3.19}$$

Now we take the chord as a quantity that may change with the radius, i.e. $c = c(r)$.

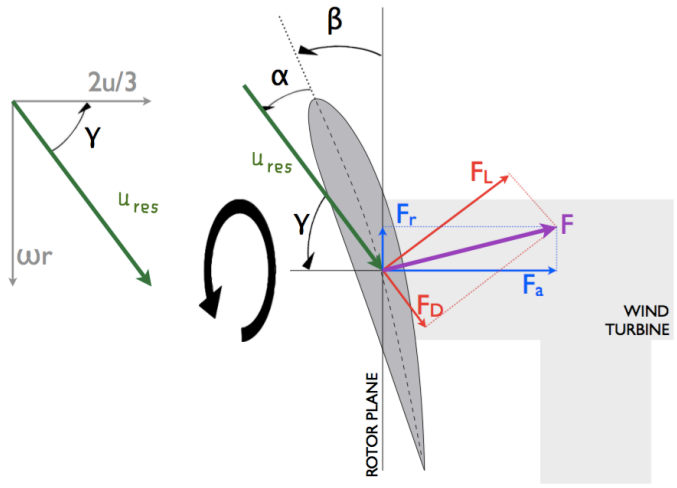

Fig. 3.6 : Cut through an airfoil rotating around the wind turbine axis. The rotational velocity ωr (gray) is perpendicular to the axial velocity $2u_1/3$ (gray). The angle of attack α is the angle between the air velocity u_{res} (green) and airfoil chord (dashed line). The pitch angle β denotes the angle between the chord and the plane of rotation. The lift and drag forces F_L and F_D are displayed (red), giving the total force F (purple), as well as the rotational and thrust projections F_r and F_a (blue).

Inflow angle

The angle $\gamma = \frac{\pi}{2} - \alpha - \beta$ (see Fig. 3.6) reads

$$\tan(\gamma) \;=\; \frac{\omega r}{2u_1/3} \;=\; \frac{3}{2}\frac{\omega R}{u_1}\frac{r}{R} \;=\; \frac{3}{2}\lambda\frac{r}{R}\,. \tag{3.20}$$

Power of blade section dr

Only the rotational component F_r is of use to rotate the rotor. The force F_a in the axial direction does not contribute to the power production but to the thrust acting on the turbine structure. F_a should be minimized to reduce mechanical fatigue. The infinitesimal power (force times velocity) associated to the rotational force acting on z rotor blades is

$$dP_{rot} \;=\; z\, dF_r\, \omega r \;=\; z\,\frac{\rho}{2}u_{res}^2\, c(r)\; dr\Big[C_L\cos(\gamma) - C_D\sin(\gamma)\Big]\,\omega r\,. \tag{3.21}$$

Optimized power leads to $c(r)$

The goal is to construct the blades in such a way that they extract the optimal power following Betz limit out of the wind. It should be noted that in this idealized case, the drag force is taken to be zero, which can be practically approached if $C_D \ll C_L$. Each infinitesimal radial annulus of size $2\pi r dr$ should extract a fraction $16/27$ of the wind power

$$dP_{ideal} \;=\; dP_{rot} \quad\Longleftrightarrow\quad \frac{16}{27}\,\frac{\rho}{2}\,u_1^3\,(2\pi r dr) \;=\; z\frac{\rho}{2}u_{res}^2\; c(r)\;\omega r\; dr\; C_L\cos(\gamma) \tag{3.22}$$

based on equation (3.21). In order to approach such ideal case, the blade depth $c(r)$ must follow

$$c(r) \;=\; \frac{16\pi}{9}\,\frac{1}{z\,C_L}\,\frac{R}{\lambda}\,\frac{1}{\sqrt{\lambda^2\frac{r^2}{R^2}+\frac{4}{9}}}\,. \tag{3.23}$$

For $r > R/7$ the square root gets approximately $\lambda\frac{r}{R}$ and thus we obtain

$$\boxed{\frac{c(r)}{R} \approx \frac{16\pi}{9}\frac{1}{zC_L\frac{r}{R}\lambda^2}}. \tag{3.24}$$

Here all lengths are given with respect to the blade length R. This approximation has an important consequence on the design of rotor blades. The depth $c(r)$ decreases when increasing either the number of blades, z, the lift coefficient C_L, the radius r or the tip speed ratio λ. This explains why fast rotating wind turbines tend to have only two or three narrow blades to optimize power extraction, while old western-mill machines have many, rather broad blades (in order to maximize mechanical torque).
As a last remark we point out that the optimized chord function $c(r)$ of eq. (3.24) was derived without any condition on the value of $C_L(\alpha)$. Thus an optimal blade shape can be designed also for values of the angle of attack α below the one that gives the maximal lift force. It is good to avoid maximal lift forces as for such conditions small fluctuations in the angle of attack may lead to the stall effect, a sudden decrease in lift.

3.3 IEC power curve and Annual Energy Production

In the previous sections, we have set theoretical models to predict and optimize power production, however, with 'laminar flow' approaches. Now, we look at real wind turbines, that operate in a ***turbulent, non stationary wind***. We describe a normalized way of ***monitoring power production performances***. We assume that wind velocities u and power P are measured at a sampling frequency of the order of a few Hz, and focus on the ***processing*** of these data. This processing is mainly performed in two steps.

After adequate normalization of the data, the first step consists in averaging the measured data over time intervals of 10 minutes. The ***IEC power curve*** (IEC 2005) is derived in a second step from the ten-minute averages using the so-called method of bins, i.e. the data is separated into wind speed intervals of width 0.5 m/s. In each of these intervals, labeled i, bin averages of wind speed u_i and power output P_i are calculated according to

$$u_i = \frac{1}{N_i}\sum_{j=1}^{N_i} u_{norm,i,j} \quad , \quad P_i = \frac{1}{N_i}\sum_{j=1}^{N_i} P_{norm,i,j}\,, \tag{3.25}$$

where $u_{norm,i,j}$ and $P_{norm,i,j}$ are the normalized 10-minute average values of wind speed and power, and N_i is the number of 10 min data sets in the i^{th} bin.

For the power curve to be complete and reliable, each wind speed bin must include at least 30 minutes of sampled data. Also, the total measurement time must cover at least a period of 180 hours. The range of wind speeds must range from 1 m/s below cut-in wind speed to 1.5 times the wind speed at 85% of the rated power of the wind turbine. The norm also provides an estimation of uncertainty as the standard error of the normalized power data, plus additional uncertainties related to the instruments, the data acquisition system and the surrounding terrain. A typical IEC power curve is presented in Fig. 3.7.

The IEC norm also defines the ***Annual Energy Production*** or AEP, as it will be presented in section 3.3.2 below. The AEP is a central feature for economical considerations, as it gives a first estimate of the long-time energy production of a wind turbine. As it sets a unique ground for

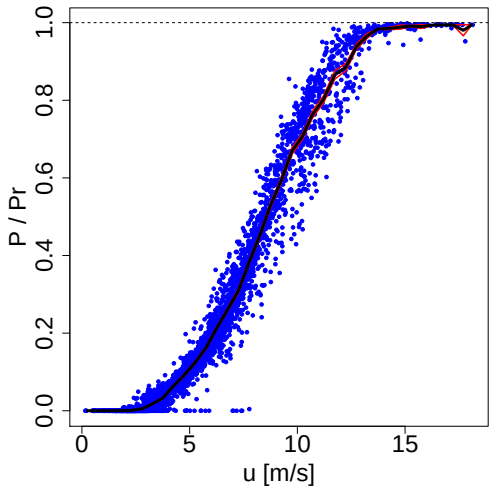

Fig. 3.7 : (color online) Typical power curve (black line) and corresponding error bars (thin red lines underneath) obtained according to the IEC norm. The blue dots represent the 10-minute average values.

wind power performance worldwide, the IEC norm helps building a general understanding between manufacturers, scientists and end-users. This statement comes to be ever more important as the wind energy sector grows. Hence, focusing on this standard is paramount to any study on power performance.

3.3.1 Turbulence-induced deviations

As a downside to its simplicity, the IEC power curve method presents a limitation. It suffers a physical and mathematical imperfection. In order to deal with the complexity of the wind speed and power signals, the data is systematically averaged over time. Although a statistical averaging is necessary to extract the main features from the complex processes, the averaging procedure over 10-minute intervals lacks a clear physical meaning, beyond its statistical definition. As the wind[3] fluctuates on various time scales (down to seconds and less), a systematic averaging over ten minutes filters out all the short-scale turbulent dynamics. Combining these turbulent fluctuations with the nonlinear power curve $P(u)$, $P(u)$ being proportional to u^3 for small u, and being more complicated for large u, the resulting IEC power curve is spoiled by mathematical errors. To show this, one can first split the wind speed $u(t)$ sampled at 1Hz into its mean value and the fluctuations around this mean value

$$u(t) = \overline{u(t)} + u'(t)\,, \tag{3.26}$$

where the operation $\overline{x(t)}$ on a given signal $x(t)$ represents the 10-minutes average of $x(t)$ as defined by the IEC norm. Assuming that $u'(t) \ll \overline{u(t)}$, a Taylor expansion of $P(u(t))$ reads (Böttcher *et al.* 2007)

$$\begin{aligned} P\left(u(t)\right) \;=\; & P\left(\overline{u(t)}\right) \;+\; u'(t)\left(\frac{\partial P(u)}{\partial u}\right)_{u=\overline{u(t)}} \\ & + \frac{u'(t)^2}{2!}\left(\frac{\partial^2 P(u)}{\partial u^2}\right)_{u=\overline{u(t)}} + \frac{u'(t)^3}{3!}\left(\frac{\partial^3 P(u)}{\partial u^3}\right)_{u=\overline{u(t)}} + o\left(u'(t)^4\right)\,. \end{aligned} \tag{3.27}$$

[3] To some extent the power output also fluctuates on short time scales, but its high-frequency dynamics are limited by the inertia of the wind turbine.

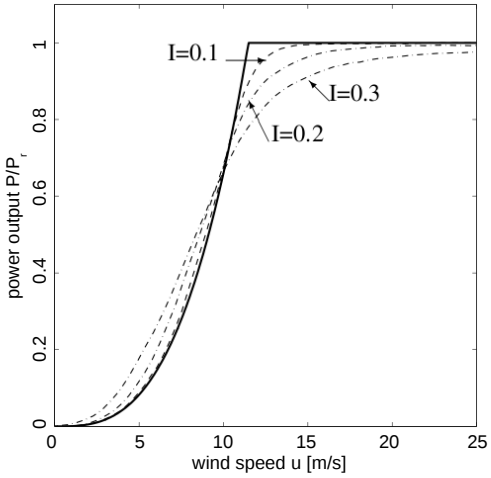

Fig. 3.8 : Typical IEC power curves for various turbulence intensities $I = 0.1,\ 0.2,\ 0.3$ (dashed lines). The full line represents the theoretical power curve. This result was obtained from numerical model simulations from Böttcher *et al.* (2007).

Averaging equation (3.27) yields

$$\overline{P\left(u(t)\right)} = P\left(\overline{u(t)}\right) + 0 + \frac{\overline{u'(t)^2}}{2}\left(\frac{\partial^2 P(u)}{\partial u^2}\right)_{u=\overline{u(t)}} + \frac{\overline{u'(t)^3}}{6}\left(\frac{\partial^3 P(u)}{\partial u^3}\right)_{u=\overline{u(t)}} + o\left(u'(t)^4\right), \quad (3.28)$$

because $\overline{u'(t)} = \overline{u(t) - \overline{u(t)}} = 0$. This means that the average of the power is not equal to the power of the average, and must be corrected by the 2^{nd} and 3^{rd}-order terms. As the IEC power curve directly relates the 10-minute averages of wind speed and of power output, it neglects the higher-order terms in the Taylor expansion. The 2^{nd}-order term is the product of the variance $\sigma^2 = \overline{u'(t)^2}$ of u(t)[4] and the second-order derivative of the power curve[5]. This demonstrates that the IEC power curve cannot describe in a mathematically rigorous way the nonlinear relation of power to wind speed when coupled with wind fluctuations (stemming from turbulence), at least not without higher-order corrections.

As a consequence of this mathematical over-simplification, the result depends on the 'turbulence intensity' $I = \sigma/\overline{u}$, so on the wind condition during the measurement Böttcher *et al.* (2007). It is illustrated in Fig. 3.8, where the IEC power curve deviates from the theoretical power curve with increasing turbulence intensity, as predicted by equation (3.28). As it does not characterize the wind turbine only, but also the measurement condition, this raises the question of its reproducibility and stability.

[4] $\sigma^2 = \overline{(u - \overline{u})^2} = \overline{u'(t)^2}$.

[5] Assuming a cubic power curve $P(u) \propto u^3$, $P(u)$ has non-zero derivatives up to 3^{rd}-order. Moreover, the transition point to rated power may have non-zero derivatives of arbitrary order, see Fig. 3.8.

3.3.2 Annual Energy Production

The one-dimensional *limitation* of the IEC power curve becomes an advantage for long-term energy production, as $P_{IEC}(u)$ relates unambiguously a unique value of power for each wind speed. As the AEP estimates the energy produced over a year, it can be seen as a prediction estimate. A prediction of power production at high-frequency is also possible using the Langevin approach, as it will be shown in the next section. The estimation of the AEP extrapolates the power production of a wind turbine characterized by its power curve in a given location. Here we do not give an exact transcription of the AEP procedure from the IEC norm (IEC 2005), but rather a comprehensive introduction on how power production can be estimated simply from a wind speed measurement. For such, the *AEP procedure* introduced here is not the official AEP procedure following IEC, but a similar version. In both cases, the availability of the wind turbine is assumed to be 100%.

Estimating the wind resource

Any location scheduled to host a wind turbine can be categorized in advance by a characterization of its wind resource. A local measurement of wind speed from a met mast at hub height[6] of the hypothetical wind turbine must be performed, typically over one year[7]. From this wind speed measurement $u(t)$, a ten-minute (or hourly) averaging is applied on $u(t)$. The probability density function (PDF) $f(u_i)$ of the ten-minute average values u_i is established. For clarity, the values u_i will be labelled u. $f(u)$ returns the probability of occurrence of the wind speed u. For long enough measurements, $f(u)$ is known to fit a ***Weibull distribution*** (Richardson 1922)

$$f(u;\lambda,k) = \frac{k}{\lambda}\left(\frac{u}{\lambda}\right)^{k-1} e^{(-u/\lambda)^k}\,, \tag{3.29}$$

where k and λ[8] are called respectively the ***shape*** and ***scale factors*** [9]. Visual examples of such wind speed distributions are given in Burton *et al.* (2001).

Estimating the AEP

A given wind site is characterized for the AEP by its wind speed PDF $f(u)$, while a given wind turbine is characterized by its IEC power curve. As P_{IEC} relates unambiguously a given wind speed u to the corresponding average power output $P_{IEC}(u)$, the power curve serves as a transfer function from wind speed to average power output. An estimation of the average power output $\overline{P}$ can be obtained following

$$\overline{P} \;=\; \int_0^\infty f(u)\; P_{IEC}(u)\, du\,, \tag{3.30}$$

and an estimation for the energy production over a period T reads

$$T\;\overline{P} \;=\; T\int_0^\infty f(u)\; P_{IEC}(u)\, du\,. \tag{3.31}$$

Over one year, $T = 8766$ hours, therefore

$$AEP \;=\; \overline{P}\;8766\,, \tag{3.32}$$

where $\overline{P}$ is given in Watt and AEP is given in Watt hour.

[6] Typical hub heights of commercial multi-MW class wind turbines are in the order of 100 m, justifying the interest for a portable LIDAR sensor...

[7] A measurement of wind speed over one year covers the various wind situations resulting from various seasonal behaviors.

[8] λ is not the tip speed ratio of a wind turbine, but a parameter of the Weibull distribution.

[9] IEC (2005) refers to the Rayleigh distribution, which is a special case of the Weibull distribution for $k = 2$.

Thanks to its simple mathematical procedure, the AEP is commonly used to make rough predictions of energy production, as well as for financial estimations. It can predict how much energy a wind turbine will generate on a given site before installing it. This allows for an optimal choice of design for the optimal location. This result however remains a rough estimation, as it neglects e.g. wake losses generated by other surrounding wind turbines.

3.4 A new alternative: the Langevin power curve

An alternative to the standard IEC power curve is proposed in this section. As the IEC norm defines the measurement procedure with relevance, the same conditions will be considered for the Langevin analysis. The difference lies in the different approach to process the measured data.

One additional point on the sampling frequency is however important for the Langevin analysis. Because the method resolves the dynamics of a wind turbine in the order of seconds, a minimum sampling frequency in the order of 1Hz is necessary for the measurements of wind speed and power output.

3.4.1 A dynamical concept

The power characteristic of a wind turbine can be derived from high-frequency measurements without using temporal averaging. One can regard the power conversion as a relaxation process which is driven by the turbulent wind fluctuations (Rosen & Sheinman 1994; Rauh & Peinke 2004). More precisely, the wind turbine is seen as a dynamical system which permanently tries to adapt its power output to the fluctuating wind. For the (hypothetical) case of a laminar inflow at constant speed u, the power output would relax to a fixed value $P_L(u)$[10], as illustrated in Fig. 3.9. Mathematically, these *attractive* power values $P_L(u)$ are called *stable fixed points* of the power conversion process.

3.4.2 The Langevin equation

The Langevin power curve[11] is derived from high-frequency measurements of wind speed $u(t)$ and power output $P(t)$. All necessary corrections and normalizations from the IEC norm IEC (2005) should be applied on the two time series.

The wind speed measurements are divided into bins u_i of 0.5 m/s width, as done in IEC (2005). This accounts, to some degree, for the non-stationary nature of the wind, yielding quasi-stationary segments $P_i(t)$ for those times t with $u(t) \in u_i$. The following mathematical analysis will be performed on these segments $P_i(t)$. From now on, the subscript i will be omitted and the term $P(t)$ will refer to the quasi-stationary segments $P_i(t)$. The power conversion process is then

[10] The subscript L stands for "Langevin" as $P_L(u)$ will be associated to the formalism of the Langevin equation.

[11] In former publications on the topic, the Langevin power curve was called *dynamical power curve* or *Markovian power curve*. It is nonetheless the same approach.

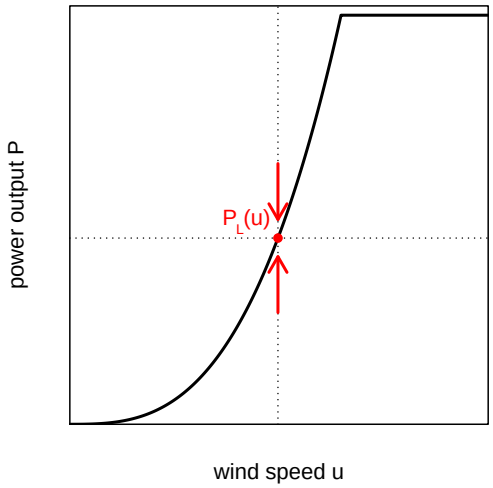

Fig. 3.9 : Illustration of the concept of stable fixed point $P_L(u)$. For constant wind speed, the power output would relax to a stable value $P_L(u)$. This sketch is inspired from Anahua *et al.* (2008).

modeled by a first-order stochastic differential equation called the ***Langevin equation***[12]

$$\boxed{\frac{d}{dt}P(t) \;=\; D^{(1)}(P) \;+\; \sqrt{D^{(2)}(P)}\,\Gamma(t)} \,. \tag{3.33}$$

In this model, the time evolution of the power output is controlled by two terms[13].

- $D^{(1)}(P)$ represents the deterministic relaxation of the wind turbine, leading the power output towards the attractive fixed point $P_L(u)$ of the system. For such, $D^{(1)}(P)$ is commonly called the ***deterministic drift function***.
- The second term $\sqrt{D^{(2)}(P)}\,\Gamma(t)$ represents the stochastic (random) part of the time evolution, and serves as a simplified model for the turbulent wind fluctuations that drive the system out of equilibrium. The function $\Gamma(t)$ is a Gaussian-distributed, delta-correlated ***noise*** with variance 2 and mean value 0. $D^{(2)}(P)$ is commonly called the ***diffusion function***. A mathematical approach to the Langevin equation can be found in Risken (1984).

The mathematical background for this 'Langevin' approach is presented in the Appendix A, which is an introduction to stochastic theory.

3.4.3 The drift function and the Langevin power curve

The deterministic drift function $D^{(1)}(P)$ is of interest as it quantifies the relaxation of the power output towards the stable fixed points of the system. When the system is in a stable state, no deterministic drift occurs[14], and $D^{(1)}(P) = 0$. Following equation (3.34), $D^{(1)}(P)$ can be understood as the average time derivative of the power signal $P(t)$ in each region of wind speed u_i and power output P.

[12] This equation is the reason for the name of the Langevin power curve.

[13] $D^{(1)}$ and $D^{(2)}$ are the first two coefficients of the general Kramers-Moyal coefficients.

[14] To separate stable (attractive) from unstable (repulsive) fixed points, also the slope of $D^{(1)}(P)$ must be considered.

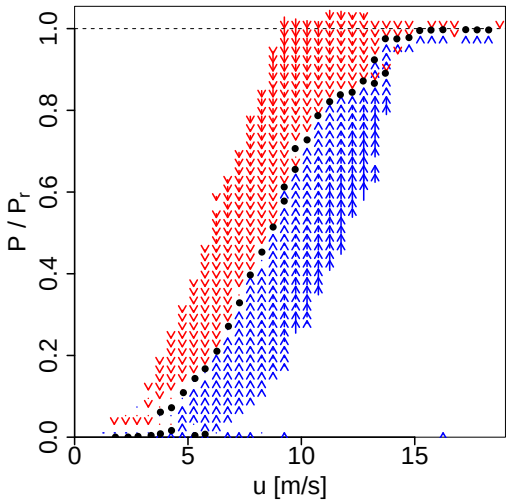

Fig. 3.10 : Typical drift function $D^{(1)}(P)$. Each arrow represents the local value of $D^{(1)}(P)$ in magnitude (length of the arrow) and direction (pointing up for positive values). The stable fixed points where $D^{(1)}(P) = 0$ are given by the black dots.

The drift and diffusion functions can be derived directly from measurement data as conditional moments (Risken 1984)

$$D^{(n)}(P) = \lim_{\tau \to 0} \frac{1}{n!\tau} \langle \left(P(t+\tau) - P(t)\right)^n \mid P(t) = P \rangle_t \,, \tag{3.34}$$

where $n = 1{,}2$ respectively for the drift and diffusion functions. The averaging $\langle \cdot \rangle_t$ is performed over t, as the condition means that the calculation is only considered for those times during which $P(t) = P$.

This means that the averaging is done separately for each wind speed bin u_i and also for each level of the power P. One could speak of a *state-based* averaging on u and P, in contrast to the temporal averaging performed in the IEC norm. A typical drift function is displayed in Fig. 3.10.

The dynamics of the power signal can be directly related to the local sign and value of $D^{(1)}$. A positive drift indicates that the power tends to increase (arrows pointing up in Fig. 3.10), in regions where the wind turbine does not produce enough power for the given wind speed. On the contrary, a negative drift corresponds to a decreasing power (arrows pointing down), in regions where the wind turbine produces too much power for the given wind speed. At the intersection are the points where $D^{(1)} = 0$, indicating that when at this value, the power output is in a stable configuration (the average time derivative is zero). The collection of all the points where the drift function is zero is defined as the ***Langevin power curve***, and will be further labelled $P_L(u)$.

The stable fixed points $P_L(u)$ of the power conversion process can be extracted from the measurement data as solutions of

$$D^{(1)}\left(P_L(u)\right) = 0 \,. \tag{3.35}$$

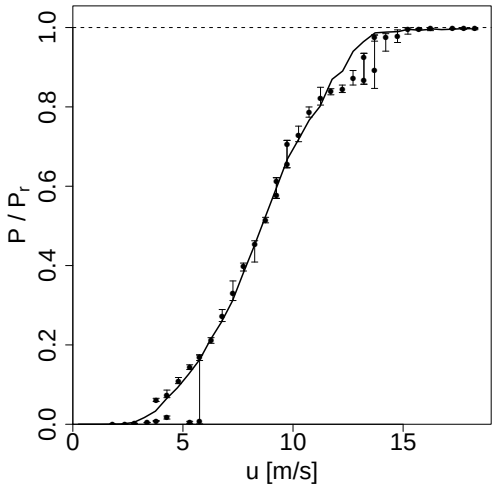

Fig. 3.11 : Typical Langevin power curve (black dots with corresponding error bars) and IEC power curve (solid line).

An illustration is given in Fig. 3.11.

Following the mathematical framework of equations (3.33) and (3.34), an estimation of uncertainty for $P_L(u)$ can be performed (Gottschall 2009). One can see on Fig. 3.11 that, for most wind speeds, the power curve has very little uncertainty. Nevertheless, larger uncertainties occur in the region of transition to rated power. There the power conversion is close to stability over a wider range of power values, as a consequence of the changing control strategy from partial load to full load operation (see Fig. 3.5). It is a region of great interest as the controller of the wind turbine is highly solicited for the transition to rated power.

3.4.4 Advantages of the Langevin approach

The Langevin equation (3.33) is a simplifying model for the power conversion process. The question of its validity for wind turbine power signals was positively answered in recent developments (Milan *et al.* 2010), as the power signal of a wind turbine could be successfully modelled. Also, the drift function $D^{(1)}$ is well-defined for a large class of stochastic processes, and is not limited only to the class of the Langevin processes.

Moreover, the definition of the drift function does not suffer the systematic errors caused by temporal averaging. For such, the Langevin power curve characterizes the wind turbine dynamics only, regardless of the wind condition during the measurement[15]. The results are therefore machine-dependent only, and not site- or measurement-dependent, as the intensity of turbulence has no influence on the Langevin power curve.

Additionally, this approach can show complex characteristics of the investigated system, such as regions where the system is close to stability, as mentioned above, or multiple stable states, see also Anahua *et al.* (2008); Gottschall & Peinke (2008). For these various reasons, the Langevin power curve represents a promising tool for power performance monitoring, too.

[15] Assuming that the measurement period is sufficiently long to reach statistical convergence.

3.4.5 Detecting dynamical anomalies

The intention of ***dynamical monitoring*** is to detect dynamical anomalies that appear on operating wind turbines. Monitoring refers to the time evolution of the power performance here. A good monitoring procedure should be reliable[16], as fast as available, and possibly also inform on the source of the anomaly. While monitoring procedures come to be ever more complex, the approach presented here is based only on a power curve estimation. This approach is not intended to give a full-featured method, but rather an illustration of the amount of information given by power curves. More advanced studies on the topic of power curves for monitoring are being developed, but remain outside the scope of this introduction as they represent active research topics.

The monitoring procedure simply consists in computing $P_L(u)$ at an initial time that will serve as a reference[17]. Potential changes in time of $P_L(u)$ are considered anomalies, or malfunctions inside the wind turbine that spoil the conversion dynamics. While this strategy is very simple, the challenge lies in defining the right threshold for a change in $P_L(u)$ to be considered an anomaly. This threshold, along with other parameters such as the necessary measurement time or time reactivity of the method depend on the wind turbine design and location.

To illustrate the ability of the method, the monitoring procedure was applied on a numerical simulation. The simulation was applied on measurement data, where an anomaly was introduced. This artificial anomaly limits the power production to $P \simeq 0.55\ P_r$ for intermediate wind speeds, as represented by the grey rectangles in Fig. 3.12 and 3.13. More clearly, when in this rectangle, the power signal was sometimes forced to reduce towards $0.55\ P_r$. From this artificial data, $P_L(u)$ and $P_{IEC}(u)$ were then computed and compared to the original data. This is illustrated in Fig. 3.12 and 3.13.

Similar anomalies were observed on several real wind turbines, justifying the reason for this artificial anomaly. For information, the total energy production was reduced to 96.6% compared to the original energy production due to the presence of the anomaly. Fig. 3.13 illustrates the higher reactivity of $P_L(u)$. While in Fig. 3.12 $P_{IEC}(u)$ only shows a minor deviation in the region of the anomaly, $P_L(u)$ clearly *detaches* from the typical cubic curve to adjust to the new dynamics. $P_L(u)$ can detect changes in the dynamics of the conversion process, unlike $P_{IEC}(u)$ that is better suited for the AEP.

> The Langevin power curve is more reactive to changes in the dynamics. As the IEC power curve averages over 10 minutes intervals, the information about high-frequency dynamics is lost. Also, the second averaging in wind speed prevents from seeing multi-stable behaviors.
>
> In addition, the Langevin power curve does not depend on the turbulence intensity, unlike the IEC power curve, see section 3.3.1. A deviation in the Langevin power curve indicates a change in the conversion dynamics, regardless of the wind situation. This makes the Langevin power curve a promising tool for dynamical monitoring.

[16] An over-sensitive procedure might indicate non-existing anomalies, while an under-sensitive procedure would fail to detect a major malfunction.

[17] The reference time is chosen when the wind turbine is believed to work with full capacity.

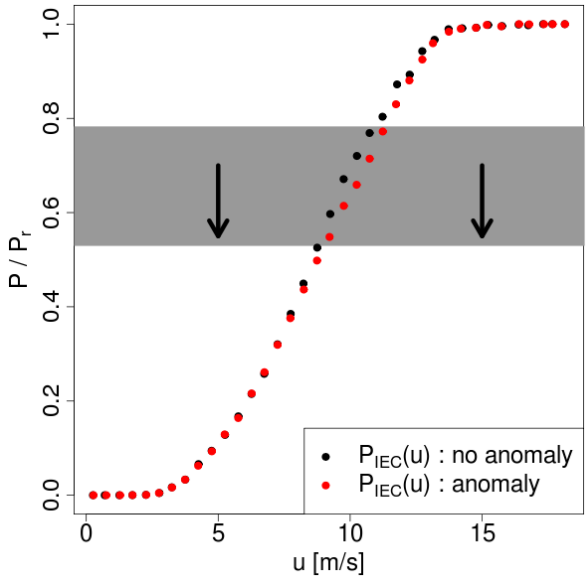

Fig. 3.12 : (color online) Comparison of $P_{IEC}(u)$ before the anomaly (black in background) and after the anomaly (grey or red in front). The artificial anomaly was applied in the grey rectangle.

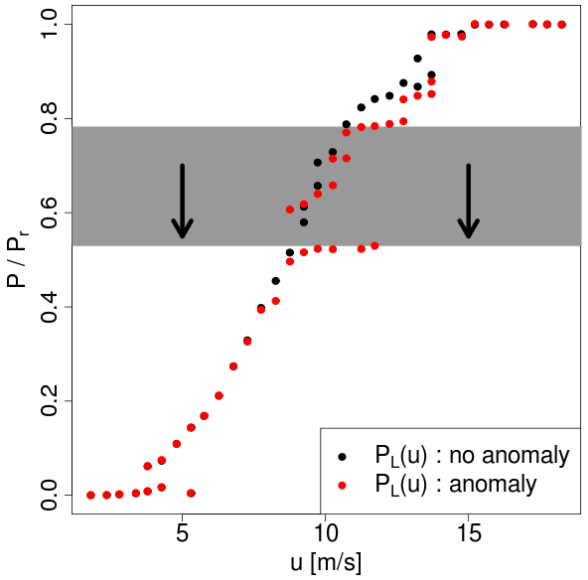

Fig. 3.13 : (color online) Comparison of $P_L(u)$ before the anomaly (black in background) and after the anomaly (grey or red in front). The artificial anomaly was applied in the grey rectangle.

3.5 Turbulence modelling

For the bibliography, especially concerning the 'old' papers, see Frisch (1995).

3.5.1 General definitions - Experimental results

The question here, to go beyond the basic description in terms of scales introduced in Plaut (2016), is how to characterize the ***spatial complexity of a turbulent field***. Of course, the starting point is still the definition of the two length scales between which the complex structures of turbulence are. There is a large scale L, called ***integral length scale***[18]. For scales larger than L, if they exist[19], unstructured, i.e. uncorrelated random fluctuations are left. In other words, L can often be defined as a correlation length. There is a small scale η, called ***dissipation or Kolmogorov scale***[20]. Any turbulent structure is smooth out by dissipation for length smaller then η. Thus the complex structure of turbulence lives at length scales between these two limiting scales L and η.

Besides these length there is the ***'turbulent energy'*** which determines the complexity. As turbulence is a dissipative structure, it can be sustained only if there is a permanent flow of energy into the system, i.e., a permanent power driving the flow structure. For a steady state there must be an equilibrium between the driving power and the dissipated power. This size is measured as a quantity ϵ called turbulent energy, what is not precise, as it is a power. Normalized by the mass the dimension is $[m^2/s^3]$. The cascade picture of turbulence is that this power ϵ is fed into the system at large scales, transfered by a cascade process to smaller scales and dissipated at smallest scales.

[18] Denoted ℓ in Plaut (2016).

[19] Often, L can be the size of the system.

[20] Denoted ℓ_K in Plaut (2016).

The spatial dependencies can be investigated by studying the ***velocity increments*** and their ***structure functions***, as defined below for a length scale r,

$$\eta \leq r \leq L \ .$$

Hereafter u (resp. $\overline{\mathbf{u}}$) denotes one component of (resp. the whole) velocity field. One uses a ***Reynolds decomposition***

$$\boxed{u \ = \ \langle u \rangle \ + \ u'} \tag{3.36}$$

with u' the fluctuating velocity.

Definitions

Velocity increments:

$$\boxed{u_r(x) := u(x+r) - u(x)} \ . \tag{3.37}$$

Structure functions:

$$\boxed{S^n(r) := \langle (u_r(x))^n \rangle = \langle (u(x+r) - u(x))^n \rangle} \ . \tag{3.38}$$

Comments

In principle all can be expressed for vectors: $u \to \overline{\mathbf{u}}$, $x \to \overline{\mathbf{x}}$ and $r \to \overline{\mathbf{r}}$.

Some ***probability density functions*** (PDF) $p(u_r)$ of velocity increments u_r for different values of r are shown in Fig. 3.14a. One observes a non-Gaussian character for small values of r, with events corresponding to large increments that are rather 'frequent', at least, with respect to what a Gaussian PDF would give. This is a signature of the ***intermittent character*** of small-scale turbulent flows. Observe that, for larger values of r, the PDF become more and more Gaussian. We will write a model for $p(u_r)$ in section 3.5.4, with the 'multiplicative cascade approach' by Castaing. However, firstly, we present 'older' models that paved the way to arrive to this point of view.

3.5.2 Kolmogorov & Obukov 1941

From the idea of a ***cascade***, Kolmogorov deduced that the structure function should be $S^n(r) = f(\epsilon, r)$ with ϵ the energy (power density) transferred in the cascade. Using dimensional analysis, one gets

$$S^n(r) \ = \ f(\epsilon, r) \ = \ C_n \ \epsilon^{n/3} \ r^{n/3} \tag{3.39}$$

with C_n a universal constant. For $n = 2$ we obtain $S^2(r) \sim r^{2/3}$, and for $n = 3$, $S^3(r) \sim r$, as tested experimentally in Fig. 3.15. Note the dimension of the "transferred energy" in the cascade $\epsilon \ \equiv \ E/(t \ m) \ \equiv \ \ell^2/t^3$.

Karmann, Howarth & Kolmogorov derived from the Navier-Stokes equation and isotropy the so-called $-\frac{4}{5}$***-law***

$$S^3(r) = -\frac{4}{5}\epsilon r + 6\nu \frac{dS^2(r)}{dr} \ . \tag{3.40}$$

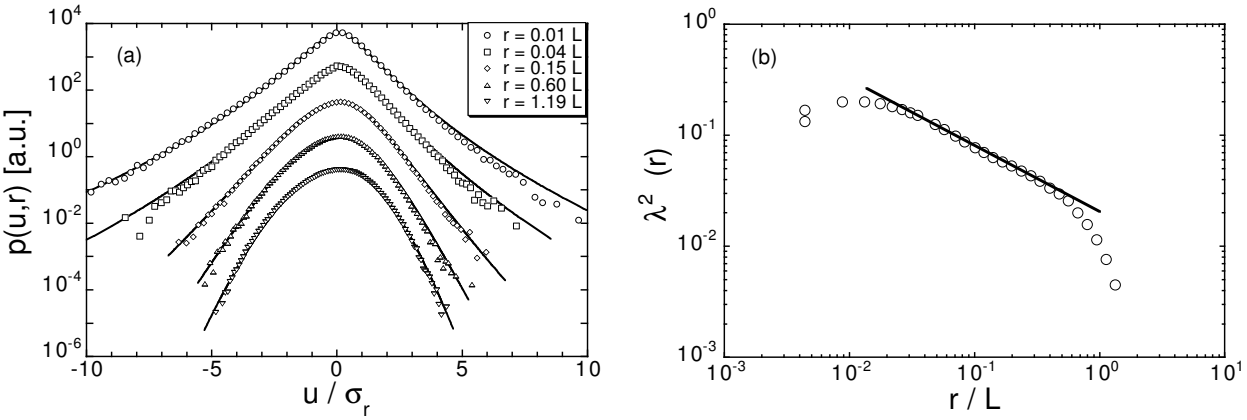

Fig. 3.14 : Statistical analysis of Experimental data acquired with Hot Wire Anemometry on a Laboratory Turbulent Flow, an air into air round free jet (Renner *et al.* 2001; these data are also available on the web page of the module). (a) : PDF $p(u_r)$ of the velocity increments u_r for different values of r; the values of u_r are normalized with the corresponding standard deviation σ_r of u_r. (b) : Corresponding form parameters, see eq. (3.60) below.

According to the eq. (3.39) $6\nu\frac{dS^2(r)}{dr} \propto r^{-1/3}$, thus for large scales ($r \to L$) one has $S^3(L) \propto -\frac{4}{5}\epsilon L$. From this L/η can be estimated. Using

$$\epsilon \approx \frac{S^3}{L} = \frac{< (u(x+L)-u(x))^3 >}{L} \approx \frac{< u'^3 >}{L} , \tag{3.41}$$

one obtains

$$\boxed{L/\eta = \frac{L}{\left(\frac{\nu^3}{\epsilon}\right)^{1/4}} = \frac{L\epsilon^{1/4}}{\nu^{3/4}} \approx \frac{L\frac{<u'^3>}{L}^{1/4}}{\nu^{3/4}} = \left(\frac{u'L}{\nu}\right)^{3/4} = Re^{3/4}} . \tag{3.42}$$

3.5.3 Kolmogorov & Obukov 1962

L.D. Landau pointed out that

> *'It is not obvious why ϵ is not a fluctuating quantity'.*

The idea of Kolmogorov 1941 can be taken as $\langle\epsilon_L\rangle = \langle\epsilon_r\rangle = \langle\epsilon_\eta\rangle$ - i.e the mean transfered energy in the cascade is conserved.

After the comment of Landau, Kolmogorov claimed that it is reasonable for $\epsilon(r)$ to assume a ***log-normal distribution***

$$p(\epsilon) = \frac{1}{\sqrt{2\pi\sigma^2}} \exp\left(-\frac{(\ln x)^2}{2\sigma^2}\right) . \tag{3.43}$$

Short argumentation for log-normal distribution

Some notations: The length scales of the turbulent cascade are denoted as $r_n < r_{n-1} < ...r_0 = L$, and $\epsilon_{r_i} := \epsilon_i$ the energy transferred at scale r_i.

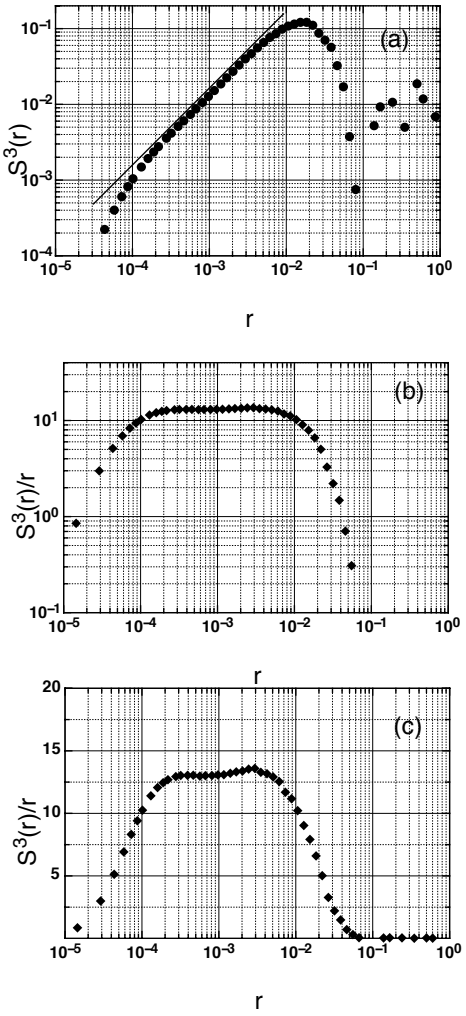

Fig. 3.15 : Experimental test of the law $|S^3| \propto r$, by Chabaud, B. & Chanal, O., CNRS Grenoble, France; reprinted from Friedrich & Peinke (2009). **(a)** Absolute value of the third-order structure function plotted with log-log scales. **(b)** and **(c)** absolute value of the compensated third-order structure function plotted with **(b)** log-log scales **(c)** log-lin scales.

The idea of a cascade is that now the sequence of $\epsilon_{r_1} = \epsilon_{r_2} = \ldots = \epsilon_L$ may become random by multipliers such that

$$\epsilon_i \;=\; a_i \; \epsilon_{i-1} \; .$$

The energy conservation is given by the condition $< a_i > \;=\; 1$. Thus one gets for the cascade:

$$\epsilon_{r_n} \;=\; a_n \; \epsilon_{r_{n-1}} \;=\; a_n \; a_{n-1} \epsilon_{r_{n-2}} \;=\; \ldots \;=\; a_n \; a_{n-1} \; \ldots \; a_1 \; \epsilon_L \; . \tag{3.44}$$

Taking the log of this equation:

$$\ln \frac{\epsilon_{r_n}}{\epsilon_L} = \sum_{i=1}^{n} \ln a_i \; . \tag{3.45}$$

This is now taken as a sum over independent random numbers $\ln a_i$. The "central limit theorem" from Kolmogorov says that such a sum of independent random numbers converges towards a

Gaussian distribution, hence

$$p(\epsilon_{r_n}) \;=\; p\left(\ln\frac{\epsilon_{r_n}}{\epsilon_L}\right) \;=\; \frac{1}{\sqrt{2\pi\Lambda^2}}\exp\left(-\frac{\left(\ln\frac{\epsilon_{r_n}}{\epsilon_L}\right)^2}{2\Lambda^2}\right) \tag{3.46}$$

where the variance Λ^2 can still be a function of r_n.

Kolmogorov 1962 assumes that

$$\Lambda^2(r) \;=\; \Lambda_0^2 - \mu\ln\frac{r}{L}\;. \tag{3.47}$$

Some argumentation for Kolmogorov 1962 hypothesis

As $\ln a_i$ are assumed to be uncorrelated ($\langle(\ln a_i)(\ln a_j)\rangle = 0$),

$$\Lambda^2(r) \;=\; \left\langle\left(\ln\frac{\epsilon_r}{\epsilon_L}\right)^2\right\rangle \;=\; \left\langle\left(\sum_{i=1}^{n}\ln a_i\right)^2\right\rangle \;=\; n\left\langle(\ln a_i)^2\right\rangle \;\propto\; n\;. \tag{3.48}$$

Thus $\Lambda^2(r)\sim n$ with n the depth of the cascade. Furthermore it is assumed that $r_{n+1} = k\,r_n$, for example $k = \frac{1}{2} \;\rightarrow\; r_{n+1} = \frac{1}{2}\,r_n$. Thus

$$\begin{aligned} r_{n+1} \;=\; k\,r_n \quad &\Longleftrightarrow \quad r_n \;=\; k^n\,L \\ &\Longleftrightarrow \quad k^n \;=\; \frac{r_n}{L} \\ &\Longleftrightarrow \quad n\,\ln k \;=\; \ln\frac{r_n}{L} \\ &\Longleftrightarrow \quad n \;=\; \ln\frac{r_n}{L}\,\frac{1}{\ln k}\;. \end{aligned}$$

As $k<1$, is follows that $\ln k<0$. Thus we can define $\mu := -\frac{1}{\ln k}$ and one obtains

$$n \;=\; -\,\mu\ln\frac{r}{L}\;. \tag{3.49}$$

Thus the hypothesis follows

$$\Lambda^2(r) \;=\; \Lambda_0^2 - \mu\ln\frac{r}{L} \tag{3.50}$$

with μ an ***intermittency coefficient***.

Knowing $p(\epsilon)$ and $\Lambda^2(r)$ one can calculate

$$\langle\epsilon^{n/3}\rangle \;\sim\; r^{-\mu\frac{n(n-3)}{18}}\;.$$

This is the results of Obukov & Kolmogorov 1962.
One deduces from this that the structure functions

$$S^n(r) \;=\; C_n\langle\epsilon^{n/3}\rangle r^{n/3} \;\sim\; C_{\epsilon_n} r^{n/3-\mu\frac{n(n-3)}{18}} \tag{3.51}$$

This equation is known as the ***intermittency correction*** to Kolomogov 1941 (3.39). It is easy to see that for $n=3$ (3.51) the $-\frac{4}{5}$***-law*** is fulfilled, and that

$$S^2(r) \;=\; C_{\epsilon_2} r^{2/3+\mu\frac{1}{9}}\;, \tag{3.52}$$

$$S^3(r) \;=\; C_{\epsilon_3} r\;, \tag{3.53}$$

$$S^6(r) \;=\; C_{\epsilon_6} r^{2-\mu}\;. \tag{3.54}$$

S^6 is good to estimate the intermittency correction μ.

The structure functions can also be seen as ***spatial 2-point-correlations***,

$$S^n(r) \;=\; \langle (u(x+r)-u(x))^n \rangle \;=\; \langle u_r^n \rangle \;=\; \int_{-\infty}^{\infty} u_r^n p(u_r) du_r \;. \tag{3.55}$$

Thus the structure functions $S^n(r)$ are the general moments of $p(u_r)$.
If the increments u_r are normalized by $\sqrt{< u_r^2 >}$ to $u_r = \sqrt{< u_r^2 >}\, w_r$ we obtain

$$S^n(r) \;=\; \int_{-\infty}^{\infty} u_r^n p(u_r) du_r \;=\; < u_r^2 >^{n/2} \int w_r^n P(w_r)\, dw_r \;. \tag{3.56}$$

If the integral over w_r is independent of r , this is the case if $P(w_r)$ is the same for all r, then Kolmogorov 1941 is obtained again. The other way round, from the intermittency correction, expressed by μ must have the consequence that $P(w_r)$ is changing its from with r.

3.5.4 Multiplicative cascade after Castaing

We follow here Castaing *et al.* (1990). One studies the ***probability density function*** (PDF) $p(u_r)$ of the velocity increments. One can write $p(u_r)$ as function of the conditioned probability $p(u_r|\epsilon_r)$, as

$$p(u_r) \;=\; \int_0^{+\infty} p(u,\epsilon_r,r)\, d\epsilon_r \;=\; \int_0^{+\infty} p(u_r|\epsilon_r)\, p(\epsilon_r,r)\, d\epsilon_r \,. \tag{3.57}$$

Castaing assumed (all this is experimentally verified, see e.g. Naert *et al.* 1998) that $p(u_r|\epsilon_r)$ is Gaussian distributed:

$$p(u_r|\epsilon_r,r) \;=\; \frac{1}{\sqrt{2\pi}\, s(\epsilon_r)} \exp\left(-\frac{u^2}{2\, s^2(\epsilon_r)}\right) \;. \tag{3.58}$$

Next the standard deviation s depends on ϵ_r as

$$s(\epsilon_r) \;\propto\; \epsilon_r^{\alpha} \,. \tag{3.59}$$

As $\ln(s) \propto \alpha \ln(\epsilon_r)$ also s must be log-normal distributed. Thus

$$p(u_r) \;=\; \frac{1}{2\pi\lambda(r)} \int_{-\infty}^{+\infty} \exp\left(-\frac{\ln^2(s/s_0(r))}{2\lambda^2(r)}\right) \exp\left(-\frac{u^2}{2s^2}\right) \frac{d\ln s}{s} \,. \tag{3.60}$$

There are two parameters $s_0(r)$ and $\lambda^2(r)$. The first one $s_0(r)$ is the maximum of the distribution of s and determines the variance of $p(u_r)$. The second one $\lambda^2(r)$ is the variance of the log-normal distribution for s. It determines the form of $p(u_r)$ and is thus called the ***form parameter***. In the limit $\lambda^2(r) \to 0$ a Gaussian distribution is obtained. This is the case for $r > L$, as shows the Fig. 3.14a. On the contrary for small scales r the values λ^2 increase thus a departure from Gauss is seen. By fitting the $p(u_r)$, on can estimate the parameter $\lambda^2(r)$ (Fig. 3.14b). Thus informations on $\Lambda(r)$ can be obtained, since, as shown in Castaing *et al.* (1990), $\Lambda = 3\lambda$.

3.6 Data analysis - Wind data

As can be deduced from the previous Section, ***Wind Turbulence*** leads to ***power fluctuations***, ***fatigue*** and ***extreme loads*** on Wind Turbines. Therefore a thorough description and characterization of wind turbulence is crucial for a reliable design and efficient operation of Wind Turbines. On the other hand, due to the presence of many phenomena at many different scales in the atmosphere, a comprehensive and direct analytical description of turbulence remains a challenge.

A way to handle this complexity is to describe the phenomena in terms of statistical quantities. However which statistical information is necessary and sufficient for a certain purpose is not a trivial question. A useful characterization should enable comparison of wind situations between different sites and allow for the adequate selection of a Wind Turbine class and layout. IEC (2005) defines a procedure to achieve these requirements based on 10 minutes mean values of the wind speed and respective deviations from this mean. Definitions are given for Wind Turbine classes, wind situations and probability estimations of certain extreme events. While necessity and usefulness of standards are beyond doubt, in the recent years growing demand for a more comprehensive and more detailed characterization has become evident. This is an active field of research, for example Bierbooms (2009) worked on the extreme operative gust and how to incorporate this in the generation of synthetic wind time series. Also recently in Larsen & Hansen (2008) calibrations of the extreme cases with return periods of 50 and 1 years in the standard IEC 61400 were presented. Common to the cited works is the explicit role of the particular Wind Turbine under consideration.

Here we try to review and clarify which kind and which amount of information is grasped by different levels of statistical descriptions of wind turbulence. Our aim is not to give a detailed review of every different statistical approach, but to provide a general and systematic framework which allows to classify and distinguish these approaches and their reach. This is particular important for a systematic review of the statistical methods present in the mentioned IEC norm, while recognizing the value and power of the methods therein but also in the realization of their limitations and where they stand within a systematic and consistent statistical description of wind turbulence. Such statistical framework is also important when defining benchmarks for synthethic and simulated turbulent wind fields.

The structure of this section is such, that with every subsection more statistical information for the description of the wind turbulence is taken into account, therefore enhancing the classification of wind turbulence gradually from low order one-point statistics to n^{th}-order two-point statistics, look at Tab. 3.1 page 82. Note also that we differentiate between statistics taken from some data point x_i or taken from pairs of data like x_i, x_{i+n}, the latter is denoted as two-point statistics. Based on examples we show the suitability and completeness of every step of the statistical description. Thus we start with one-point statistics proceed with two-point statistics and finally comment on n-point statistics. Each time lower and higher order moments of the statistics are discussed.

For illustration purposes we use wind data of the research platform FINO 1[21]. Trying to avoid wake effects caused by the measurement tower we use data from the top anemometer at 100 m height. The wind speed is recorded with a sampling rate of 1 Hz, for our examples we used one month of data namely January 2006. For simplicity we work just with the horizontal magnitude $u(t)$ of the wind velocity vector. It is straight forward to extend our scheme to different directional components of the wind vector, as well as to spatial instead of temporal separations.

[21] http://www.fino1.de/en .

To demonstrate the importance of this method of data analysis, we compare the results from measured data with a synthetic time series, which was obtained from a common package used by the wind energy community called TurbSim[22].

3.6.1 One-Point Statistics

One-Point Statistics up to Second Order

Given a wind time series, a common approach in the context of wind energy is to define ***turbulent fluctuations*** $u'(t)$ superimposed over a ***mean wind speed*** (Burton *et al.* 2001),

$$u(t) = \langle u \rangle_T + u'(t)_{\langle u \rangle_T}. \tag{3.61}$$

Here $\langle \cdot \rangle$ denotes time average and T the particular time span taken for calculating the average. In general $\langle x^n \rangle$ is the n^{th} moment of x. These fluctuations around the mean value have themselves a mean value of zero, $\langle u'(t)_{\langle u \rangle_T} \rangle = 0$. Fig. 3.16 (a) shows a typical wind time series and its 10 minutes mean values. Fig. 3.16 (b) shows the corresponding fluctuations $u'(t)$. Note that in our notation the index in $u'(t)_{\langle u \rangle_T}$ makes explicit the fact that these fluctuations are always defined through $\langle u \rangle_T$. In our case we take a simple average over the time window T, filtering or more elaborated detrending methods would change the actual value of u' and there statistical properties.

One issue with this definition is the need of an averaging period T over which to define the mean wind speed used as reference for the fluctuations. Due to the strong non-stationarity of the wind, this task is not trivial, but 10 minutes spans are the usual practice. This particular time span is often motivated by the so-called 'spectral gap', cf. Stull (1994). It is assumed that there is a clear cut between mesoscale variations (large-scale meteorological patterns) and high frequency fluctuations. Another argumentation for an averaging time scale T could be attributed to the response dynamics of a Wind Turbine. Wind Turbines can follow adiabatically changes in the wind acting on sufficiently large time scales. In this way one might propose a Wind Turbine based time span T, which would change from Wind Turbine to Wind Turbine, depending on size and control system.

For simplicity, from now on we will just write $u'(t)$ for $u'(t)_{\langle u \rangle_T}$, and we will also adopt the usual $T = 10$ min. Our following arguments could be applied to any other characteristic or desired value of T.

In addition to the 10 minutes mean values $\langle u \rangle_{10min}$, an estimation of turbulence strength in the wind during the time span T is the ***turbulence intensity***

$$\boxed{I = \frac{\sqrt{\langle u'^2 \rangle}_T}{\langle u \rangle_T} = \frac{\sigma_T}{\langle u \rangle_{10min}}}. \tag{3.62}$$

Here σ_T is the standard deviation of the fluctuations departing from the mean wind speed in the considered period of time. The turbulence intensity is a crucial parameter by which, e.g., certification and site assessment procedures are defined, and it is indeed a design constraint IEC (2005). Details on how this parameter changes with height, mean wind speed or surface roughness can be found for example in IEC (2005); Hansen & Larsen (2005) and for offshore data in Türk & Emeis (2007). As important as it is, the statistical information of this parameter is restricted to the standard deviation or the second moment of the fluctuations. Formally the statistics contained

[22] https://nwtc.nrel.gov/TurbSim .

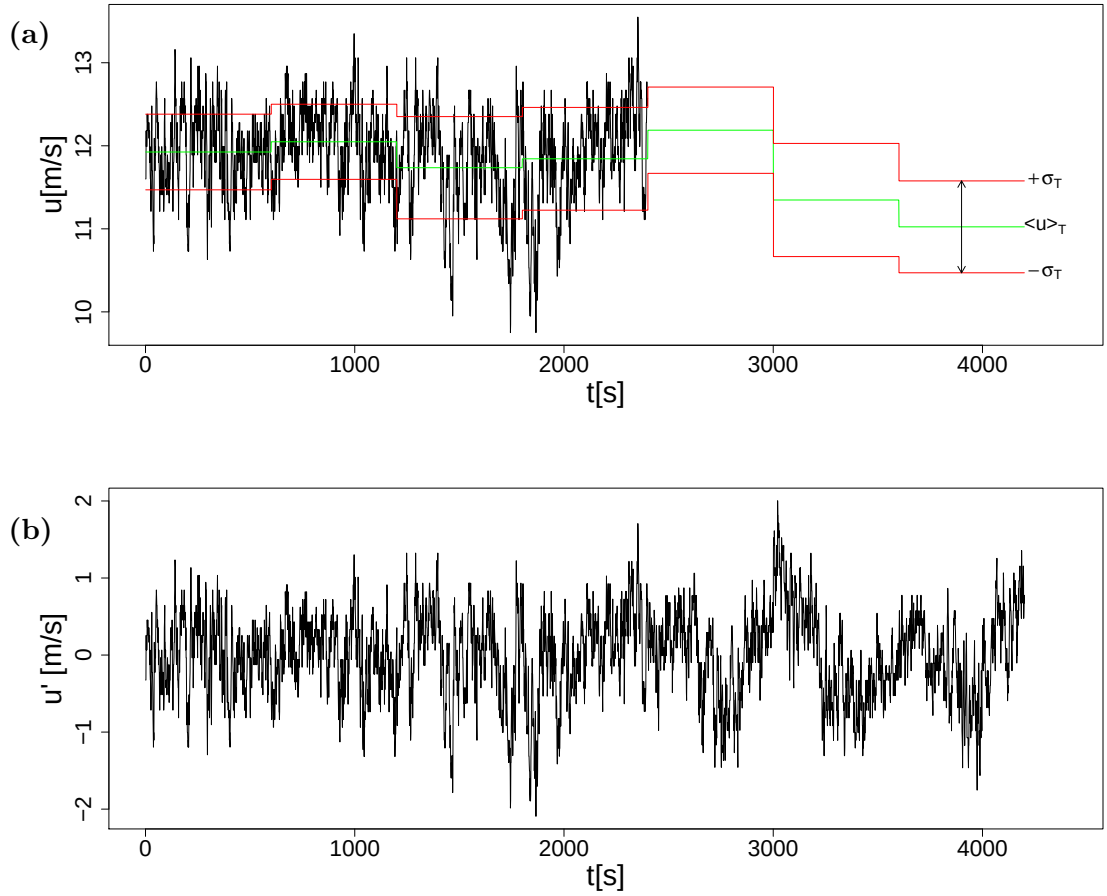

Fig. 3.16 : (a) Time series of the horizontal wind speed $u(t)$ measured on the research platform FINO I at 100 m height, with 10-minute mean values and standard deviations. (b) Fluctuations $u'(t)$ defined over 10-minute mean values.

in the turbulence intensity are one-point statistics of second order. As we will introduce in the next section, higher order moments of the fluctuations, $\langle u'^n \rangle$ with $n > 2$, are necessary for the description of extreme values of u'.

Higher Order One-Point Statistics

In the previous subsection we discussed first-order ($\langle u \rangle_{10min}$) and second-order ($\sigma_T$) one point statistics. In general higher order moments are also significant, and this information is contained in the form of the probability density function (PDF) of fluctuations, $p(u')$. Generally, for a PDF there are as characterising quantities, its mean value, its width or standard deviation and its form, which may be Gaussian or not and which is best shown in a normalized presentation, $p(u'/\sigma)$. Note, $\langle x^n \rangle = \int x^n p(x) dx$, the complete set of moments is contained in the knowledge of the PDF of a statistical quantity. The only case where the first two moments will give a complete description of one-point statistics, is the case where the PDF of the fluctuations follows a Gaussian distribution, since only this distribution is completely defined by its first two moments.

The question whether wind fluctuations follow a Gaussian distribution or not becomes relevant in order to understand how much parameters like the turbulence intensity I are needed to char-

acterize such fluctuations. To consider the Gaussianity of the fluctuations, Fig. 3.17 presents the PDFs for different sets of $u'(t)$. Fig. 3.17a shows the PDFs for some arbitrary single 10-minutes intervals. Which can be understood as $p(u'(t)|\sigma_T^i)$, where σ_T^i denotes the standard deviation of the i^{th} 10-minutes interval. Within such intervals fluctuations seem to follow the Gaussian distribution, and the pdfs can be characterized by the corresponding σ_T^i. In contrast to this in Fig. 3.17b the complete set (20 days) of $u'(t)$ is shown. We see that in this case the probabilities of large values of fluctuations are clearly underestimated by a Gaussian distribution. Note the logarithmic y-axis and note that the observed $10\sigma_\infty$ events are underestimated by the Gaussian distribution by a factor of 10^8 i.e. this probability difference translates into the event ocurring once every week or once every 2 10^6 years.

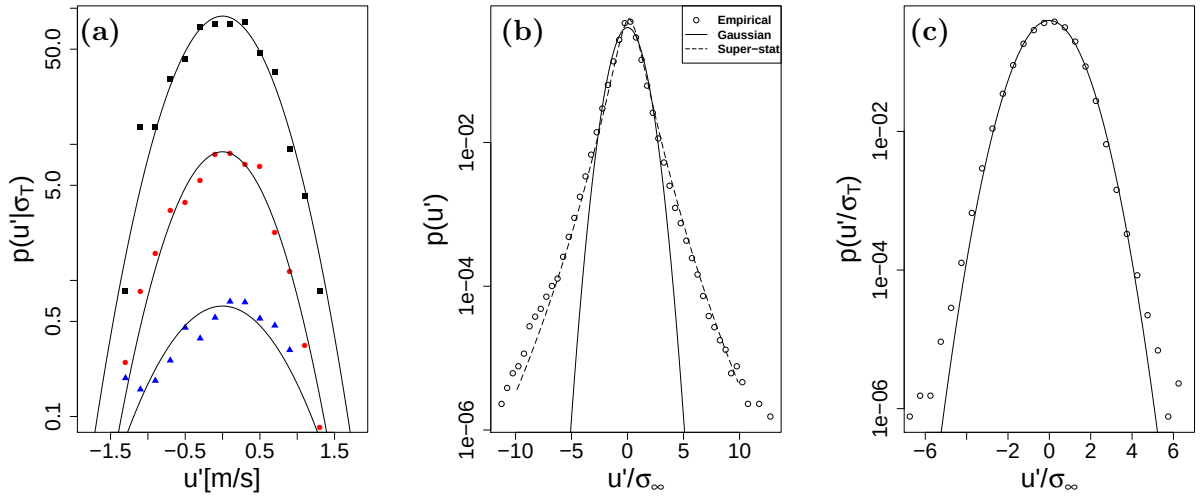

Fig. 3.17 : (a) $p(u'(t)|\sigma_T)$ for three arbitrary ten-minute intervals. From top to bottom the values of the respective σ_T are 0.456, 0.452 and 0.616 m/s, the flatness $\langle u'^4\rangle/\sigma_T^4$ are 2.82, 2.82, and 2.89 ± 0.79. (b) PDF of $u'(t)$ considering all the data set. The flatness is 6.30 ± 0.11, and $\langle (ln\sigma'_T - \overline{ln\sigma'_T})^2\rangle = 0.2037$. (c) PDF of $u'(t)/\sigma_T$ where σ_T is the standard deviation in each interval of length T (see also discussion with the text). Flatness is 2.98 ± 0.01. Symbols represent wind data and solid lines Gaussian distributions in all figures.

Finally Fig. 3.17c shows again the PDF of the total data set, but here in each i^{th} 10-minutes interval the fluctuations $u'(t)$ were normalized by the corresponding σ_T^i standard deviation of the respective i^{th} 10-minutes interval. For these locally rescaled fluctuations, the resulting PDF $p(u'(t)/\sigma_T^i)$ is well described by a Gaussian distribution within $\pm 5\sigma$. Small deviations may be seen for the largest values, but the significance here is rather questionable. Nevertheless comparing Fig. 3.17b and c we clearly see that for $p(u'(t)/\sigma_T^i)$ a Gaussian distribution is a very good approximation.

These findings support the hypothesis that $u'(t)$ is Gaussian distributed within ten minute intervals, but with different standard deviations σ_T for each interval. It is known that the standard deviations σ_T of $u'(t)$ for single ten-minute intervals are closely log-normal distributed and the parameters of the log-normal distributions depend on the mean wind speed (Hansen & Larsen 2005). Thus if fluctuations $u'(t)$ are considered without normalization, the superposition of the different Gaussians distributions with different σ_T leads to the intermittent distribution in Fig. 3.17b.

For a more quantitative evaluation of deviations from Gaussianity, it is common to calculate the third and fourth moments of the fluctuations normalized by the standard deviation, which are

called ***skewness*** *Skew* and ***flatness*** F, respectively. For a general signal $x(t)$ the definitions are

$$Skew(x) = \frac{\langle (x - \bar{x})^3 \rangle}{\sigma_x^3} \tag{3.63}$$

$$F(x) = \frac{\langle (x - \bar{x})^4 \rangle}{\sigma_x^4} \,. \tag{3.64}$$

A Gaussian distribution has a skewness value of zero and a flatness of three. For all the cases in Fig. 3.17, the values of the skewness do not differ significantly from zero, confirming the symmetry of the distributions. The values of the flatness are 2.82, 2.82, and 2.89 ± 0.79 from top to bottom in Fig. 3.17a and thus do not contradict the Gaussian distribution for arbitrary single ten-minute intervals, while the large deviations from Gaussianity in Fig. 3.17b result in a flatness of 6.30 ± 0.11. For the PDF of all the rescaled ten-minute intervals in Fig. 3.17c the flatness of 2.98 ± 0.01 is again surprisingly close to the Gaussian value.

From the discussion above it follows that an assumption of Gaussianity for $u'(t)$ holds only for single ten-minute intervals, and caution should be taken when estimating the probability of extreme values of u', where the actual values of u' and not the rescaled vaules u/σ_T are relevant. Here general higher moments than $\langle u'^2 \rangle$, or related quantities like the flatness (see eq. 3.64), will be needed for a correct description of $p(u')$. This non-Gaussianity of the extreme excursions from the mean wind speed has been already noted in, e.g., Panofsky & Dutton (1984). More recently in Larsen & Hansen (2006) an asymptotic expression for describing the distribution of such extreme events was presented.

Based on our above findings that $p(u'(t)|\sigma_T)$ can be approximated by a Gaussian, we can apply a superposition approach similar to Castaing *et al.* (1990),

$$p(u') = \int p(u'|\sigma'_T) \cdot p(\sigma'_T) d\sigma'_T. \tag{3.65}$$

Here $p(u'|\sigma'_T)$ represents a Gaussian distribution and $p(\sigma'_T)$ a log-normal distribution. The key parameter is $\langle (\ln \sigma'_T - \overline{\ln \sigma'_T})^2 \rangle$ which gives directly a measurement of the intermittency of $p(u')$ and is therefore actually related to the flatness of the distribution. Fig. 3.17b shows that our model based on equation (3.65) is able to describe the PDF $p(u')$ properly even in the tails.

Up to this point we have been discussing stepwise one-point statistics of first order $\langle u \rangle$, of second order in σ_T, and of higher orders summarized in the PDF of u'. However even a complete knowledge of $p(u')$, or respectively of all the moments $\langle u'^n \rangle$, is not unique in the sense that many different time series can share these statistics. To make this point more clear we refer to Fig. 3.18, which shows three time series which have Gaussian distributions $p(u')$. Those time series share the same one-point statistics, thus the same value of standard deviation and will give the same value of turbulence intensity once added to the same mean wind speed. Clearly the nature of these time series is different.

This is not surprising since the PDF of $u'(t)$ gives no information regarding which path the process follows in order to achieve the observed distribution. In order to distinguish more features of the time series a proper correlation analysis is necessary. The next section will therefore deal with the characterization of correlations by two-point statistics.

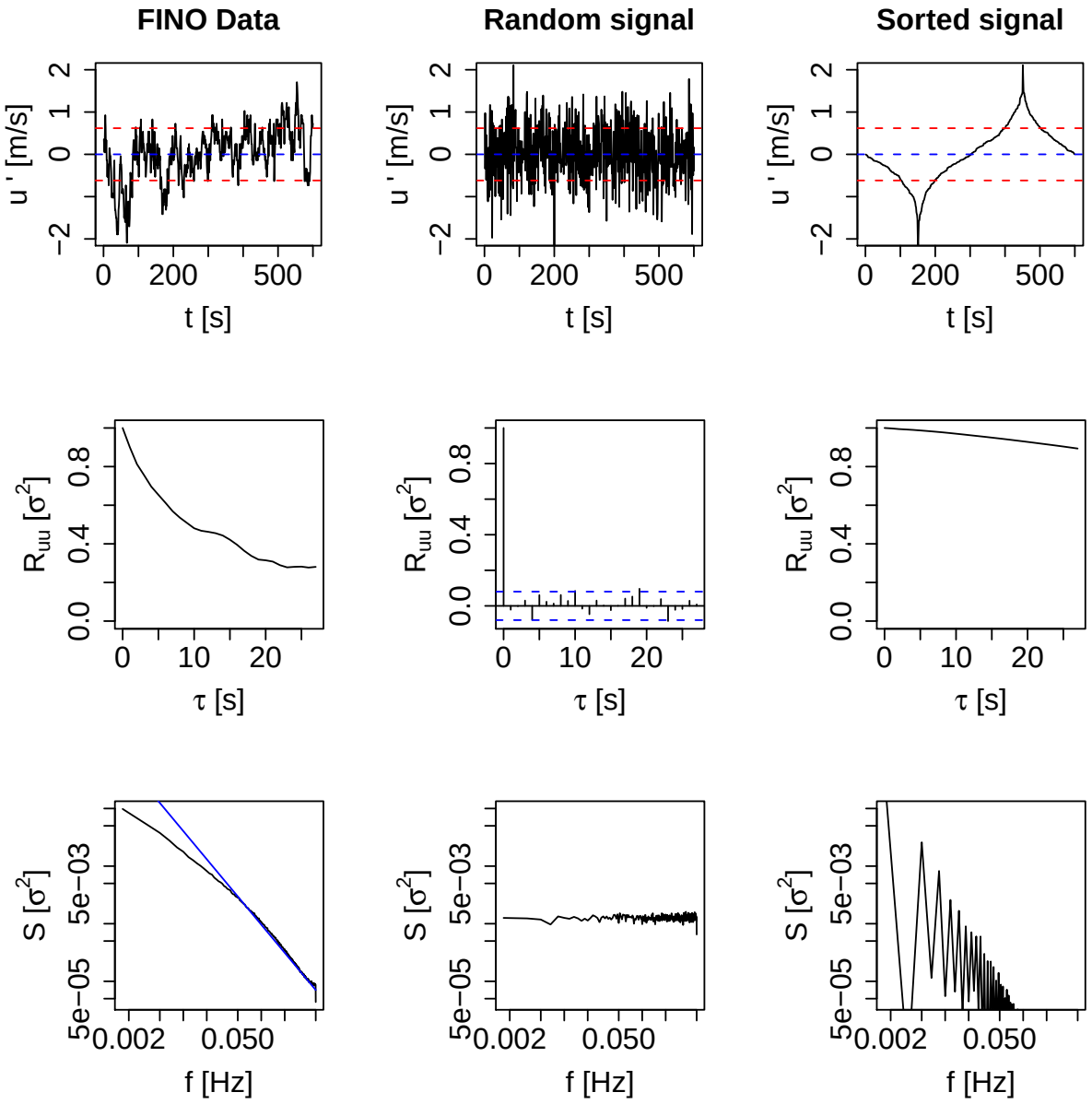

Fig. 3.18 : Three different time series, their autocorrelation functions $R_{u'u'}(\tau) = \langle u'(t+\tau)u'(t)\rangle$, and power spectral densities $S(f)$. From left to right, atmospheric fluctuations u' (measured at FINO 1), a random Gaussian distributed time series, and an ordered time series constructed from the random series. All three share the same standard deviation σ_T, and closely the same $p(u')$. In the top column the dashed lines correspond to one standard deviation. The straight line shown with the FINO 1 power spectral density corresponds to $S(f) \propto f^{-5/3}$. From the figure it is clear how even a complete knowledge of one-point statistics is not sufficient in order to characterize wind turbulence.

3.6.2 Two-point statistics

Two-point statistics up to second order

As seen previously and in Fig. 3.18 it is in general necessary to obtain knowledge on the correlations between two points in the time series of wind fluctuations. The basic statistical tool for this purpose is the autocorrelation function

$$R_{u'u'}(\tau) \;=\; \frac{1}{\sigma_{u'}^2}\left\langle u'(t+\tau)\, u'(t)\right\rangle \tag{3.66}$$

which quantifies the correlation of two data points separated by the time lag τ. The Wiener-Khintchine theorem (Press *et al.* 1996) relates it to the power spectral density $S(f)$ via a Fourier Transformation $\mathcal{F}$, thus both functions contain the same information:

$$S(f) \overset{\mathcal{F}}{\Longleftrightarrow} R_{u'u'}(\tau) \quad \text{with} \quad \sigma_{u'}^2 \;=\; \int S(f)\mathrm{d}f\,. \tag{3.67}$$

These are second order two-point statistics and give information on the intensity or amplitude with which different frequencies contribute to the fluctuations. This statistical tool already enables us to distinguish between the signals shown in Fig. 3.18 despite that they share the same one-point statistics. As we can see in Fig. 3.18 in the case of the random signal our description would be complete with the turbulence intensity because the PDFs of the fluctuations are Gaussian and the fluctuations are completely uncorrelated, i.e.,

$$R_{u'u'}(\tau) \;=\; \delta(\tau). \tag{3.68}$$

However as we know this special case would be very difficult to find in the atmosphere where many different interactions occur over many scales Stull (1994). Instead as can be seen again in Fig. 3.18 the atmospheric turbulence exhibits a lot of structure regarding the power spectrum. In the so-called inertial range usually a Kolmogorov similarity theory is adopted in order to explain the spectrum over a range of frequencies ($S(f) \propto f^{-5/3}$). In practice either the Kaimal or the von Karman spectra are used not only for the description of atmospheric turbulence but also in the generation of synthetic wind fields.

Similar to the one-point statistics up to second-order summarized in the turbulence intensity I, the autocorrelation function and the power spectral density are important and widely used statistical quantities. Nevertheless, in the general case higher order two-point statistics are indispensable. In principle we should ask ourselves for higher correlations of the form

$$R_{u'^n u'^m}(\tau) \;=\; \frac{1}{\sigma_{u'}^{n+m}}\left\langle u'(t+\tau)^n\, u'(t)^m\right\rangle. \tag{3.69}$$

However, it is more general and even practical to work with the statistics of wind speed differences. As we will see in the next subsection these are also two-point statistics and their moments contain the arbitrary order two-point correlations defined in eq. (3.69). These will be discussed in the next subsection in terms of wind speed differences.

Higher-order two-point statistics

To investigate more generally two-point statistics and higher order correlations in wind turbulence, let us now consider wind speed differences over a specific time lag τ,

$$u_\tau(t) = u(t+\tau) - u(t) = u'(t+\tau) - u'(t)\,, \tag{3.70}$$

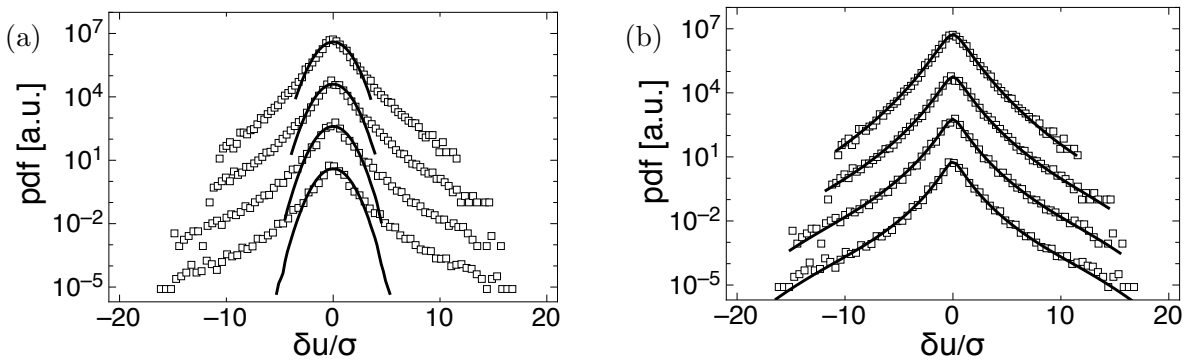

Fig. 3.19 : PDFs of wind speed increments, $u_\tau(t)$, displayed by symbols and shifted vertically. Scales from bottom to top are $\tau = 2$, 4, 10, and 60 s. Additionally, the PDFs are modeled by (a) Gaussian distributions with identical standard deviations, and (b) Castaing's formula (3.72) with (3.73) and (3.74).

which we will refer to as ***wind speed increments*** in the following. Wind speed increments statistics are clearly by definition two-point statistics, and the necessity of selecting a time span for calculating the mean wind speed is avoided. Instead the increments are defined over a scale τ, and the nature of wind speed variations can be studied against the evolution of this scale. The increment's second moment is directly connected to $R_{uu}(\tau)$ by the simple calculation

$$\langle u_\tau(t)^2 \rangle \;=\; 2\langle u(t)^2 \rangle - 2\langle u(t)\, u(t+\tau) \rangle \;=\; 2\langle u(t)^2 \rangle \left(1 - R_{uu}(\tau)\right) , \tag{3.71}$$

where it is assumed that the time series is long enough to ensure $\langle u(t)^2 \rangle = \langle u(t+\tau)^2 \rangle$ within the desired precision. Note that these considerations apply for the wind speeds $u(t)$ as well as for their fluctuations $u'(t)$, at least inside a ten minute interval, see eq. (3.70). Thus, from the power spectral density and autocorrelation function we obtain the variances or the second moment of the wind speed increments as a function of τ. It is straight forward to see that higher moments of wind speed increments, $\langle u_\tau(t)^n \rangle$ with $n > 2$, are related to higher order correlations, compare with eq. (3.69).

In Fig. 3.19a we show PDFs of wind speed increments for different time scales τ, together with Gaussian PDFs which share the same standard deviation. Typically PDFs of atmospheric wind speed increments are non-Gaussian for a wide range of scales and have a special 'heavy-tailed' shape Böttcher *et al.* (2003). As already noted in section 3.6.1, the Gaussian distribution is the only one completely determined by the first two moments. Therefore it becomes clear that for wind speed increments the knowledge of higher-order moments than the second is necessary for a proper characterization of their PDFs. This is a well known and heavily discussed phenomena for turbulence (Frisch 1995) and this is analogous to the case presented in subsection 3.6.1, where we found that higher moments of one-point statistics $\langle u'^n \rangle$ were needed in order to describe the corresponding u' PDFs. AgaThe observed tails in the PDFs imply an increased probability of extreme events, as much as several orders of magnitudes, compared to a Gaussian distribution. Therefore these tails have to be properly reflected in the statistical description.

To this end we follow Böttcher *et al.* (2003) and parameterize the PDFs using Castaing's model Castaing *et al.* (1990), which with some minor modifications is also an explicit formula for eq. (3.65),

$$p(u_\tau) = \frac{1}{2\pi\lambda(\tau)} \int_0^\infty \frac{\mathrm{d}\sigma}{\sigma^2} \exp\left[-\frac{u_\tau^2}{2\sigma^2}\right] \exp\left[-\frac{ln^2(\sigma/\sigma_0)}{2\lambda^2(\tau)}\right] . \tag{3.72}$$

In this equation the PDF is considered as a continuous superposition of Gaussian distributions with different standard deviations, which are weighted by a log-normal distribution function. The shape of the resulting PDF is determined by the two parameters $\lambda^2(\tau)$ and σ_0. Here, σ_0 fixes the median of the lognormal function, while $\lambda^2(\tau)$ mainly dictates the shape of the distribution and is accordingly called the shape parameter. $\lambda^2(\tau)$ is zero for Gaussian distributions and for positive values intermittent distributions are achieved. In general for an emprically given PDF, both parameters can be estimated straightforwardly by an optimization procedure based on equation (3.72). Chilla *et al.* (1996) and Beck Beck (2004) showed that for the case when log-normal superstatistics is the right model, then $\lambda^2(\tau)$ can be directly estimated from the flatness. Following such procedure for Eq. (3.72) we obtain

$$\lambda^2(\tau) \;=\; \frac{\ln\left(F_{u_\tau}/3\right)}{4} \tag{3.73}$$

where F_{u_τ} is the flatness of the increment PDF at a given scale τ, cf. equation (3.64). Considering the moments of Gaussian and log-normal distributions we obtain for σ_0, also from Beck (2004),

$$\sigma_0^2 \;=\; \langle u_\tau^2 \rangle \exp\left[-2\lambda^2(\tau)\right]. \tag{3.74}$$

In Fig. 3.19b we model the PDFs by Castaing's formula (3.72), using (3.73) and (3.74) for a simplified estimation of $\lambda^2(\tau)$ and σ_0. It can be seen that the measured increment PDFs are well reproduced for all scales τ.

Now, in Fig. 3.20 we show how the shape parameter behaves against the scale τ for our offshore data. It is important to note the difference between unconditioned and conditioned (by a mean wind speed bin) values of atmospheric data. The behavior of the PDFs or respectively of $\lambda^2(\tau)$ against scale is similar, but the conditioned PDFs show a reduced overall intermittency. The reduction of intermittency for conditioned data sets is due to the fact that part of this intermittency stems from the non-stationarity of the wind.

Regardless of the absolute value of $\lambda(\tau)$ it is important to note that, for both the conditioned and unconditioned sets, there is a clear range of scales τ where $\lambda^2(\tau) \sim \ln\tau$. This logarithmic dependency has a deep meaning in turbulence and is directly related to the intermittency correction of turbulence in the Kolmogorov 1962 theory (Frisch 1995). In particular with

$$\lambda^2(\tau) \approx \lambda_0^2 - \mu \cdot \ln\tau, \tag{3.75}$$

and using eq. (3.72) one gets

$$\langle u_\tau^n \rangle \propto \tau^{\frac{n}{3} - \mu\frac{n(n-3)}{18}}, \tag{3.76}$$

which is the well known multifractal behaviour of turbulence, see the discussion of Kolmogorov 1962 theory at the end of section 3.5.3.

In summary, we have found that higher moments of the increments are neccessary for the proper estimation of the wind speed increments u_τ PDFs, in particular for the correct estimation of extreme events. Fortunately in many cases with $\sigma_{\delta u}(\tau)$ and $F_{\delta u}(\tau)$, we achieve a precise estimation of arbitrary-order two-point statistics of the wind speed. The according wind speed increment PDFs can be modeled following equations (3.72) to (3.74).

3.6.3 Synthetic Time Series vs Atmospheric Turbulence

Previously, we have presented a hierarchical statistical description of atmospheric turbulence. To summarize and contrast this with what is usually standard and used in the wind energy industry,

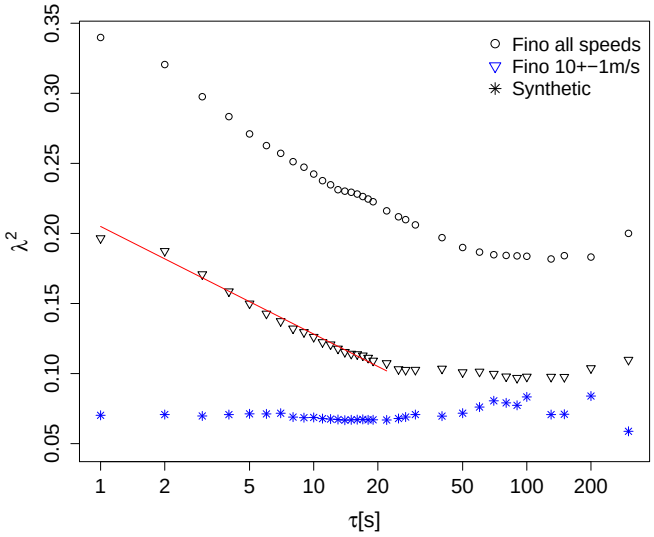

Fig. 3.20 : $\lambda^2(\tau)$ against τ for all wind speeds of the data set ($\circ$), for conditioned wind speeds $(10 \pm 1)\, m/s$ ($\bigtriangledown$), and for a synthetic time series ($*$, see text).

we next apply and compare our statistical scheme to a standard synthetic turbulent wind field and a conditioned FINO data set ($\langle u \rangle_T = 10 \pm 1\, m/s$). We generate with the TurbSim package[23] 10-min. blocks of synthetic time series with Gaussian pdfs $p(u'|\sigma'_T)$. The 10-minutes blocks are summed up following the distribution $p(\sigma'_T)$ of the conditioned FINO data set (compare with subsection 3.6.1). The resultant synthetic time series reproduce closely $p(u')$ (complete one-point statistics) of the conditioned data as seen in Fig. 3.21a. We have used TurbSim with the option of a Kaimal power spectrum, therefore the synthetic time series power spectrum follows nicely the law $S(f) \propto f^{-5/3}$, the conditioned atmospheric data follows a similar scaling as seen in Fig. 3.21b.

On the other hand, when we analyse higher-order two-point statistics, summarized in the behavior of λ^2 against scale τ, we find that the synthetic time series do not at all reproduce the wind PDFs (see Fig. 3.20). For the synthetic time series the characteristic values of λ^2 remain nearly constant at some low values, i.e. the corresponding PDFs are more Gaussian like.

As discussed in the previous section, the ln dependency of λ^2 against τ, expressed in Eq. (3.75), has an important meaning in terms of the turbulent energy cascade. The failure in reproducing such behaviour by the synthetic time series can not be ignored and represents and important weakness of the models used for the synthetic generation. Moreover, as the response time of different control aspects of a Wind Turbine are well within time scales $\tau < 20s$ this part of the scaling plays an important role for the Wind Turbine dynamics.

3.6.4 Outlook: n-point statistics

Previously we proposed a comprehensive characterization of increments PDFs by the shape parameter $\lambda(\tau)^2$. These increment PDFs provide information on arbitrary-order two-point correlations. The natural next step in our hierarchical description would be the study of n-scale statistics. The complete stochastic information is contained in the general n-scale joint PDF,

$$p(u_{\tau_1}, u_{\tau_2}, ..., u_{\tau_n}). \tag{3.77}$$

[23] https://nwtc.nrel.gov/TurbSim .

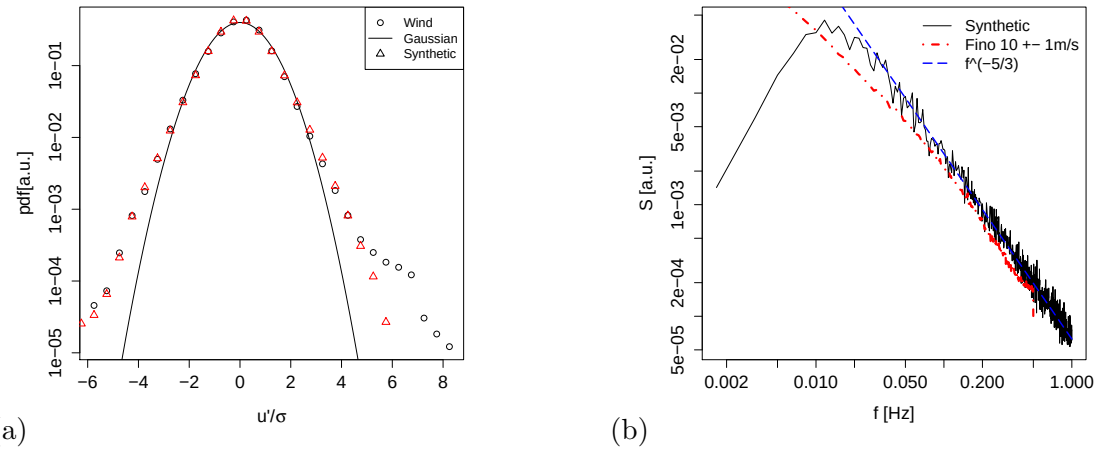

Fig. 3.21 : Basic (a) PDF of $u'(t)$. (b) Normalized FINO and Synthetic spectral densities. A curve following $S \propto f^{-5/3}$ has been added for comparison.

This PDF quantifies the probability that at the same time the wind speed increments $u_{\tau_1}, u_{\tau_2}, ..., u_{\tau_n}$ are observed on the scales τ_1,.....,τ_n. Note that by the definition of eq. (3.71) and that all increments $u(t,\tau) = u(t+\tau) - u(t)$ share the common point $u(t)$ the n-scale probability (3.77) corresponds to an n-point statistics and would capture the arbitrary n-point correlation.

3.6.5 Conclusions

A statistical characterization of wind turbulence has been presented in a hierarchical and mathematically consistent way. In doing so, we have reviewed the well known one-point statistics up to second order summarized in the turbulence intensity as well as the two-point statistics up to second order reflected in the spectral density. We have shown that in general, in the case of wind speed time series, higher order moments contain relevant statistical information in both one and two-point statistics and can not be ignored. Therefore we propose to use the probability density functions of wind speed fluctuations u' and wind speed increments $u_\tau(t)$ in order to grasp the statistical information of higher moments. In the case of the fluctuations u' we have presented a superposition model which describes the measured PDFs very well. A similar approach is used for the increments statistics. Historically this approach has been already applied in laboratory turbulence by Castaing *et al.* (1990), and for atmospheric turbulence by Böttcher *et al.* (2007). For the characterization of wind speed increments $u_\tau(t)$ it is in many cases possible to characterize these increment PDFs just by the shape parameter $\lambda(\tau)^2$. This parameter can be estimated by the second and fourth moment as shown in eq. (3.73) (this has to be done in a careful way by checking the quality of this approach like in Fig. 3.19). Moreover, after conditioning on certain mean wind speeds, a logarithmic decay of $\lambda(\tau)^2$ has been shown (see Fig. 3.20) and its meaning on the turbulent cascade has been pointed out. We would like to note that the current practice in wind energy assessment and according regulations (IEC 2005) do not include the characterization of higher-order two point statistics. An easy improvement in the assessment of turbulent conditions would be the systematic estimation of the shape parameter as a function of τ. Of course a question of special practical importance is which scales τ are relevant for WECs. It seems reasonable to expect that these critical scales will depend on every type of machine, however reaction times on the order of seconds can be expected. Thus the scaling behavior of $\lambda(\tau)^2$ presented in

Type of Statistics	Order	Feature	Random Data	Spectral Models	Wind Turbulence	Characterization
1-point	1	Mean speed	•	•	•	$\bar{u} = \langle u(t) \rangle_T$
	2	Turbulence Intensity	•	•	•	$I = \sigma_{u'}/\bar{u}$
	n	Extreme Fluctuations	-	$*$	•	$p(u')$
2-point	2	Distribution of σ_u over f	-	•	•	$S(f) = \mathcal{F}\{R_{uu}(\tau)\}$
	n	Intermittency of $p(\delta u(\tau))$	-	-	•	$\lambda(\tau)$
n-point	n	Arbitrary-order n-point correlations	-	-	•	To be investigated

Tab. 3.1 : Turbulence Characterization Scheme.

Fig. 3.20 results probably relevant for many machines. As shown here and in Mücke *et al.* (2009), common models and simulation packages for generating synthetic wind fields do not reproduce these two-point statistics. As a consequence, quantitative evaluations of possible effects on WECs due to the non-Gaussian behavior of wind speed increments have not been carried out until very recently Mücke *et al.* (2009). An outlook was given on n-point statistics for the characterization of, e.g., gust clustering and the identification of critical wind gusts shapes. Here we have presented an example on the verification of Markov properties of wind speed increment time series. We pointed out how these Markov properties could ease the description of n-point statistics.

Table 3.1 presents a summary of the observed statistical features in wind time series, as well as the statistical parameters we propose to characterize them. Additionally, columns for synthetic time series generated by spectral models and a random time series (see Fig. 3.18) are presented for comparison purposes.

3.7 Exercises

Exercise 3.1 ***Study of time series of Wind Speed and Wind Turbine Power***

On the ARCHE page of the module, there are two synchronous time series `wind.dat` and `power.dat`, which contain (normalized) measurements of wind speed u in front of a turbine, and the corresponding (normalized) wind turbine power P at the same time values. The sampling frequency is 1 Hz. The velocity is normalized to its maximum value maxu = 24.35 m/s. The power is normalized to its maximum value of the order of a few MW.

1 Import these files to construct two lists `lu` and `lp` with the time series of the real wind speed u in m/s and of the normalized power P. Construct then a list `lup` of (u,P) couples using a subset of like 100 - 1000 data points, to see the time evolution. Plot those in the plane (u,P) and comment.

Indications:

The commands `Directory`, `SetDirectory` and `FileNames` will be useful to be sure that Mathematica will read the right file at the right place. The command `Flatten` will help to get lists of numbers, not lists of lists.

To construct the list `lup`, you may use a program of the form:

```
lup = {};
Do[AppendTo[lup, {lu[[n]], lp[[n]]}], {n, 1, .., 1 }]
```

2 Apply the procedure defined by the IEC norm IEC 2005, described in section 3.3, to construct the ***IEC power curve*** for this case. Comment.

Indications:

First, to construct the data averaged over time intervals of 10 minutes, you may use a program of the form:

```
Lu = lu; Lp = lp;
luapa = {};
Do[
    luofinterest = Take[Lu, X]; Lu = Drop[Lu, X];
    lpofinterest = Take[Lp, X]; Lp = Drop[Lp, X];
    AppendTo[luapa, {Mean[luofinterest], Mean[lpofinterest]}]
  , {na, 1, Na, 1}]
```

with `X` the number of data points in a time interval of 10 minutes, `Na` the number of time intervals of 10 minutes in the whole time series `lu` and `lp`.

Second, to construct the IEC power curve, you may use a program of the form:

```
lucpc = {};
Do[
    Print["ucenter= ", ucenter];
    lupofinterest= Select[luapa, ucenter - 0.25 <= #[[1]] < ucenter + 0.25 &];
    Nupofinterest= Length[lupofinterest];
    Print["Number of data sets in the bin = ", Nupofinterest];
    If[Nupofinterest < .. ,
       Print["Problem, less than 30 minutes of data !!"],
       AppendTo[lucpc, Mean[lupofinterest]] ]
  , {ucenter, 0.25, .. - 0.25, .. }]
```

Exercise 3.2 ***Study of time series of Turbulent Flows***

On the web page of the module, there are two time series of Turbulent Flows, either, an air into air round free jet - file `Jet.dat` -, or, a wind Flow - file `Wind.dat` -. In both cases we note T the time step between two measurements; the actual value of T is not the same in the two cases !..

1 Import the file `Jet.dat` or `Wind.dat`, compute the number N_d of data points, and plot the whole time series.

Indication: the command `Flatten` will help to get a list of numbers, not a list of lists.

2 Prepare two lists where you take either the first 5000 or the last 5000 data points. Plot the time series of the first 5000 and the last 5000 data points. Compare and comment.

3 Determine the mean velocity $\langle u(t) \rangle_t$ for the first 5000 and for the last 5000 data points. Compare and comment. Play also with the number of data points chosen.

4.a Construct a list with the histogram of the data $u(t)$, normalized as a Probability Density Function, and plot it. Indicate the mean value and the standard deviation. Comment.

Indications: Your code should have the following structure, to produce a list with u at the first place and $p(u)$ at the second place:

```
h= HistogramList[..., Automatic, "PDF"]
hup= {};
Do[AppendTo[hup,{(h[[1,n+1]]+h[[1,n]])/2,h[[2,n]]}], {n,Length[h[[2]]]}]
ListPlot[hup, ...]
```

4.b Plot the PDF of u but in linear - log scales. Comment on the character, Gaussian or non Gaussian, of $u(t)$.

5.a Construct a list with the velocity increments

$$u_\tau(t_n) \;=\; u(t_n + \tau) - u(t_n) \;,$$

for $\tau = 10T$, i.e.

$$u_\tau(t_n) \;=\; u(t_{n+10}) - u(t_n) \;.$$

Plot this time series, that we denote hereafter $u_{10}(t)$.

5.b Plot the time series of the first 5000 data points $u_{10}(t)$. Compare with the plots of question 2 and comment.

5.c Do what you did for u in questions 4 but for u_{10}: construct a list with the histogram of the data $u_{10}(t)$, normalized as a Probability Density Function, and plot it; comment; plot this PDF of u_{10} but in linear - log scales; comment on the character, Gaussian or non Gaussian, of $u_{10}(t)$. Compare also the results for `Jet` with those for `Wind`.

6 Redo the analysis of question 5 for a much larger value of the time lapse τ, e.g., $\tau = 500T$. Comment.

Exercise 3.3 ***Study of a time series of a Grid Turbulence Flow***

[*Part of the test of February* 2016]

On the ARCHE page of the module, there is a file `grid.dat` which contains velocity measurements in an air-filled Wind Tunnel, behind a grid. The velocity u in the mainstream direction is given in m/s, with a sampling frequency $f_s = 60$ kHz.

0 Give the value of the time step T between two measurements.

1 Import this file to your computer and determine the number of data points N_d.

2 Observe the data by plotting it. Determine its mean value U and its standard deviation $\sigma = \sqrt{\langle u'^2 \rangle_t}$ with $u' = u - \langle u \rangle_t$ the fluctuating velocity.

3 Estimate the ***turbulence intensity*** I and comment.

4 Construct a list with the histogram of the data $u'(t)$, normalized as a Probability Density Function, and plot it in linear - log scales. Comment on the statistical properties of $u'(t)$.

5 Construct a list with the ***velocity increments***

$$u_\tau(t) = u(t+\tau) - u(t) \ ,$$

for $\tau = 2T$. Construct a list with the histogram of the data $u_\tau(t)$, normalized as a Probability Density Function, and plot it in linear - log scales.
Comment on the statistical properties of $u_\tau(t)$, also, as compared with the ones of $u'(t)$. We expect 4 short sentences with keywords, the last one making a link with Wind Energy physics.

6 What do we expect, if we redo the same analysis as in question 5, but with increasing values of τ ?

7 We admit that the time lapse τ corresponding to the ***integral length scale*** L is $\tau_0 = 1040T$. Compute τ_0 in physical units and, according to the Taylor hypothesis, the integral length scale L.

8 Estimate the ***Reynolds number*** at scale L, $Re = \sigma L/\nu$.

9 Deduce from this and the theory of Kolmogorov 1941 an estimate of the ***dissipation length scale*** η.

Appendix A

Introduction to stochastic theory

This appendix provides the mathematical background for the Langevin-power curve introduced physically in section 3.4.

Complex system can be regarded as systems composed of many microscopic interactions, which lead to some random-like dynamics of macroscopic estimates or macroscopic variables. Let us consider a one-dimensional[1] dynamical system described by the macroscopic variable $x(t)$. The process $x(t)$ is defined as ***stochastic*** because its time evolution is described in a probabilistic sense[2]. Although the sample path $x(t)$ can be continuous, and should be for a purely Markov process, practical applications mostly involve ***discrete signals***. From the continuous process $x(t)$, only N samples x_1, x_2, ..., x_N are known at discrete times $t_1 < t_2 < ... < t_N$. $x(t_i) = x_i$ and $x(t_{i+1}) = x_{i+1}$ are known, yet $x(t)$ for $t_i < t < t_{i+1}$ is unknown. The dynamical system is then described by the discrete samples x_i, so that a complete (statistical) description is given through the joint probability distribution

$$f(x_N,t_N;\ x_{N-1},t_{N-1};\ ...;\ x_1,t_1)\,, \tag{A.1}$$

where $f(A;B;C)$ is the probability of A and B and C happening. The value of sample x_i at time t_i is stochastic, but its probability to have a given value is fixed. Similarly, one can define the conditional probability p following

$$f(x_N,t_N;\ x_{N-1},t_{N-1};\ ...;\ x_1,t_1) \ = \ p(x_N,t_N|x_{N-1},t_{N-1};...;x_1,t_1)\ f(x_{N-1},t_{N-1};\ ...;\ x_1,t_1)\,, \tag{A.2}$$

where $p(A|B;C)$ is the probability of A happening conditioned on (given) B and C happen.

The simplest stochastic process that can be thought of is a purely random process with independent samples x_i (Risken 1996). Independence implies that $p(x_i,t_i|Y) = f(x_i,t_i)$ for any arbitrary condition Y, that is, no matter what the condition Y is, x_i will not depend on it. As a consequence, the joint probability of an independent process is

$$f(x_N,t_N\ ;x_{N-1},t_{N-1};\ ...;\ x_1,t_1) \ = \ \prod_{i=1}^{N} f(x_i,t_i)\,. \tag{A.3}$$

[1] Only an account of one-dimensional stochastic systems is given here, as it suffices for the problem at hand.

[2] Under some weak conditions (that are not presented here for the sake of brevity), if one would let several realizations $x_a(t)$, $x_b(t)$, ..., $x_z(t)$ of that process x evolve in time, one would see that at a given future time t', the exact values of the process have a random character, i.e., $x_a(t') \neq x_b(t') \neq ... \neq x_z(t')$. Yet the probability to obtain a given value remains fixed, giving for the probability distribution $f(x_a,t') = f(x_b,t') = ... = f(x_z,t')$.

A.1 Markov property

Besides the trivial case of an independent process, the next simplest process is a ***Markov process*** (Risken 1996). For a Markov process, only information about the present state is necessary to describe the next future state, regardless of the past state. This means that the state of system x_i at time t_i depends on x_{i-1} at time t_{i-1}, and the conditional probability can be simplified following

$$p(x_i,t_i|x_{i-1},t_{i-1};\ ...;\ x_1,t_1) \ = \ p(x_i,t_i|x_{i-1},t_{i-1})\,. \tag{A.4}$$

Equation (A.2) can be rewritten for a Markov process as

$$f(x_N,t_N;\ x_{N-1},t_{N-1};\ ...;\ x_1,t_1) \ = \ f(x_1,t_1)\prod_{i=2}^{N} p(x_i,t_i|x_{i-1},t_{i-1})\,. \tag{A.5}$$

The Markov property is often described as ***memoryless***. One should note that a (one-dimensional) Markov process $x(t)$ cannot describe n-order differential systems with $n > 1$[3]. In some cases, the Markov property can emerge by introducing new variables (which remain to be found) to a non-Markov dynamical system, i.e., by making it higher-dimensional.

The total probability theorem gives (Papoulis & Pillai 2002)

$$f(x_i,t_i) = \int dx_{i-1}\, f(x_i,t_i;x_{i-1},t_{i-1})\,. \tag{A.6}$$

Similarly for the conditional probability

$$\begin{aligned} p(x_i,t_i|x_{i-2},t_{i-2}) &= \int dx_{i-1}\, p(x_i,t_i;x_{i-1},t_{i-1}|x_{i-2},t_{i-2}) \\ &= \int dx_{i-1}\, p(x_i,t_i|x_{i-1},t_{i-1};x_{i-2},t_{i-2})\ p(x_{i-1},t_{i-1}|x_{i-2},t_{i-2})\,. \end{aligned} \tag{A.7}$$

Using the Markov assumption in equation (A.4), equation (A.7) becomes the Chapman-Kolmogorov equation

$$p(x_i,t_i|x_{i-2},t_{i-2}) = \int dx_{i-1}\, p(x_i,t_i|x_{i-1},t_{i-1})\ p(x_{i-1},t_{i-1}|x_{i-2},t_{i-2})\,. \tag{A.8}$$

For non-Markov processes, the future state does not depend only on the present state, but also on a number of past states, see also Risken (1996); Fox (1977); Farias *et al.* (2009). One can define the Einstein-Markov length τ_{mar} (further referred to as Markov length) as the length of the memory kernel, that is the number of past states that influence the present state. Einstein (1905) presents this coarse-graining as a necessary time interval such that the stochastic forces become independent events . This implies the relation

$$p(x_i,t_i|x_{i-1},t_{i-1};\ ...;\ x_1,t_1) \ = \ p(x_i,t_i|x_{i-1},t_{i-1};\ ...;\ x_j,t_j) \tag{A.9}$$

with $t_j = t_i - \tau_{mar}$. Experimental signals usually exhibit a non-vanishing, yet finite Markov length, see e.g. Lück *et al.* (2006); Stresing *et al.* (2011) for turbulence. Various Markov tests exist to search for a Markov length in data sets.

[3] Let us consider the example of a deterministic (a special case of stochastic) process $x(t)$ governed by an arbitrary second-order differential equation $\ddot{x} = F(x,\dot{x})$. $x(t)$ is not a Markov process because the future state $x(t+dt)$ does not depend only on the present state $x(t)$, but also on $\dot{x}(t)$. Knowing $x(t)$ does not suffice to know $x(t+dt)$. However, the two-dimensional process $\{x(t),\dot{x}(t)\}$ is a (two-dimensional) Markov process, so that knowing $\{x(t),\dot{x}(t)\}$ suffices to know $\{x(t+dt),\dot{x}(t+dt)\}$.

A.2 Kramers-Moyal expansion

The stochastic process $x(t)$ evolves probabilistically in time. Because of its partly random nature, it is inappropriate to describe its exact time evolution, which is not reproducible. Instead, a description of the probability $f(x,t)$ to find a value x at time t is relevant. For a Markov process, $f(x,t)$ follows a ***master equation***

$$\frac{\partial f(x,t)}{\partial t} = \int dx' \left[w(x' \to x) f(x',t) - w(x \to x') f(x,t) \right], \tag{A.10}$$

where $w(a \to b)$ is the transition rate from state a to state b. More concretely, the law of total probability implies

$$f(x,t+\tau) = \int dx'\, f(x,t+\tau;x',t) = \int dx'\, p(x,t+\tau|x',t) f(x',t) \tag{A.11}$$

with $\tau \geq 0$.

Conditional moments are defined following Risken (1996),

$$M^{(n)}(x',t,\tau) = \int dx\ (x-x')^n\, p(x,t+\tau|x',t) = \left\langle \left[x(t+\tau)-x(t)\right]^n \middle| x(t)=x' \right\rangle \tag{A.12}$$

where $\langle A|B\rangle$ is defined as the mean value of A given that condition B is fulfilled. One can derive the Kramers-Moyal expansion (see complete derivation in Risken 1996)

$$\frac{\partial f(x,t)}{\partial t} = \sum_{n=1}^{\infty} \left(-\frac{\partial}{\partial x} \right)^n D^{(n)}(x,t) f(x,t) \tag{A.13}$$

with the Kramers-Moyal coefficients defined as

$$\begin{aligned} D^{(n)}(x,t) &= \frac{1}{n!} \lim_{\tau \to 0} \frac{1}{\tau} M^{(n)}(x,t,\tau) \\ &= \frac{1}{n!} \lim_{\tau \to 0} \frac{1}{\tau} \left\langle \left[x(t+\tau)-x(t)\right]^n \middle| x(t)=x \right\rangle \\ D^{(n)}(x,t) &= \frac{1}{n!} \left. \frac{\partial M^{(n)}(x,t,\tau)}{\partial \tau} \right|_{\tau=0}, \end{aligned} \tag{A.14}$$

where the third relation owes to $M^{(n)}(x,t,\tau=0)=0$.

The ***Kramers-Moyal expansion*** can be formally written

$$\frac{\partial f(x,t)}{\partial t} = L_{KM}(x,t)\ f(x,t) \tag{A.15}$$

with the ***Kramers-Moyal operator*** defined as

$$L_{KM}(x,t) = \sum_{n=1}^{\infty} \left(-\frac{\partial}{\partial x} \right)^n D^{(n)}(x,t)\,. \tag{A.16}$$

Risken (1996) *assumes*[4] that the Kramers-Moyal expansion describes a Markov process, as the evolution $\partial f(x,t)/\partial t$ of the process at time t depends only on its present state $f(x,t)$, and not on some past states $f(x,t')$ for $t' < t$.

[4] Some criticism of the Kramers-Moyal expansion is formulated in Gardiner (1985), where it is argued that the Kramers-Moyal expansion cannot describe the evolution of some Markov jump processes, but only approximate it.

A.3 Fokker-Planck equation

The Fokker-Planck equation is a special case of the Kramers-Moyal expansion for which $D^{(n)}(x) = 0$ for $n \geq 3$. This relates to the Pawula theorem, which states[5] that the Kramers-Moyal expansion (A.13) either stops after $n = 1$, after $n = 2$, or require an infinity of terms, see Risken (1996). This theorem shows from the generalized Schwartz inequality that $[M^{(2n+m)}]^2 \leq M^{(2n)} M^{(2n+2m)}$ for any set of integers $(n,m \geq 0)$. This implies that $D^{(n>2)} = 0$ if there exists one integer $r > 0$ such that $D^{(2r)} = 0$.

If a Markov process $x(t)$ satisfies the Pawula theorem, the Kramers-Moyal expansion stops after the second term and the probability distribution $f(x,t)$ is described by the ***Fokker-Planck equation***

$$\boxed{\frac{\partial f(x,t)}{\partial t} = \left[-\frac{\partial}{\partial x} D^{(1)}(x,t) + \frac{\partial^2}{\partial x^2} D^{(2)}(x,t) \right] f(x,t) = L_{FP}(x,t)\ f(x,t)} \,. \tag{A.17}$$

The ***Fokker-Planck operator*** reads

$$L_{FP}(x,t) = -\frac{\partial}{\partial x} D^{(1)}(x,t) + \frac{\partial^2}{\partial x^2} D^{(2)}(x,t). \tag{A.18}$$

The stationary solution $f_{st}(x)$ of the Fokker-Planck equation, for time-independent coefficients $D^{(1,2)}(x)$, can be derived from

$$\frac{\partial f_{st}(x)}{\partial t} = \left[-\frac{\partial}{\partial x} D^{(1)}(x) + \frac{\partial^2}{\partial x^2} D^{(2)}(x) \right] f_{st}(x) = 0 \,. \tag{A.19}$$

The solution reads

$$f_{st}(x) = \frac{N}{D^{(2)}(x)} \exp\left(\int^x \frac{D^{(1)}(x')}{D^{(2)}(x')} dx' \right) \tag{A.20}$$

with N a normalization constant such that $\int_{-\infty}^{\infty} f_{st}(x)dx = 1$.

Similarly, the Fokker-Planck equation exists for a conditional probability $p(x,t|x',t')$ (that is the distribution $f(x,t)$ for the initial condition $f(x,t') = \delta(x - x')$) and gives

$$\frac{\partial}{\partial t} p(x,t|x',t') = L_{FP}(x,t)\ p(x,t|x',t') \,, \tag{A.21}$$

which has a unique initial condition $p(x,t|x',t) = \delta(x - x')$.

Let us now consider a process that is stationary in time:

$$f(x_N,t_N;...;x_1,t_1) = f(x_N,t_N + \tau;...;x_1,t_1 + \tau)$$

for an arbitrary time shift τ. Then $L_{FP}(x,t) = L_{FP}(x)$ and $D^{(n)}(x,t) = D^{(n)}(x)$, so equation (A.21) has a formal solution

$$p(x,t + \tau|x',t) = e^{\tau\ L_{FP}(x)} \delta(x - x') \tag{A.22}$$

owing to the initial condition $p(x,t|x',t) = \delta(x - x')$.

It is shown in Risken (1996) that equation (A.22) also holds for a time-dependent $L_{FP}(x,t)$ if the time increment τ is sufficiently small so that $D^{(n)}$ can be seen as unchanged coefficients. Based

[5] The Pawula theorem only applies if the conditional probability $p(x,t + \tau|x',t)$ is a non-negative function.

on the definition of the delta function $\delta(x-x')$, equation (A.22) gives the short-time propagator of the Fokker-Planck equation for small τ (for details see Risken 1996):

$$p(x,t+\tau|x',t) = \frac{1}{\sqrt{4\pi\tau D^{(2)}(x',t)}} \exp\left(-\frac{[x-x'-\tau D^{(1)}(x',t)]^2}{4\tau D^{(2)}(x',t)}\right). \tag{A.23}$$

The Fokker-Planck equation (A.17) is a linear partial differential equation that can be solved numerically. Besides the direct method that consists in numerically approximating the differential operators, one can use a path integral method (Risken 1996). Similarly to what is done in quantum mechanics to solve the Schrödinger equation, this method is easy to implement. Given an initial condition $f(x,t_0)$, equation (A.11) gives $f(x,t_0+\tau)$ using $p\big(x,t_0+\tau\big|x,t_0\big)$. This can be iterated $n-$times to calculate $f(x,t_n)$ from $f(x,t_{n-1})$ for time $t_n = t_0+n\tau$. One can formulate this following

$$\begin{aligned} f(x,t_n) = &\int dx_{n-1}\int dx_{n-2}...\int dx_0 \\ &p\big(x,t_n\big|x_{n-1},t_{n-1}\big)p\big(x_{n-1},t_{n-1}\big|x_{n-2},t_{n-2}\big)...p\big(x_1,t_1\big|x_0,t_0\big)f(x_0,t_0)\,. \end{aligned} \tag{A.24}$$

For a small enough time increment τ, the conditional probability is given by equation (A.23). A similar approach can be used for $p(x,t_0+n\tau|x',t_0)$ using the Chapman-Kolmogorov equation (A.8) and the initial condition $p(x,t_0|x',t_0)=\delta(x-x')$.

A.4 Langevin equation

Based on the historical example of Brownian motion, a ***Langevin equation*** for a ***Langevin process*** $x(t)$ reads

$$\boxed{\frac{dx}{dt} = D^{(1)}(x,t) + \sqrt{D^{(2)}(x,t)}\cdot\Gamma(t)}\,. \tag{A.25}$$

The Kramers-Moyal coefficients are the coefficients defined in equation (A.14).

The time evolution of a sample path $x(t)$ is described by the so-called drift coefficient $D^{(1)}(x,t)$ and diffusion coefficient $D^{(2)}(x,t)$. In parallel, the probability $f(x,t)$ is described by the Fokker-Planck equation (A.17). For a given set of drift and diffusion coefficients, the Fokker-Planck equation gives a unique solution $f(x,t)$. On the contrary, the Langevin equation can generate different sample paths $x_i(t)$ that have different values (due to the randomness of the Langevin noise $\Gamma_i(t)$). Yet the probability that $x_i(t_j)=X$ is the unique solution of the Fokker-Planck equation $f(X,t_j)$.

The Langevin equation can be discretized following

$$\begin{aligned} x(t+dt) &= x(t) + \int_t^{t+dt}\frac{dx}{dt}(t')dt' \\ &= x(t) + \int_t^{t+dt} D^{(1)}(x,t')dt' + \int_t^{t+dt}\sqrt{D^{(2)}(x,t')}\Gamma(t')dt'\,. \end{aligned} \tag{A.26}$$

The integration of $\Gamma(t)$ is not defined mathematically, yet a physical interpretation of the stochastic integral is needed. The definition of stochastic integration in the sense of Itô gives[6]

$$\int_t^{t+dt} g(x,t')\Gamma(t')dt' = g(x,t)\int_t^{t+dt}\Gamma(t')dt'\,. \tag{A.27}$$

[6] Another common approach to carry out a stochastic integral is the Stratanovich definition that reads $\int_t^{t+dt} g(x,t')\Gamma(t')dt' = g\Big(\frac{x(t+dt)-x(t)}{2}\,,\ t+dt/2\Big)\int_t^{t+dt}\Gamma(t')dt'$. The Stratanovich approach is more intuitive because it considers the value of the function g at the middle point of the integration range. Only the Itô interpretation is

For $dt \ll 1$, $D^{(n)}$ can be taken as unchanged coefficients and equation (A.26) becomes

$$x(t+dt) = x(t) + D^{(1)}(x,t)dt + \sqrt{D^{(2)}(x,t)} \int_t^{t+dt} \Gamma(t')dt' \,. \tag{A.28}$$

The Langevin noise $\Gamma(t)$ fluctuates much faster than the stochastic process $x(t)$ and has a correlation length much shorter than dt (its theoretical correlation length is zero). The Langevin noise is related to a Wiener process $W(t)$ in that $\dot{W} = \Gamma(t)$, bringing the Stieltjes integral

$$\int_t^{t+dt} \Gamma(t')dt' = \int_t^{t+dt} dW(t') = \sqrt{dt} \cdot \eta(t) \tag{A.29}$$

with $\eta(t)$ a set of independent, Gaussian-distributed samples following $\langle \eta(t) \rangle = 0$ and $\langle \eta(t)^2 \rangle = 2$. The discrete form of the Langevin equation for a small time increment dt becomes

$$x(t+dt) = x(t) + D^{(1)}(x,t)dt + \sqrt{D^{(2)}(x,t)dt} \cdot \eta(t) \,. \tag{A.30}$$

A sample path $x(t_0 + n\ dt)$ can be generated by iterating $n-$times the integration from an initial condition $x(t_0)$.

used here, as it is easier to implement numerically. Also, the definition of the Kramers-Moyal coefficients is different in the Stratanovich interpretation. Both interpretations are equivalent, as they yield identical probability distributions (Friedrich *et al.* 2011). Sokolov (2010) summarizes various interpretations of the Langevin equation in the presence of non-constant $D^{(2)}$.

Appendix B

Elements of solution of the problems

Problem 1.1 ***Lorenz model of slip Rayleigh-Bénard Thermoconvection***

2 With $D_1 = k^2 + \pi^2$,

$$[D \cdot \partial_t V]_1 \;=\; P^{-1}\; \dot{A}\; D_1\;\; \sin(kx)\cos(\pi z)\;,$$

$$[L_R \cdot V]_1 \;=\; -\,A\; D_1^2\;\; \sin(kx)\cos(\pi z) \;+\; kRB\;\; \sin(kx)\cos(\pi z)\;,$$

$$[N_2(V,V)]_1 \;=\; 0\;,$$

$$[D \cdot \partial_t V]_2 \;=\; \dot{B}\;\; \cos(kx)\cos(\pi z) \;+\; \dot{C}\;\; \sin(2\pi z)\;,$$

$$[L_R \cdot V]_2 \;=\; -\,B\; D_1\;\; \cos(kx)\cos(\pi z) \;-\; 4\pi^2\; C\;\; \sin(2\pi z) \;+\; k\; A\;\; \cos(kx)\cos(\pi z)\;,$$

$$[N_2(V,V)]_2 \;=\; \frac{k\pi}{2}\; A\; B\;\; \sin(2\pi z) \;-\; k\pi\; A\; C\;\; \cos(kx)\;[\cos(\pi z) + \cos(3\pi z)]\;.$$

3.a

$$P^{-1}\; \dot{A}\; D_1 \;=\; -\,A\; D_1^2 \;+\; kR\; B\;. \tag{B.1}$$

3.b

$$\dot{B} \;=\; -\,B\; D_1 \;+\; k\; A \;-\; k\pi\; A\; C\;, \tag{B.2}$$

$$\dot{C} \;=\; -\;4\pi^2\; C \;+\; \frac{k\pi}{2}\; A\; B\;, \tag{B.3}$$

3.c Except very special cases, the heat equation is not fulfilled: the Lorenz model is an ***approximate model***.

4

$$r \;=\; k^2 R / D_1^3 \tag{B.4}$$

is the ***main control parameter*** of the system, since it can be changed easily by changing δT hence R; it must be viewed as a ***'reduced Rayleigh number'***.

$$b \;=\; 4\pi^2 / D_1\;. \tag{B.5}$$

6 Two new fixed points

$$X \;=\; Y \;=\; \pm\sqrt{b(r-1)}\;, \quad Z \;=\; r-1 \quad \text{appear if } r \;>\; 1\;. \tag{B.6}$$

This corresponds to a ***supercritical pitchfork bifurcation*** that leads from the static conduction configuration to ***thermoconvection rolls*** of finite amplitude.

7 One recovers the 'optimal' or 'critical' values

$$K_c \;=\; \pi^2/2\;,\quad k_c \;=\; \pi/\sqrt{2}\;,\quad R_c \;=\; 27\pi^4/4 \tag{B.7}$$

already found in Ex. 1.0.

8 $r \;=\; 1+\epsilon \quad$ and $\quad b \;=\; 8/3\;.$

9 $X_0 \;=\; Y_0 \;=\; \sqrt{b\epsilon}\;,\quad Z_0 \;=\; \epsilon\;.$

10.a

$$[M] \;=\; \begin{bmatrix} -P & P & 0 \\ 1 & -1 & -\sqrt{b\epsilon} \\ \sqrt{b\epsilon} & \sqrt{b\epsilon} & -b \end{bmatrix}\;. \tag{B.8}$$

10.b $\chi(\sigma) \;=\; \sigma^3 + (P+1+b)\sigma^2 + b(1+\epsilon+P)\sigma + 2Pb\epsilon\;.$

10.c A change of sign of q, from $q<0$ for small $\epsilon>0$, to $q>0$ for $\epsilon>\epsilon_1$, would signal a ***secondary oscillating instability***.
Right at the point where this change of sign would occur, the spectrum of $[M]$ would assume the form

$$\{\sigma_1,\,\sigma_2,\,\sigma_3\} \;=\; \{i\omega,\;-i\omega,\;-s\} \quad \text{with} \quad \omega\in\mathbb{R}^{+*},\, s\in\mathbb{R}^{+*}\;.$$

Hence the characteristic polynomial

$$\chi(\sigma) \;=\; (\sigma-i\omega)(\sigma+i\omega)(\sigma+s) \;=\; \sigma^3 + s\sigma^2 + \omega^2\sigma + s\omega^2\;.$$

By identification we get

$$s = P+1+b\;,\quad \omega^2 = b(1+\epsilon+P) \quad \text{and} \quad s\omega^2 = 2Pb\epsilon\;.$$

This gives the relation

$$(P+1+b)b(1+\epsilon+P) \;=\; 2Pb\epsilon \quad\Longleftrightarrow\quad \epsilon \;=\; \epsilon_1 \;=\; (1+P)(1+b+P)/(P-b-1)\;, \tag{B.9}$$

that is, for $b=8/3$,

$$\epsilon_1 \;=\; (1+P)(P+11/3)/(P-11/3)\;. \tag{B.10}$$

We recover the criterion given in the Lecture Notes, $P>11/3$, for secondary instabilities of the thermoconvection rolls.

10.d For $P=11$, we obtain a lower bound for the ***onset of chaos***

$$\epsilon_1 = 24 \quad\Longleftrightarrow\quad r = 25 \quad\Longleftrightarrow\quad R \;=\; 675\pi^4/4 \;\simeq\; 16440\;.$$

Problem 2.1 ***Spatial linear stability analysis - The case of Plane Poiseuille Flow***

1

$$-r(D^2-k^2)^2\Psi \;+\; i(kU-\omega)(D^2-k^2)\Psi - ikU''\Psi \;=\; 0\;. \tag{B.11}$$

A difficulty is that k appears up to the fourth power.

2 $D\Psi(z) \;=\; [(D-k)\Phi(z)]\;e^{-kz}\;,\quad D^2\Psi(z) \;=\; [(D^2-2kD+k^2)\Phi(z)]\;e^{-kz}\;,$
$(D^2-k^2)\Psi(z) \;=\; [(D^2-2kD)\Phi(z)]\;e^{-kz}\;,\quad (D^2-k^2)^2\Psi(z) \;=\; [(D^2-2kD)^2\Phi(z)]\;e^{-kz}\;,$

$$-r(D^2-2kD)^2\Phi \;+\; i(kU-\omega)(D^2-2kD)\Phi - ikU''\Phi \;=\; 0\;. \tag{B.12}$$

3 $L_1 \;=\; 4rD^3+i(UD^2+2\omega D)-iU''\;,\quad L_2 \;=\; -rD^4-i\omega D^2\;,\quad D_1 \;=\; 4rD^2+2iUD\;.$

5 Ψ and Φ satisfy the same boundary conditions.

6 The spectral expansion (2.83) corresponds to a polynomial expansion of $\Phi(z)$ onto a basis of functions that satisfy the boundary conditions. Contrarily to what has been done in the temporal analysis, where only Chebyshev polynomials even under $z\mapsto -z$ have been used, here, even if Ψ is even under $z\mapsto -z$, because of the factor e^{kz} between Φ and Ψ, the corresponding function Φ has no symmetry property under $z\mapsto -z$. This explains why in the expansion (2.83) all Chebyshev polynomials are used, not only the ones with an even index.

7.1 For $N_z=9$, the collocation points

$$z_m \;=\; \cos(m\pi/10) \quad \text{for} \quad m\in\;\{1,2,\cdots,9\}$$

can be constructed by dividing the upper part of the unit circle in 10 equal angles, and projecting the corresponding points onto the horizontal axis, which plays here the role of the z-axis. This gives the blue points below, which scan the whole interval $z\in[-1,1]$, and will gather close to the walls $z=\pm 1$ as N_z increases:

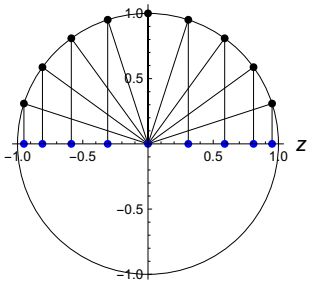

This seems a good choice to discretize an ODE in the interval $z\in[-1,1]$, with terms that have no symmetry properties under $z\mapsto -z$, and large gradients near the walls.

7.2

$$ML1_{mn} \;=\; L_1\cdot F_n(z_m)\;,\quad ML2_{mn} \;=\; L_2\cdot F_n(z_m)\;,\quad MD1_{mn} \;=\; D_1\cdot F_n(z_m)\;. \tag{B.13}$$

9 $\exp(ikx) \;=\; \exp(ik_rx-k_ix) \quad\Longrightarrow\quad sr \;=\; -k_i$; see the Fig. 2.8a.

10 - 11 See the Fig. 2.8b. We recover the same critical parameters as with the temporal stability analysis. At this stage the spatial stability analysis does not bring new information.

12 $\ell_0 = 39.4 \quad \Longrightarrow \quad$ for $\epsilon = 0.1$ we get

$$s_r \;=\; 0.0025 \quad \Longleftrightarrow \quad s_r\lambda_c \;=\; 0.0156 \quad \Longleftrightarrow \quad \exp(s_r\lambda_c) \;=\; 1.016\ ,$$

we find a spatially amplified mode with a small amplification rate (Fig. 2.8a). This viscous instability is somehow, at the linear stage, 'moderate'.

Bibliography

Ahlers, G., Grossmann, S. & Lohse, D. 2009 Heat transfer and large scale dynamics in turbulent Rayleigh-Bénard convection. *Rev. Mod. Phys.* **81**, 503–537, DOI: 10.1103/RevModPhys.81.503 - UL link.

Anahua, E., Barth, S. & Peinke, J. 2008 Markovian power curves for wind turbines. *Wind Energy* **11**, 219–232.

Beck, C. 2004 Superstatistics in hydrodynamic turbulence. *Physica D* **193**, 195–207.

Bergé, P., Pomeau, Y. & Vidal, C. 1984 *Order within Chaos: Towards a Deterministic Approach to Turbulence*. John Wiley & Sons.

Betz, A. 1927 Die Windmühlen im Lichte neuerer Forschung. *Die Naturwissenschaften* **15**, 46.

Bianchi, F., De Battista, H. & Mantz, R. 2006 *Wind Turbine Control Systems*, 2nd edn. Berlin: Springer.

Bierbooms, W. 2009 Constrained Stochastic Simulation of Wind Gusts for Wind Turbine Design. PhD thesis, Delft University Wind Energy Research Institute.

Bodenschatz, E., Pesch, W. & Ahlers, G. 2000 Recent developments in Rayleigh-Bénard Convection. *Annu. Rev. Fluid Mech.* **32**, 709–778.

Böttcher, F., Peinke, J., Kleinhans, D. & Friedrich, R. 2007 Handling systems driven by different noise sources – Implications for power estimations. *Wind Energy*, pp. 179–182. Berlin: Springer.

Böttcher, F., Renner, C., Waldl, H.-P. & Peinke, J. 2003 On the statistics of wind gusts. *Boundary-Layer Meteorology* **108**, 163–173.

Burton, T., Sharpe, D., Jenkins, N. & Bossanyi, E. 2001 *Wind Energy Handbook*. New York: Wiley.

Busse, F. H. 2003 The sequence-of-bifurcations approach towards understanding turbulent fluid flow. *Surveys in Geophys.* **24**, 269–288.

Castaing, B., Gagne, Y. & Hopfinger, E. 1990 Velocity probability density functions of high Reynolds number turbulence. *Physica D* **46**, 177–200.

Chilla, F., Peinke, J. & Castaing, B. 1996 Multiplicative Process in Turbulent Velocity Statistics: A Simplified Analysis. *J. Phys. II France* **6**, 455–460.

Davis, G. D. V. 1983 Natural convection of air in a square cavity: a benchmark numerical solution. *Int. J. Numer. Methods Fluids* **3**, 249.

Drazin, P. D. 2002 *Introduction to hydrodynamic stability*. Cambridge University Press.

Einstein, A. 1905 Über die von der molekularkinetischen der Wärme geforderte Bewegung von in ruhenden Flüssigkeiten suspendierten Teilchen. *Ann. Phys.* pp. 549–560.

Farias, R. L. S., Ramos, R. O. & da Silva, L. A. 2009 Stochastic Langevin equations: Markovian and non-Markovian dynamics. *Phys. Rev. E* **80**, 031143 (14p).

Fox, R. F. 1977 Analysis of nonstationary, Gaussian and non-Gaussian, generalized Langevin equations using methods of multiplicative stochastic processes. *J. Stat. Phys.* pp. 259–279.

Friedrich, R. & Peinke, J. 2009 Fluid Dynamics, Turbulence. *Encyclopedia of Complexity and Systems Science* (ed. R. A. Meyers), pp. 3641–3661. Springer New York, DOI: 10.1007/978-0-387-30440-3_215.

Friedrich, R., Peinke, J., Sahimi, M. & Tabar, M. R. R. 2011 Approaching complexity by stochastic methods: From biological systems to turbulence. *Phys. Rep.* **506**, 87 – 162.

Frisch, U. 1995 *Turbulence. The legacy of Kolmogorov*. Cambridge University Press.

Gardiner, C. W. 1985 *Handbook of Stochastic Methods*. Springer Verlag.

Gottschall, J. 2009 Modelling the variability of complex systms by means of Langevin processes. PhD thesis, Carl von Ossietzky Universität Oldenburg, Germany.

Gottschall, J. & Peinke, J. 2008 How to improve the estimation of power curves for wind turbines. *Environmental Res. Lett.* **3**, 015005 (7p).

Haken, H. 1983 *Synergetics - An introduction*. Springer-Verlag.

Hansen, K. S. & Larsen, G. C. 2005 Characterising Turbulence Intensity for Fatigue Load Analysis of Wind Turbines. *Wind Engineering* **29**, 319–329.

Hu, Y., Ecke, R. & Ahlers, G. 1993 Convection near threshold for Prandtl numbers near 1. *Phys. Rev. E* **48**, 4399–4413, DOI: 10.1103/PhysRevE.48.4399 - UL link.

Huerre, P. & Rossi, M. 1998 Hydrodynamic instabilities in open flows. *Hydrodynamics and Nonlinear Instabilities* (ed. C. Godrèche & P. Manneville), pp. 81–294. Cambridge University Press.

IEC 2005 Wind Turbine Generator Systems, Part 12: Wind turbine power performance testing. International Standard 61400-12-1. International Electrotechnical Commission.

Jenny, M. 2016 *Machines à fluides - Turbomachines*. Cours de Mines Nancy (2A), http://energie.mines-nancy.univ-lorraine.fr/2A/turbo2a.pdf.

Larsen, G. & Hansen, K. 2006 The statistical distribution of turbulence driven velocity extremes in the atmospheric boundary layer – Cartwright/Longuet-Higgins revised. *Wind Energy. Proc. Euromech Colloquium 464b, Oldenburg* (ed. J. Peinke, P. Schaumann & S. Barth), pp. 111–114. Springer.

Larsen, G. C. & Hansen, K. S. 2008 Rational Calibration of Four IEC Research 61400-1 Extreme External Conditions. *Wind Energy* **11**, 685–702.

Lorenz, E. 1963 Deterministic Nonperiodic Flow. *J. Atmospheric Sci.* **20**, 130–141, DOI: 10.1175/1520-0469(1963)020<0130:DNF>2.0.CO;2 - Open access.

Lück, S., Renner, C., Peinke, J. & Friedrich, R. 2006 The Markov - Einstein coherence length - a new meaning for the Taylor length in turbulence. *Phys. Lett. A* **359**, 335 – 338.

Milan, P., Mücke, T., Wächter, M. & Peinke, J. 2010 Two numerical modeling approaches for wind energy converters. *Proc. Comput. Wind Eng. 2010* .

Mücke, T., Kleinhans, D. & Peinke, J. 2009 Influence of small scale wind velocity fluctuations on the aerodynamic alternating loads. *Proceedings of EWEC 2009*.

Naert, A., Castaing, B., Chabaud, B., Hebral, B. & Peinke, J. 1998 Conditional statistics of velocity fluctuations in turbulence. *Physica D* **113**, 73–78.

Panofsky, H. & Dutton, J. A. 1984 *Atmospheric Turbulence - Models and Methods for Engineering Applications.*. Wiley, New York.

Papoulis, A. & Pillai, S. U. 2002 *Probability, random variables, and stochastic processes*. Tata McGraw-Hill Education.

Plapp, B. B. 1997 Spiral pattern formation in Rayleigh-Benard convection. PhD thesis, Cornell University.

Plaut, E. 2008 *Modélisation d'instabilités : méthodes non linéaires*. Cours du Master 2 recherche de mécanique-énergétique de Nancy, téléchargeable sur http://emmanuelplaut.perso.univ-lorraine.fr/publisp.

Plaut, E. 2016 *Mécanique des fluides*. Cours de Mines Nancy (2A), http://emmanuelplaut.perso.univ-lorraine.fr/mf/pol.pdf.

Plaut, E., Lebranchu, Y., Simitev, R. & Busse, F. H. 2008 Reynolds stresses and mean fields generated by pure waves: applications to shear flows and convection in a rotating shell. *J. Fluid Mech.* **602**, 303–326.

Press, W. H., Teukolsky, S. A., Vetterling, W. T. & Flannery, B. P. 1996 *Numerical Recipes in C The Art of Scientific Computing*, 2nd edn. Cambridge University Press.

Rankine, W. 1865 On the mechanical principles of the action of propellers. *Transactions of the Institute of Naval Architects* **6**, 13–39.

Rauh, A. 2008 On the Relevance of Basic Hydrodynamics to Wind Energy Technology. *Nonlinear Phenomena in Complex Systems* **11** (2), 158–163.

Rauh, A. & Peinke, J. 2004 A phenomenological model for the dynamic response of wind turbines to turbulent wind. *J. Wind Eng. Ind. Aerodyn.* **92**, 159–183.

Rauh, A. & Seelert, W. 1984 The Betz optimum efficiency for windmills. *Applied Energy* **17**, 15–23.

Renner, C., Peinke, J. & Friedrich, R. 2001 Experimental indications for Markov properties of small-scale turbulence. *J. Fluid Mech.* **433**, 383–409, DOI: 10.1017/S0022112001003597.

Reynolds, O. 1895 On the dynamical theory of incompressible viscous fluids and the determination of the criterion. *Phil. Trans. Roy. Soc. Lond.* **186**, 123–164.

Richardson, L. F. 1922 *Weather prediction by numerical process*. Cambridge University Press.

Risken, H. 1984 *The Fokker-Planck equation*. Berlin: Springer.

Risken, H. 1996 *The Fokker-Planck Equation*. Springer.

Rosen, A. & Sheinman, Y. 1994 The average power output of a wind turbine in turbulent wind. *J. Wind Eng. Ind. Aerodyn.* **51**, 287.

Schlatter, P., Deusebio, E., de Lange, R. & Brandt, L. 2010 Numerical study of the stabilisation of boundary-layer disturbances by finite amplitude streaks. *Int. J. Flow Control* **2**, 259–288, DOI: 10.1260/1756-8250.2.4.259.

Schlüter, A., Lortz, D. & Busse, F. H. 1965 On the stability of steady finite amplitude convection. *J. Fluid Mech.* **23**, 129–144.

Schmid, P. J. & Henningson, D. S. 2001 *Stability and transition in shear flows*. Springer-Verlag.

Sokolov, I. 2010 Ito, Stratonovich, Hänggi and all the rest: The thermodynamics of interpretation. *Chemical Physics* **375**, 359 – 363, stochastic processes in Physics and Chemistry (in honor of Peter Hänggi).

Stasiek, J. 1997 Thermochromic liquid crystals and true colour image processing in heat transfer and fluid-flow research. *Heat and Mass Transfer* **33**, 27–39, DOI: 10.1007/s002310050158 - UL link.

Stresing, R., Kleinhans, D., Friedrich, R. & Peinke, J. 2011 Different methods to estimate the Einstein-Markov coherence length in turbulence. *Phys. Rev. E* **83**, 046319 (9p).

Stull, R. B. 1994 *An Introduction to Boundary Layer Meteorology*. Kluwer Academic Publishers.

Türk, M. & Emeis, S. 2007 The Dependence of Offshore Turbulence Intensity on Wind Speed. *DEWI Magazine* **30**, 10–13.

Twele, J. & Gasch, R. 2005 *Windkraftanlagen*. Teubner B.G. GmbH.